2D NETWORKS BY DEPOSITION OF PD-CYCLOMETALLATES ON AG(110)

Doctoral dissertation of Marija Stojkovska, XXXV cycle

Supervisors: Dr. Letizia Savio (Imem-cnr) &

prof. Gianagelo Bracco (Unige)

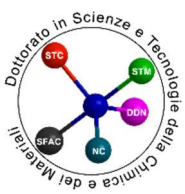

ABSTRACT

Among possible organometallic compounds, complexes of the Group 10 elements are attractive due to their widespread use in numerous applications such as catalytic synthetic processes, biological chemistry, and material science. Many palladium complexes have been extensively studied as catalysts in several cross-coupling reactions and while great advancements have been made on the synthesis of transition metal complexes with specifically designed properties, our understanding about their interactions with metal surfaces is still quite limited. Their coupling to a surface is of interest, since their self-assembly on metal surfaces could lead to a major impact in catalysis and sensoristics.

My Ph.D. thesis enters this field, in the framework of the projects "MC-nano" (by Fondazione Compagnia di San Paolo) and "MADAM - Metal Activated low dimensional carbon-based nanostructures", (PRIN2017, by MUR). I did my research work in the joint IMEM-DIFI laboratory, at the Department of Physics of University of Genoa, under the supervision of prof. G. Bracco and Dr. L. Savio. I worked in collaboration with partners from Università di Milano Bicocca and with the staff of the ALOISA beamline of the ELETTRA Synchrotron Light Source in Trieste since most of the XPS measurements were performed during a beamtime there. I investigated the self-assembly and thermal evolution of two palladium cyclomatellated compounds: $C_{22}H_{14}Br_2Cl_2N_2Pd_2$ (CyPd) and $C_{22}H_{16}Cl_2N_2Pd_2$ (CyPd_2). Such class of molecules were deposited on Ag(110) for the first time. The systems were studied for different coverages and annealing temperatures from RT to 500 °C by low-temperature scanning tunneling microscopy. The results were interpreted in combination with complementary photoemission spectroscopy measurements and theoretical calculations performed by the partner groups. My data reports on the long range and well-ordered self-assemblies formed by Pd cyclomatellated compounds on Ag(110) by STM. It highlights the active role of the substrate which promotes dissociation of the molecules upon adsorption, and the role of molecular geometry on the morphology of the nanostructure. Annealing the CyPd or CyPd_2/ Ag(110) system to 100 °C or above leads to the formation of new structures and surface reconstruction.

CONTENTS

LIST OF ACRONYMS

1D	1-Dimensional
Ag	Silver
BE	Binding Energy
CyPd	Cyclometallated Palladium complex (dibrominated)
CyPd_2	Cyclometallated Palladium complex (non-brominated)
DOD	Dodecanethiol
DOS	Density of states
DFT	Density Functional Theory
LDOS	Local density of states
LHe	Liquid Helium
LN_2	Liquid Nitrogen
LT	Low Temperature
PDT	1,3-pentadithiols
PhDT	Phenyl Dithiol (
STM	Scanning Tunnelling Microscopy
STS	Scanning Tunneling Spectroscopy
ML	Monolayer
NPs	Nano Particles
NEXAFS	Near-Edge X-ray Adsorption Fine Structure Spectroscopy
QDs	Quantum Dots
QMS	Quadrupole Mass Spectrometer
STS	Scanning Tunnelling Spectroscopy
TSP	Titanium Sublimation Pump
UHV	Ultra High Vacuum
XPS	X-ray Photoemission Spectroscopy

1. INTRODUCTION

Among possible organometallic compounds, complexes of the Group 10 elements are attractive due to their widespread use in numerous applications such as catalytic synthetic processes [1]–[3], biological chemistry [4]–[6] and material science [7], [8]. In particular, many palladium complexes have been extensively studied as catalysts in several cross-coupling reactions [9], [10]. In these reactions, two reagents are joint together with the aid of a metal catalyst forming, in the most common case, new C-C bond. They are of strategic importance since they allow to produce complex molecular architectures, possibly doped with heteroatoms, but they are also the most widespread method to synthesize several key precursors for the production of pharmaceuticals and organic compounds, such as arylalkynes and conjugated enzymes. [11]. When they take place on solid surfaces, the coupling can occur between adjacent molecules of the same or of different species [12]–[14]. Due to the confinement in two dimensions (2D), the use of vacuum environment and the absence of solvents, the process can lead to different reaction steps and possibly to different reaction products. This enables the formation of complex building blocks and intermediates.

Recently, great advancements have been made in organic synthesis of transition metal (TM) complexes with specifically designed properties. However, our understanding about their interactions with metal surfaces is still quite limited. Their coupling to a surface is of interest, since their self-assembly on metal surfaces could lead to a major impact in catalysis and sensoristic.

A fundamental requirement for such a strategy is the stability of the selected TM complex in the experimental conditions used for the surface deposition. Among the possible candidates, cyclometallated complexes display sufficiently high stability thanks to the presence of a E-M-C sequence of sigma bonds, where E is usually a group 15 or 16 donor atoms, M is a metallic center and C is a sp^2 or sp^3 carbon atom [15], [16]. Up to now, for such compounds only few studies have been conducted for on-surface modification by using a bottom-up approach. For instance, Wilde et al. [17] successfully deposited Pt(II) cyclometallated on Ag(111) and demonstrated by scanning tunneling microscopy (STM) that the intermolecular interactions upon 2D confinement are mainly driven by the entanglement of aliphatic side chains. Ren et al. [18] investigated the tetradentated Pt(II) complexes on various noble metal (111) surfaces and reported on the surface-mediated scission of the C-N bond in the organometallic compound upon annealing. They found out that the reactivity of the system strongly depends on the geometry of the coordination compounds and on the nature of the substrate. Similarly, dissociation of Ir(III) phosphorescent emitter molecules was observed on Cu(110) [19]. I note that all this work concerns cyclometallated complexes of the third-row transition-metal elements, such as Ir(III) and Pt(II), which are of interest as light emitters. To my knowledge, nothing has ever been reported on Pd cyclometallated complexes at metal surfaces, though these compounds are relevant especially for catalytic applications.

It is well-established that carbon-based nanostructures can be doped with hetero-atoms to tune their electronic and chemical properties [20]. By far, the most studied systems concern doping

with non-metal atoms (e.g., N, P, S, B). On the other hand, TM containing C-networks are predicted to have interesting electronic and catalytic properties and can present a low-cost alternative to the existing catalysts based on precious metals. Among the different ways to grow 1D and 2D molecular architectures [21]–[25], the self-assembly and possible polymerization of properly designed precursors guarantees the best uniformity and degree of order [12], [26]. The properties of the self-assemblies depend on intra- and inter-molecular interactions, choice of sample, temperature, and surface coverage. Accordingly, functionalization of molecular precursors with different types of halogen substituents can be used to steer the on-surface reactions. For instance, the dissociation energy of the halogen atoms from the molecular precursors depends on the type of halogen atom. As the size of halogen atom increases, the C–X bond length increases while the C–X bond strength decreases. Thus, the C-X bond strength is increasing in the order C–F>C–Cl>C–Br>C–I [27]. Consequently, Iodine (I) would require a lower activation temperature compared to bromine (Br) or chlorine (Cl) to be split off from the molecule on the same substrate. The presence of dissociated halogens on the surface can also influence the final adsorption configuration of the molecules. E.g., Dettmann et al. compared the thermal evolution of differently halogenate para-phenylenes and demonstrated that the halogen species influences the orientation of the organometallic assembly and affects the activation barriers. In particular, they observed topotactic polymerization of di-iodobenzene on Cu(110) with iodine atoms sitting in rows parallel to the organometallic chains [28], while in the parallel experiment performed with bromo-iodobenzene precursors the Br atoms remain involved in the assembly and I segregates in c(2x2) reconstructed areas [14]. After the breakage of C-X bond, the reaction proceeds with a formation of organometallic intermediate between the unsaturated C atom and a surface metal atom, or a direct C-C bond formation with another dissociated precursor molecule. The split off halogens remain chemisorbed on the metal substrate and they are considered a side product which may interfere with the surface and influence the morphology of the final molecular network [14]. The strong interaction of halogens with metal surfaces was proved to often induce changes in the electronic structure, atomic arrangement and reactivity of the surface, with important drawbacks in heterogeneous catalysis [27], [29]. E.g., missing row and c(2x2) reconstructions were observed upon Cl adsorption on Cu(110) [30], while LEED patterns corresponding to a p(2x1) and c(4x2) overlayers were detected after Br_2 dissociation on Ag(110) [31]. On the other hand, it is well known that the addition of a small amount of chlorine to Ag catalyst drastically improves its selectivity towards ethylene epoxidation [29].
In the case of halogenated complexes at metal surfaces, the halogen atoms released in the dissociation process coexist with a high density of organic fragments and only seldom induce surface reconstruction [14]. They usually desorb in the form of hydrogen halide, provided that some H is made available by further dehydrogenation of the aromatic compounds [32] or even by exposure of the surface to atomic H [33]. In absence of available hydrogen, on the contrary, experimental evidence suggests that they desorb as diatomic molecules or metal halides or, in case of the small Cl atom, diffuse into the substrate [27], [31], [34].
My thesis project aimed at developing a protocol for the surface assisted synthesis of transition metal-containing (TM) carbon-based nanostructures with chemical properties optimized for applications in nanocatalysis and sensors. For this reason, I performed an experimental

investigation of the interaction of two Pd clyclometallated compounds, $C_{22}H_{14}Br_2Cl_2N_2Pd_2$ (CyPd) and $C_{22}H_{16}Cl_2N_2Pd_2$ (CyPd_2), with Ag(110). My results were then complemented by a corresponding theoretical study. The choice of Ag(110) as a substrate is due to its intermediate reactivity among coinage metals. This often allows for intermolecular interaction to prevail over molecule-surface attraction, so that uniform and extended self-assemblies may form. The CyPd and CyPd_2 complexes were chosen for their planar structure and high thermal stability, besides bearing two metal atoms/molecule. In CyPd, the organic ligand was brominated, aiming at a surface-assisted organization, as it was previously observed for bromoarenes [12], [35]. As mentioned before, there is no previous literature on this topic, so I focused my attention on the stability of the compound upon adsorption and on the change in molecular conformation. I produced the self-assembled monolayers of CyPd on Ag(110) by sublimating the molecules (synthesized by prof. A. Papagni at Università di Milano Bicocca (UNIMIB)) in ultra-high vacuum (UHV) at room temperature (RT). A scheme of the typical experiment is given in Figure **1**.

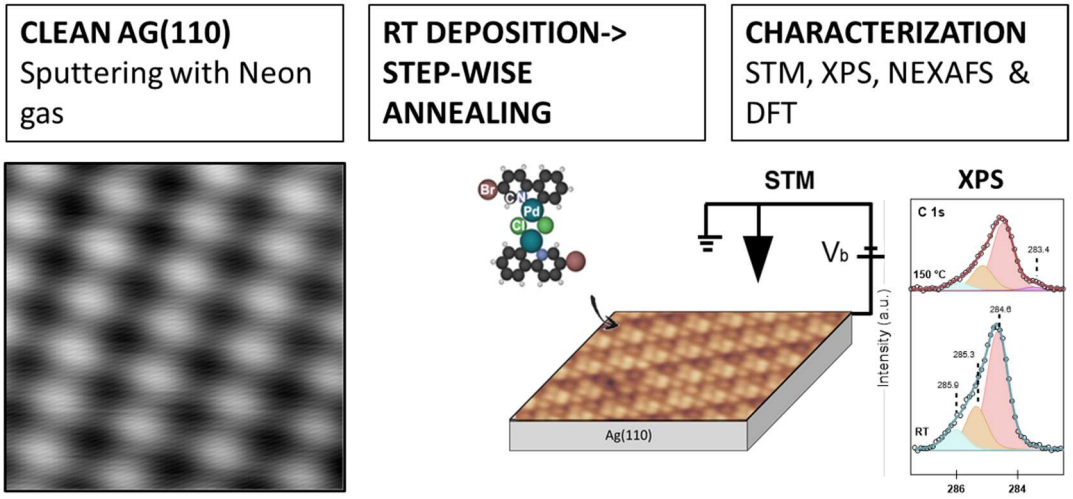

Figure 1 Schematic figure introducing the experiments.

The system was investigated by combining spectroscopic (XPS, NEXAFS, STS) and microscopic techniques (LT-STM) to understand its chemical, electronic and morphological properties. My analysis was complemented with density functional theory (DFT) modeling performed by the group of prof. Cristiana di Valentin (UNIMIB). Unfortunately, no structural analysis with diffraction techniques was performed because our low electron energy diffraction (LEED) set-up is not suitable for quantitative I-V curves but only for qualitative inspection of the surface symmetry. However, this latter information was deduced by STM at the local scale.

While I successfully deposited for the first time the Pd-cyclometallated compound on Ag(110), my results suggest that no oligomerization occurs. On the contrary, different self-assembled geometries are observed depending on deposition conditions and following annealing. For instance, experiments performed with different flux during evaporation led not only to different surface coverage (sub- vs full- monolayer (ML)) but also to different structures. The sub-ML structure was completely resolved based on chemical, morphological characterization of the

system combined with DFT calculations: the molecule splits in two fragments, the halogen atoms bind to the substrate and the Pd atoms diffuse below the surface, being replaced by Ag atoms. Therefore, the system is not suitable for catalytic applications, but it reveals an interesting chemistry due to the interaction with the metal substrate and opens new perspectives in this field of research. This work is published in [36]. The polymorphs formed at full ML coverage of CyPd on Ag(110) were investigated after stepwise annealing up to T>450 °C. Similarly to what was observed in the sub-ML, CyPd dissociated upon interaction with the metal surface, but the phenyl-pyridine (Phe-Pyr) fragments organized in a completely different way. Initially, they form organometallic complexes $(Phe\text{-}Pyr)_2$-Ag; eventually, if enough energy is provided, they undergo a cross coupling reaction producing diphenyl-bipyridine units. Interestingly, the self-assembled structures in the full ML regime are accompanied by a reconstruction of the substrate. I conclude that the halogen atoms detach from the molecules, bind to the substrate and promote a reconstruction, which is c(2x2) around the isolated $(Phe\text{-}Pyr)_2$ units and p(2x1) in areas where complete desorption of the organic part has occurred. This behavior suggests an active role of halogen species in the reorganization of the surface morphology and the work is published in [37]. To better understand the role of halogens in the surface reconstruction and the molecule-surface interaction, I repeated the experiments using the non-brominated CyPd molecule (CyPd_2), which contains only one halogen species (Cl) and has therefore a simpler structure than CyPd. I deposited CyPd_2 following the same protocol previously established and I investigated the morphology and the thermal evolution of the self-assembled layer, starting from RT until 500 °C. In this case, I observed different structures than the ones produced by CyPd. This is expected since CyPd_2 contains fewer dangling bonds than its parent molecule. I highlight that along with the molecular features, c(2x2) and a p(2x1) reconstructed Ag surface exist. The interpretation of the data, is based on the observed morphology by STM, on complementary XPS data and in comparison with the previously investigated CyPd/Ag(110) system. These results confirm that CyPd_2 also interacts strongly, dissociates at the substrate and that Cl atoms are involved in the surface reconstruction. My data suggest that Ag(110) is still too reactive to act as a support for this class of molecules. Therefore, a future development could be to use a less reactive substrate as Au(111) or an oxide layer, on which the molecules have a lower probability to dissociate and, consequently, Pd is less likely to diffuse into the bulk. Finally, I will discuss the results obtained during my three-month internship in the surface science group of prof. Federico Rosei at the Institut National de la Recherche Scientifique-INRS (Varennes, Canada). There, my acquired expertise on STM was applied to investigate the morphology and electronic structure of cadmium chalcogenide CdX (X=Se, S,) quantum dots (QDs) on Au(111) in UHV or ambient conditions.

2. EXPERIMENTAL DETAILS

2.1. Basics of Ultra High Vacuum (UHV)

A prerequisite for conducting surface science experiments is the use of UHV conditions, i.e., working at a typical pressure lower than 10^{-8} mbar. Under those conditions, the influence of residual gas molecules present in the chamber is negligible and the samples are kept clean during the time of analysis.
Moreover, UHV conditions permit experiments that involve electrons/ions as probe particle since the gas density is reduced and the probe particles can travel macroscopic distances without scattering or being absorbed by the gas molecules in the chamber.
The gas density $\frac{N}{V}$ in the UHV chamber can be estimated according to the ideal gas law:

$$\frac{N}{V} = \frac{P}{k_B T} \qquad [38]$$

Where P is the pressure of the gas, V is the volume occupied by the gas, T is the temperature, N is the total number of particles, and k_B is Boltzmann constant (1.38×10^{-23} $\frac{J}{K}$)
The mean molecular speed $\bar{c}$ for a gas of mass m is given by the Maxwell-Boltzmann distribution:

$$\bar{c} = \sqrt{\frac{8 k_B T}{m\pi}}$$

Hence, combining the above equations the Hertz-Knudsen formula is obtained. It describes the flux of molecules impinging on the surface:

$$\Phi = \frac{1}{4} n \bar{c} = \frac{P}{\sqrt{2\pi m k_B T}} \left[\frac{molecules}{m^2 s}\right]$$

The total exposure (χ), i.e., the number of molecules impinging on the surface, is a function of the gas pressure and of the exposure time. It can be expressed in SI units $Pa \cdot s$ (Pascal seconds) or in Langmuir (L) for convenience:

$$1L = \frac{3}{4} \times P\left[10^{-6} mbar\right] \times t[s]$$

Considering a base pressure in the UHV chamber P=1×10^{-9} mbar and the worst case in which all the residual gas is carbon monoxide (CO), we can estimate a CO flux of Φ=$2.88 \cdot 10^{15}$ $\frac{molecules}{m^2 \cdot s}$, which corresponds to each surface unit cell of Ag(110) (atomic surface density of 8.46 10^{18} atoms/m^2) being hit by a CO approximatively once every hour. At the temperature T=300K such exposure corresponds to a CO coverage of almost 1 Monolayer (ML) assuming sticking

coefficient=1. Since a typical experiment requires several hours, only a base pressure in the low 10^{-10} mbar range guarantees adsorption from the background to be negligible.

The pumping system

UHV is achieved by pumping gas out of the chamber via different types of pumps. The experimental set-up I used is equipped with:

- scroll pump (pumping speed 4.2 m^3 /h), that reduces the P in the chamber from 10^3 to ~ 10^{-3} mbar by mechanical compression and provides fore-vacuum for the molecular and turbo-molecular pumps.
- -molecular pump (7.5 l/s), installed between the scroll and the turbo-molecular pumps.
- a turbo-molecular pump (550 l/s) connected to the preparation chamber, which allows 10^{-8} mbar to be reached before baking.
- a separate, small turbo molecular pump is (70 l/s) used for differential pumping of the fast entry lock, the gas line, and the molecular evaporator, whenever necessary.
- a Titanium (Ti) sublimation pump combined with an Ion pump, keeping the vacuum in 10^{-10} mbar by entrapping the residual gas molecules chemically.
- cryogenic panel, condensing/absorbing the gases on a cold surface. In the preparation chamber the cryogenic panel is filled with liquid LN_2, while in the main chamber the cryogenic pumping is given by the cryostats, filled with liquid nitrogen (LN_2, 77 K) (outer part) and/or liquid helium (LHe, 4K) (inner part).

After each exposure to atmospheric pressure, the UHV system must be baked at T=125 °C for at least a day to regain the same UHV condition.

2.2. Description of the UHV SET-UP

The growth and characterization of the self-assembled layers was done *in situ*, in the UHV set-up shown in Figure 2. The set up consists of two parts separated by a built-in valve. The main chamber hosts the low temperature scanning tunnelling microscope (LT-STM) hanging from the cryostat. The preparation chamber is equipped with various preparation and analysis tools:

- The manipulator with 4 degrees of freedom (x-, y-, z-axis and rotation angle (Θ =360 °) is used to move the sample in front of the various tools for sample preparation (i.e., deposition, sputtering) or inside and out of the main STM chamber. It is also used for placing samples in the storage unit or in the fast entry lock system. Furthermore, it provides electrical and thermal connections to the sample.
- Storage unit, holding up to 4 samples and 6 STM tips. On its side there is an additional filament used to anneal W tips by electron bombardment, hence removing the oxide layer off an STM tip.
- Gas lines for controlled intake of high purity gases (Ne, CO, O_2, purity >99.99%).
- Ion gun for sample cleaning by ion bombardment with Ne^+ ions (sputtering) (see details in sample preparation section).
- Homemade Ta crucible for molecular evaporation.

- Quadrupole Mass Spectrometer (QMS) for residual gas analysis.
- A fast-lock entry (FEL) system is connected on the preparation chamber to introduce new samples/tips without breaking the vacuum.

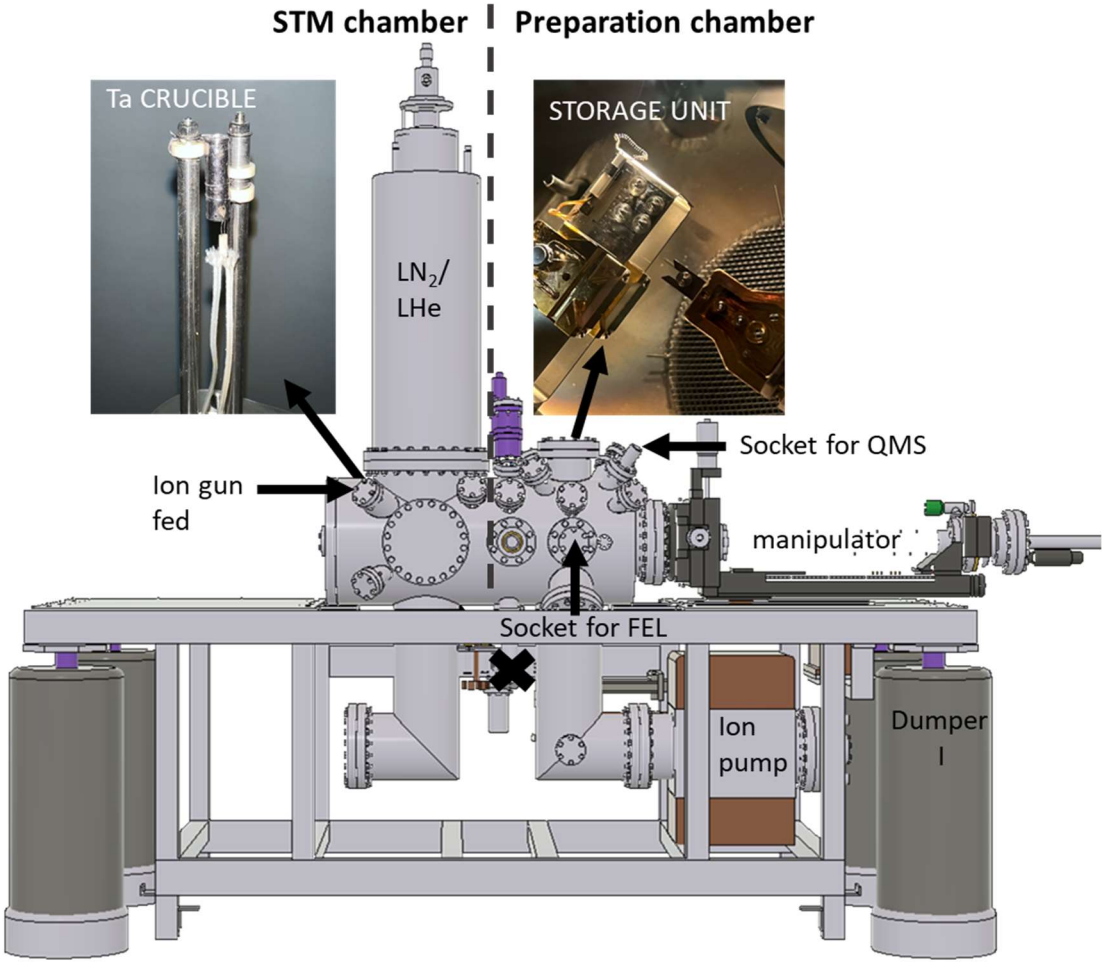

Figure 2 Scheme of the LT-STM apparatus: The STM chamber with its cryostat that consists of an outer tank (12 L) filled with liquid N_2, and an inner tank (4 L), filled with liquid He or liquid N_2. The preparation chamber hosts the manipulator, storage unit, Ta crucible (its position is indicated by black X), ion gun, fast entry lock, QMS and LEED (not visible from this side). The whole chamber rests on four dumpers.

The sample holder hosting the sample is grabbed by the manipulator via the T bar mechanism as shown in Figure 3a. On its backside, there is a ceramic plate which can provide up to six electrical connections between the sample and the manipulator or the STM. The electrical connections (pins) extend on both sides of the sample holder and are highlighted in Panel b. The sample holder is electrically isolated from the sample via two sapphire crystals that also clamp the sample in place. When the sample holder is attached on the manipulator (e.i. during sample preparation) the ceramic plate provides electrical contacts to the sample via four pins: two for heating (T up to 1000K) via Cu wires and two for the type K thermocouple (NiCr, CrAl), as shown in panel c,d. The sample I used is an Ag(110) single crystal, hat-shaped, with a polished surface

of 6mm in diameter. The thermocouple is fixed at its side. The sample can be heated up to 1000 K by passing a current as high as 3.3 A in the button heater installed below it. It is also possible to cool down the sample by fluxing LN_2 or LHe in the manipulator. When the sample is transferred with this manipulator into the STM, it is fixed inside with the hook and up to 6 electrical contacts can be established via the pins, panel c.

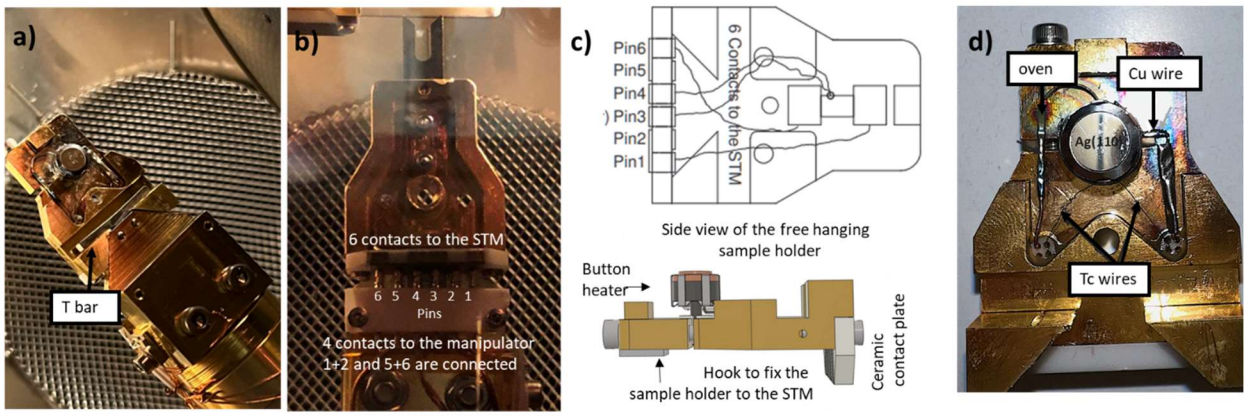

Figure 3 a) Picture of the sample holder clamped on the manipulator, (facing upwards).; b) the sample holder placed downwards, highlighting the electrical connections on the ceramic plate. c) Scheme of the electrical connections and a side view of the sample holder. d) Picture of the Ag (110) sample mounted on the sample holder with the connections for sample heating indicated.

2.3. Scanning tunneling Microscopy and Spectroscopy (STM & STS): basic principle.

Since it was invented by Binning and Rohrer in 1981 [39] the Scanning Tunneling Microscope (STM) has been widely used for surface science experiments. It works by measuring the tunneling current when a small bias voltage is applied between a conductive or semiconductive sample and a conductive tip placed few Angstroms from the surface. According to the rules of classical physics, as the tip and the sample are not in direct contact, no current can flow between them. The vacuum between tip and sample is a classically forbidden region with an energy barrier higher than electron kinetic energy. However, according to quantum mechanics, electrons can "tunnel" through the classically forbidden region due to the wavelike properties of electrons and the phenomena is known as quantum tunnelling effect.

If we treat the barrier as a simple one-dimensional (1D) approximation for one electron tunneling, we can describe the tunneling effect by splitting the model into three regions: region 1 (tip), vacuum (classically forbidden) 2, and the sample 3, Figure 4. The electron with a mass m and energy E that tunnels between regions 1 and 3 is described by a wave function ψ(r). Therefore, in region I, the electron is described by the propagating wavefunction ψ_I, in the classically forbidden region II, is described by the decaying wavefunction ψ_{II} and in region III, it is described by the propagating wavefunction ψ_{III}, past the barrier. The wave function is solution

to the Schrödinger equation and its square root$|\psi|^2$ will allow us to calculate the probability of finding the electron in the region dx.
The Schrödinger equation for region I, II and III in the presence of a barrier of height U_0 and width L can be written as:

$$\Psi_I + {k_1}^2\Psi = 0, \text{for } z < 0;$$
$$\Psi_2 - {k_2}^2\Psi = 0, \quad \text{for}, z \in [0; L]$$
$$\Psi_3 + {K_3}^2\Psi = 0, \text{for } z > L;$$

Where, the wavevector k is:

$$k_1 = \sqrt{\frac{2mE}{\hbar^2}}\ , \quad k_2 = \sqrt{\frac{2m(V_0 - E)}{\hbar^2}}$$

In region I, the solution to the wave equation can be expressed as the sum of the incident wave and partially reflected wave $\Psi_1 = e^{(ik_1 z)} + Ae^{-(ik_2 z)}$. For region III, since Z>L, the solution can be expressed as a transmitted wave $\Psi_3 = B^{(ik_3 z)}$. The solution inside the potential barrier, region II, is: $\Psi_2 = Ce^{(ik_2 z)} + De^{-(ik_2 z)}$. The coefficients A, B, C, D are determined applying the boundary conditions which require that the wavefunction and its derivative must be continuous at z=0 and z=L. From the solutions obtained, it is evident that the tunnelling current, i.e., the current of electrons reaching the point x=L, is proportional to the transmission coefficient:

$$I \propto \Psi_2 \Psi_2^* \propto e^{-2k_2 L}$$

The equation indicates negative exponential dependence of the transmission coefficient from the widths. The tunnelling current is proportional to the transmission coefficient; hence it is also exponentially dependent on the tip-sample distance. This is the physical reason why STM is so sensitive to the surface corrugation. The tunnelling current usually has values in the pico- and nano-Ampere range. For a typical value of the work function of a metal (~ 4 eV), the tunneling current reduces by a factor ~10 for every 0.1 nm increase in distance. Therefore, over an atomic diameter of 0.3 nm, the tunneling current changes three orders of magnitude.

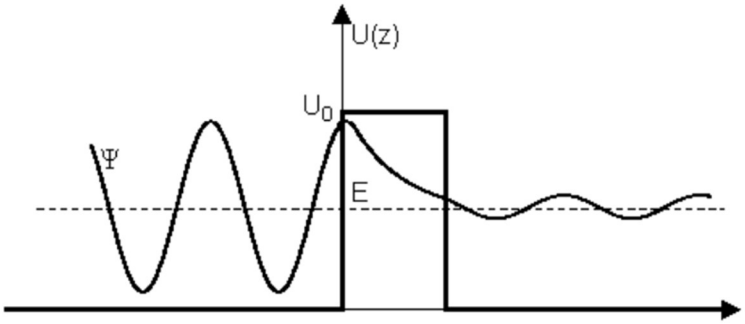

Figure 4 1D Rectangular potential barrier and particle wave function.

2.3.1. The STM SET UP

The STM used for this thesis is manufactured by CreaTec. Figure 5 shows the scanner, which is a modified Besocke Beetle type, described in details in [40]. In short, it consists of a Cu disk (ramp) containing three 120 ° sectors with a decreasing thickness from one side to the other. The ramp rests on three outer piezoes in triangular configuration through a sapphire ball which minimizes the friction. The tip is magnetically attached to the fourth piezo in the center of the ramp. To move the tip, a slip and stick movement is applied to ramp: an electric signal applied to the piezos forces the ramp to slip causing the tip to move in a certain way. The three outer piezos are responsible for larger movements over the sample (up to 1 mm) in both lateral (XY) and vertical (Z) directions. The central piezo is responsible for fine movements in tunneling conditions (tip-sample distances of a few Å). Another note about the typical setup during experiments is that the STM has the lateral (XY) and vertical (Z) movement decoupled. This means that I can use coarse movement for X and Y while maintaining fine movement for Z when scanning the sample. This setup benefits from lower distortion induced by the coarse mode and the better response of the main scanning mode for fine height adjustment, maintaining high vertical resolution.

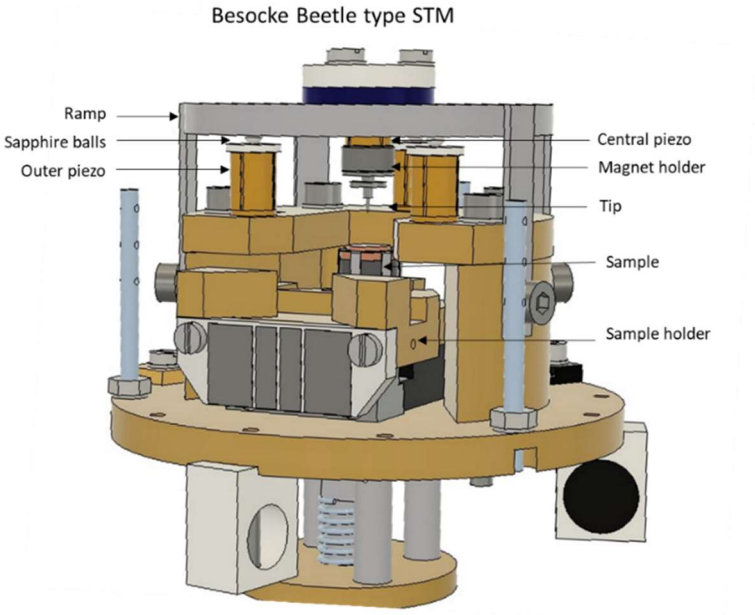

Figure 5 Scheme of the Besocke Beetle type STM.

The scanning/feedback parameters are controlled via the STM program provided by Createc. The electronics are based on a digital design. A digital signal processor (DSP) controls the scanning (XY) and the tip-sample distance (Z). Furthermore, the software has a lock-in system for spectroscopy measurements, the principle of which is explained below.

The STM can be operated in two modes: constant current or constant height. All my measurements were recorded in the constant current mode which means that the tunnelling current was measured and kept constant by a feedback system that changes the tip sample

separation distance. In this way, a map of the surface is obtained by recording the distance (z) for each coordinate (x,y). In constant height mode, the tip sample distance is kept constant and therefore the tunnelling current is varied during scanning. This mode is less used since it requires very smooth and defect free surfaces to avoid tip crashes. My images were acquired in constant current mode, using Pt/Ir tip. In the different experiments I used tunneling currents ranging between (i) 0.1 nA<i< 1 nA and bias voltages (V) –0.05 V <V< 3.8 V. STM analysis was performed using WSxM software [41].
For acquisition of atomically resolved images, good vibration isolation in STM is necessary. During scanning, the STM hangs free from the inner cryostat through three vertical springs. The springs suppress the vertical vibrations of the apparatus. Additionally, the STM and the inner cryostat have eddy current damping to suppress the horizontal vibrations. The Eddy current damping system is placed around the STM head and consists of copper plates intercalated with permanent magnets. The whole chamber sits on pneumatically damped feet to avoid low frequency vibrational noise. To further improve the data acquisition, the STM is kept at low T by thermal contact with the cryostat filled with LN_2 and/or LHe.

2.3.2. Scanning Tunneling Spectroscopy

STM can be operated in spectroscopy mode to probe the local density of electronic states (LDOS) and the band gap of surfaces.
During operation, the tip is fixed at a specific height over the sample, and the tunneling current is measured as a function of electron energy (bias voltage). This allows us to plot an I-V curve spectrum. From the slope of the I-V curve at each voltage the differential conductance (dI/dV) can be obtained, and it corresponds to the local electron density of states, the LDOS. To interpret the dI/dV measurements, usually the Wentzel-Kramers Brillouin (WKB) approximation for the tunneling current is used:

$$\boldsymbol{I = \int_0^{eV} \rho_s\,(r, E)\rho_t(r + eV - E)T(E, eV, r)dE} \qquad [42]$$

where $\boldsymbol{\rho_s}$ is the sample density of states, $\boldsymbol{\rho_t}$ is the tip density of states, and T is the tunneling transmission probability. To perform the derivative of the (total) tunneling current I=I(V), a small sinusoidal signal $V_m=V_0\cos(2\cdot \pi \cdot f \cdot t)$ ($V_0<<V$) with frequency $\boldsymbol{f}$ is added to the constant bias V to obtain $I= I(V+V_m)$ and expanding to the first order $I\approx I(V)+(dI/dV)\ V_0\ \cos(2\cdot\pi\cdot f\cdot t)$. The sinusoidal component can be extracted by a lock-in amplifier working with its reference frequency set at the modulating frequency $\boldsymbol{f}$, therefore the lock-in output is proportional to the derivative of the current, i.e., the argument of the integral evaluated at the bias voltage V.

Calibration of the STM

The STM tips used in the following experiments are prepared by cutting a 0.2 mm diameter Pt-Ir wire under strain at a grazing angle. The tip is placed on a tip holder, which is magnetically

attached to the bottom of the central piezo. The tip apex can be reshaped during measuring by controlled crashes into the clean Ag sample. The sharpness of the tip is evaluated based on the quality and resolution of the STM images.
Calibration of the STM images is necessary to determine the image dimensions, which is done by calibrating the piezoelectric constants against the lattice parameters of Ag (110). The piezo constants are the conversion factors between the voltage applied to the piezos and the distance covered by the tip and must be adjusted according to the formula:

$$Cpiezo(new) = Cpiezo(old)\frac{d}{d_{meas}}$$

Their value depends on the working temperature of the STM, since both the lateral and vertical movement are related to the physical deflection and compression of the piezo components of the tip assembly, which decreases for any given voltage at lower T. Therefore, the calibration process needs to be performed both at LN_2 and at LHe temperature. Calibrating consists of recording atomically resolved STM images of the Ag(110) surface lattice and assuming that primitive unit cell dimensions in the <1-10> and <001> directions are 0.28 and 0.40 nm, respectively, based on X-ray diffraction measurements.
Figure 6a. shows atomically resolved STM image of the Ag(110) surface, taken at LHe. The grey and black traces indicate the <1-10> and <001> directions, respectively. Panel b) shows that the corresponding measured periodicities are 0.28 nm (along <1-10>) and 0.43 nm, (along <001> direction). Then to calibrate the image dimensions, I determined the correction factors from the ratio between the measured and tabulated values for Ag lattice. Because the difference between the established primitive cell dimensions with the values taken experimentally differ by about 5%, this is within the acceptable uncertainty of the instrument and the STM is calibrated for use. The same procedure was performed in Z-direction, considering the height of monoatomic Ag steps, which should be 0.14 nm. The calibration was checked and adjusted for scanning at LN_2 temperature.

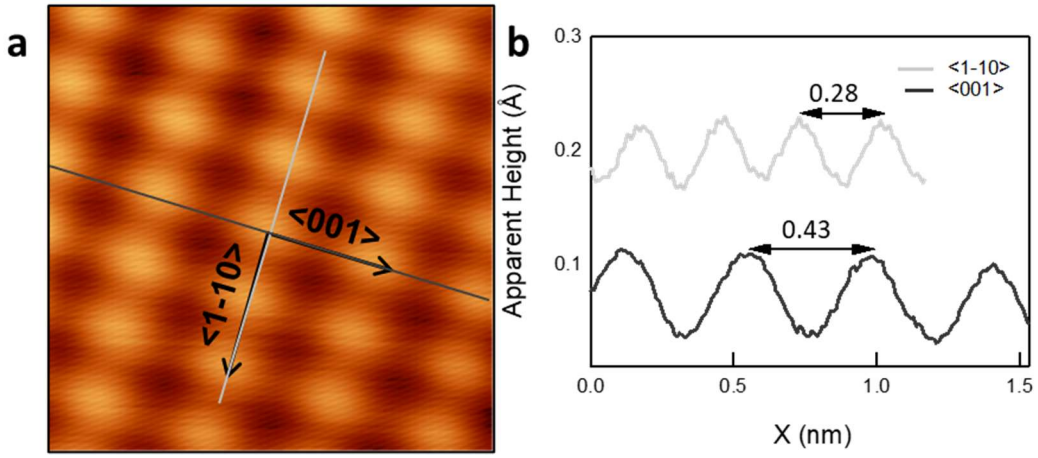

Figure 6a) Atomically resolved STM image of a clean Ag(110) surface taken at LHe temperature. The grey and black trace indicate the <1-10> and <001>, respectively, and are used to calibrate the piezoelectric constants. The corresponding measured periodicities are reported in the apparent height profile in panel b).

2.4.High Resolution- X-ray Photoemission spectroscopy (HR-XPS) and Near Edge X-Ray Adsorption Fine Structure (NEXAFS)

The HR-XPS and NEXAFS were performed at the ANCHOR-SUNDYN end-station of the ALOISA beamline at the Elettra synchrotron radiation facility in Trieste, by Dr. Letizia Savio and Dr. Marco Smerieri.
Firstly, I will describe the physical principle behind the two techniques. Then I will discuss the experimental conditions and measurement for each of them.

2.4.1. X-ray Photoemission spectroscopy: basic principle

X-ray photoelectron spectroscopy (XPS) is a technique which exploits the photoelectric effect caused by X-rays to gain information on the chemical composition and oxidation state of surfaces [43]. A scheme of the XPS process is shown in Figure 7a: a core level photoelectron is emitted from the atom, above Fermi level, when the atom absorbs a photon.

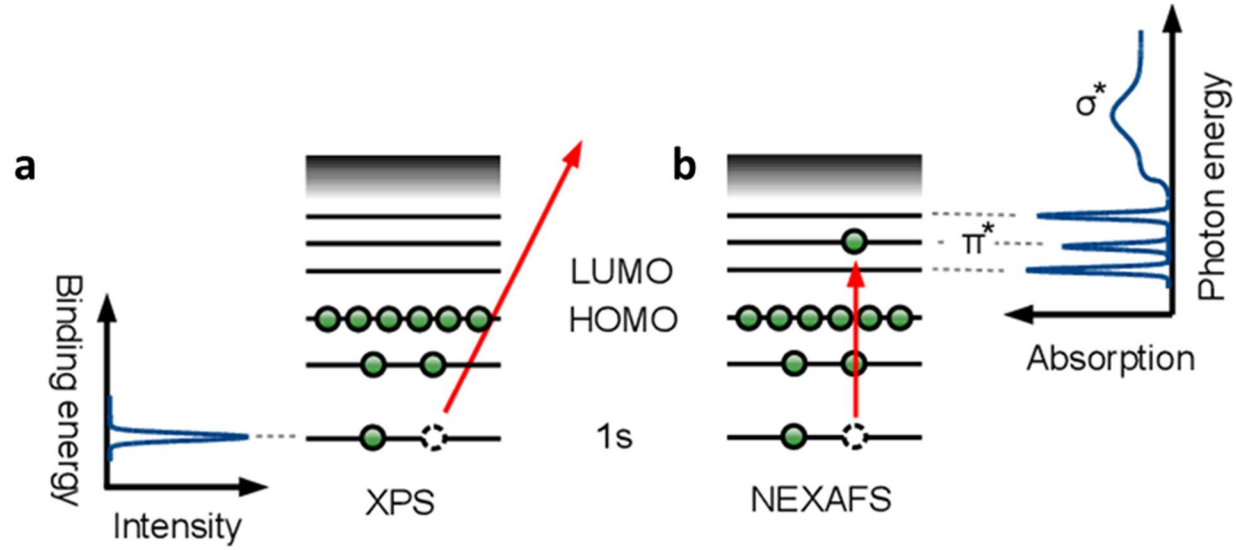

Figure 7 Excitation principle of XP and NEXAFS spectroscopy. Absorption of X-rays causes either emission of core level electrons (XPS) into vacuum (panel a) or excitation into unoccupied molecular π ∗ and σ∗ states (NEXAFS, panel b). The schematic spectra show the relation between adsorbate states and peaks in the spectra. Scheme taken from [44].

Following the energy conservation principle, in the single particle limit the kinetic energy (KE) of the emitted photoelectrons can be calculated as:

$$KE = h\nu - BE - \varphi \qquad [43]$$

Where BE is the binding energy of the electron, φ is the work function of the analyzer, $h\nu$ is the energy of the incoming photon. In principle both $h\nu$ and φ are known parameters, and by measuring KE, information of the binding energy (BE) of the atoms is obtained. Every electron shell of every element has a specific BE, thus with XPS it is easy to determine the chemical

species present on the surface. Furthermore, the core level peaks can undergo small binding energy shifts (by few eV) depending on the chemical environment of the atom which photo-emits the electron, hence providing information about the different oxidation state of elements. XPS is also a quantitative technique, i.e. the intensity of the photoemission peaks is proportional to the amount of probed atoms. Therefore, by considering the sensitivity factor for each element it is possible to determine the relative concentration of species present in the sample.
Some other observable processes in XPS include: the photon-induced Auger peaks, valence band electrons, inelastic scattering processes and other features like shake-up and shake-off satellites. Some of them can be important for interpreting the spectra.

XPS is a surface sensitive technique because of the short inelastic mean free path (IMFP) of electrons, i.e the average distance that electrons can travel in a solid before undergoing collisions with lattice defects, phonons or with other electrons, Figure 8. The universal curve indicates that the highest surface sensitivity, approx. 2 ML, is achieved for electrons with kinetic energy E_k=50 eV and it increases up to 10 ML for electrons with 1000 eV energy.

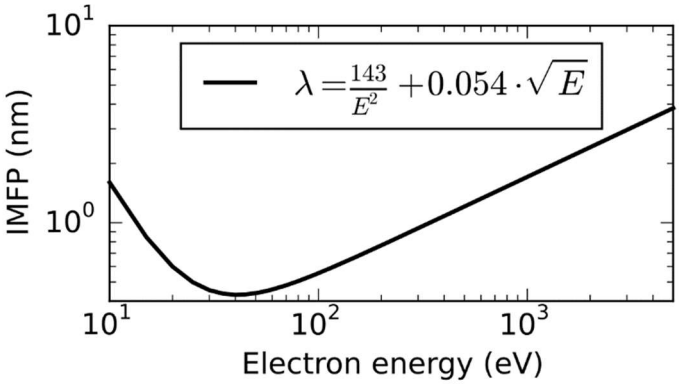

Figure 8 Universal curve for the Inelastic Mean free path of electrons.

The XPS results regarding the CyPd complex, were recorded by my group at the ANCHOR endstation connected to the ALOISA undulator beamline of the Elettra Synchrotron Light Source in Trieste. On the other hand, I performed the XPS measurements of the CyPd_2 compex in our UHV chamber at University of Genoa.

2.4.2. NEXAFS: Basic principle

Near Edge X-Ray Absorption Fine Structure (NEXAFS) is a type of absorption spectroscopy. It requires tunable photon source (synchrotron radiation) to probe transitions between core levels and unoccupied molecular states. Details about the principle and applications are reported in [45], [46].
An example of NEXAFS spectrum is given in Figure **7**b. In NEXAFS, absorption of X-rays may excite an electron into an unoccupied state (bound) or in the continuum of unbound states. The de-excitation of electron occurs then by Auger electron emission, or by florescence, thus

emitting a photon. Hence, spectra of the emitted Auger electrons (electron yield) or of the fluorescent yield can be recorded. The cross section of these two processes depends on the atomic number of the elements probed and, on the edge, considered. For elements with low atomic number Z (N, C, O atoms), the Auger decay process is favored [47]. NEXAFS spectra are recorded by varying the photon energy around the absorption edge of an element, in contrast to XPS, where the photon energy is fixed, and the KE of electron is measured. The position, shape, and intensities of the peaks in the NEXAFS spectrum allow us to understand the changes in the chemical environment of the atoms and give information about the electronic properties of the system. NEXAFS measurements are also sensitive to the molecular orientation on surfaces. This is because the technique relies on dipole selection rules, associated with a photoelectron originating from a K edge (s initial state) that is excited into p-like orbital (final state, antibonding orbital). For a diatomic molecule, the antibonding orbitals can be π* or σ* type. Since they exhibit different directionality, the π* resonance has opposite polarization dependence to that of the σ* resonance.

2.4.3. HR-XPS and NEXAFS measurements:

XPS and NEXAFS spectra were plotted and analyzed using the IGOR Pro software (version 6.37, by WaveMetrics Inc.) and the XPSMania2 fitting routines developed at the ALOISA beamline in Trieste.

The base pressure in the chamber was 3.10^{-10} mbar. XP spectra were recorded with Phoibos 150 hemispherical electron analyzer (SPECS manufacturer) at normal emission, using a photon energy hv=515 eV for the *Br 3d, C 1s, Pd 3d, Cl 2p and N 1*regions. All the spectra are plotted as intensity (counts) vs BE. The BEs were calibrated on the Fermi edge, corresponding to BE=0 eV. After calibration, the Ag $3d_{5/2}$ line of the clean surface was found at BE=368.21 eV, in agreement with literature data [48]. All the other regions of one spectrum were rigidly shifted accordingly. The curves were fitted with Doniach-Sunjic line shapes convoluted with a Gaussian profile after subtracting a linear background. The error of ±5 % is estimated for the fitted intensities. Up to four components were necessary to reproduce the C 1s region, while only two were sufficient for the N 1s peak. Ag 3d, Pd 3d, Cl 2p and Br 3d regions were fitted with doublets considering the spin-orbit splitting. The instrumental resolution was 0.15 eV, as determined from the Fermi edge. The NEXAFS spectra were acquired in Auger electron yield mode recording C and N KVV Auger electrons with the hemispherical electron analyzer fixed at a kinetic energy of 262 eV and 385 eV for the C and N K-edges, respectively. A two-step normalization process is used for the spectra. Firstly, a multiplication factor is applied to scale the intensity before the energy threshold to the one of the clean surfaces. This is to correct for unwanted variations of the X-ray beam intensity. Then, the ratio between the so-normalized spectrum and the spectrum of the clean surface is plotted [45]. This is to reduce the signals due to impurities and substrate, leaving only the contributions of the adsorbates in the signal.

2.5.The quadruple mass spectrometer (QMS)

The quadruple mass spectrometer (QMS) is used to determine the composition of the residual gas present in the chamber and to check the purity of the gases that will be introduced by the gas inlet. It consists of four parallel rods of circular or hyperbolic cross-section, connected to a radiofrequency (RF, Vcos(ωt)) and direct current (DC) potential (U)[49], as shown in Figure 9. The working principle is as follows: The neutral gas molecules are firstly ionized by an ion source consisting of a hot filament (cathode), which emits electrons. The emitted electrons are accelerated to several tens of volts towards the central QMS axis, and they ionize the molecules by collision. The ions are accelerated and focused by electrostatic lenses towards the rods. The stability of the trajectory of the ions passing through the fields depends on their mass-to-charge ratio. Since the voltages define the field, they can be set such that only ions with single-mass-to-charge ratio is stable and can reach the detector. Ions with mass-to-charge ratios that are too small or too big have unstable trajectories and will collide with the rods. Hence, varying the RF allows scanning over all masses, thus obtaining the mass spectrum of the residual gas present in the UHV chamber.

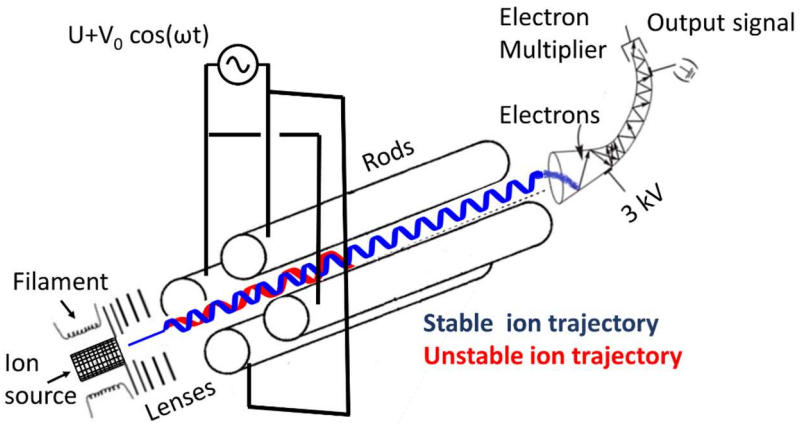

Figure 9 Schematic diagram of a quadrupole mass spectrometer.

2.6.Density Functional Theory (DFT)

DFT is an ab initio theory that investigates the electronic structure of many-body systems at their ground states. It uses functionals i.e. spatially dependent electron density n(r) along with correlation effects, and exchange effects. This computational technique is based on two Hohenberg-Kohn theorems. The first one states that the electron density can uniquely determine the properties of a system. The second one states that the ground state energy can be obtained if the input density is the true ground state density. DFT calculations were performed using the plane-wave based Quantum ESPRESSO package (QE) [50]–[52] by our collaborators in Milano, Danielle Perilli and Christiana Di Valentin. The ultrasoft pseudopotentials were adopted to describe the electron-ion interaction with Ag (4d, 5s), Pd (4d, 5s), C (2s, 2p), N (2s, 2p), Cl (3s,

3p), Br (4s, 4p), and H (1s), treated as valence electrons. Energy cutoffs of 45 Ry and 360 Ry (for kinetic energy and charge density expansion, respectively) were adopted for all calculations. For the electron exchange-correlation [53], The Van der Waals density functional vdW-DF2C09x were used. This gives an accurate description of the adsorption energies and distances of graphene on metal surfaces [54]. It has also been successfully applied to describe self-assembly of other halogenated precursors such as brominated tetracene (DBT) on different metal surfaces [35], [55], [56]. For the simulation of the Ag(110)-supported CyPd (CyPd/Ag), a (2√3a × 3√3b)R55 supercell was used, where a and b are the lattice vectors of the Ag(110) unit cell (2.88 Å and 4.07 Å, respectively, in perfect agreement with the experimental values).The geometry relaxation of all considered systems was performed with a 4 × 2 × 1 Monkhorst-Pack k-points mesh [57], followed by a non-self-consistent field (NSCF) calculation with a 12 × 6 × 1 Monkhorst-Pack k-points mesh for evaluating the electronic properties.The Ag(110) surface was modeled by a three-layer slab. The bottom layer was fixed to the bulk positions during the geometry relaxation to mimic a semi-infinite solid. A vacuum space of about 25 Å in the direction perpendicular to the surface was used, to avoid interactions between periodic images. STM simulations were performed using the Tersoff-Hamann approach [58], according to which the tunneling current is proportional to the energy-integrated Local Density of States (ILDOS). STM images were rendered with Gwyddion software [59]. The constant-current and voltage values for the STM simulations were chosen to match the experimental values.

2.7. Sample preparation/experimental protocol

2.7.1. The precursor molecules: CyPd and CyPd_2

During my Ph.D. I used two organometallic precursors: $C_{22}H_{14}Br_2Cl_2N_2Pd_2$ [(2-[2-{3-bromopyridyl}]phenyl)palladium chloride tetramer] (CyPd) and its parent molecule $C_{22}H_{16}Cl_2N_2Pd_2$ (CyPd_2). Their molecular structure is shown in Figure 10. The precursors present a two chloro-bridged structure. They contain two L type nitrogen (N) hetero atoms in the geminal positions. The N atoms stabilize two palladium (Pd) centers due to their strongly donating nature. CyPd is brominated in the 2-position of the heteroatom, while CyPd_2 is hydrogenated. The molecules were synthetized in Milano (UNIMIB) by the group of A. Papagni according to the procedure of Yian Shi et al. [60], described below, while I was responsible for their deposition on Ag(110) in UHV.

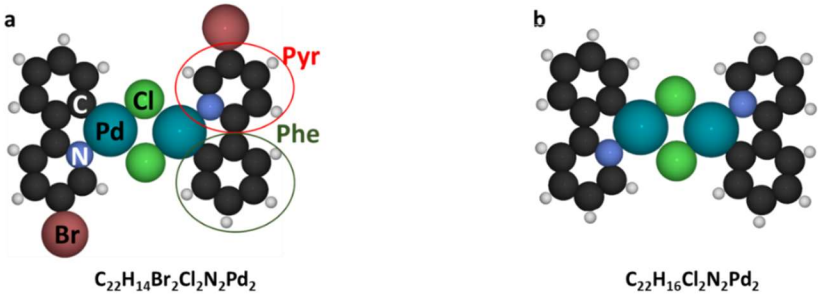

Figure 10 The molecular Structures of the precursors used in this thesis: a) $C_{22}H_{14}Br_2Cl_2N_2Pd_2$ [(2-[2-{3-bromopyridyl}]phenyl)palladium chloride tetramer] (CyPd). b) $C_{22}H_{16}Cl_2N_2Pd_2$ (CyPd_2).

All the reagents and solvents used for the synthesis of the molecular precursors, were purchased commercially (Fluorochem Co.; Tokyo Chemical Industry Co. and Aldrich Chemical Co.) and used as received. The CyPd complex was synthesized according to the procedure of Yian Shi and coworkers [60]: $PdCl_2$ was reacted with a slight excess (1:1.05) of 5-bromo-2-phenylpyridine in $CHCl_3$, at a temperature of 100 °C (sealed tube, inert atmosphere) for 24 h. The precipitate formed was recovered by filtration and washed extensively with $CHCl_3$ to afford CyPd in a pure form (402 mg, 95%) as highly insoluble yellow solid. The non-brominated CyPd_2 compound was synthesized according to a similar procedure, described in ref [61].

Preliminary study of the powders was done by thermogravimetric analysis (TGA), Fourier Transform Infra-red spectroscopy (FT-IR) and XPS to check for their thermal stability and chemical composition. The samples were tested "as received" and after deposition in UHV, to verify the absence of any thermal degradation.
The TGA analysis was performed with a Mettler Toledo TGA/DSC1 StarE instrument. Elemental analysis was obtained with an Elementar vario MICRO cube instrument. The TGA spectra of Figure 11 suggest that the decomposition of molecular precursor occurs at T_{dec}= 355 °C (CyPd) [62] and at T_{dec}= 330 °C (CyPd_2).

Melting point was measured with a Stanford Research Systems Optimelt apparatus. ATR FTIR spectra were recorded with a PerkinElmer Spectrum 100 FT-IR spectrometer equipped with a universal ATR sampling accessory or a Thermo Fisher Scientific Nicolet iS20 FTIR spectrometer. The spectra are shown in Figure 13.

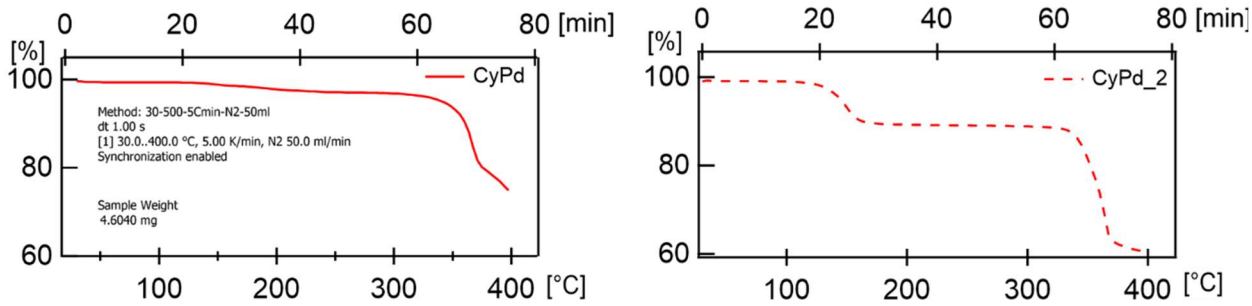

Figure 11 TGA analysis of CyPd (left) and CyPd_2 (right) powders. The CyPd has a mass loss at temperature lower than the decomposition temperature, due to solvent evaporation, while CyPd_2 has a first decrease due to the crystallization solvent.

XPS spectra show comparison between the "fresh" CyPd powders (red curve) and after several sublimation cycles (black curve), Figure 12. They are compatible indicating that no degradation of the molecule has occurred upon deposition in UHV. The slightly larger shape of the fresh CyPd spectra is due to limited charging effects during the acquisition of the spectrum. I emphasize that a measurable Pd signal is observed in the used powders.

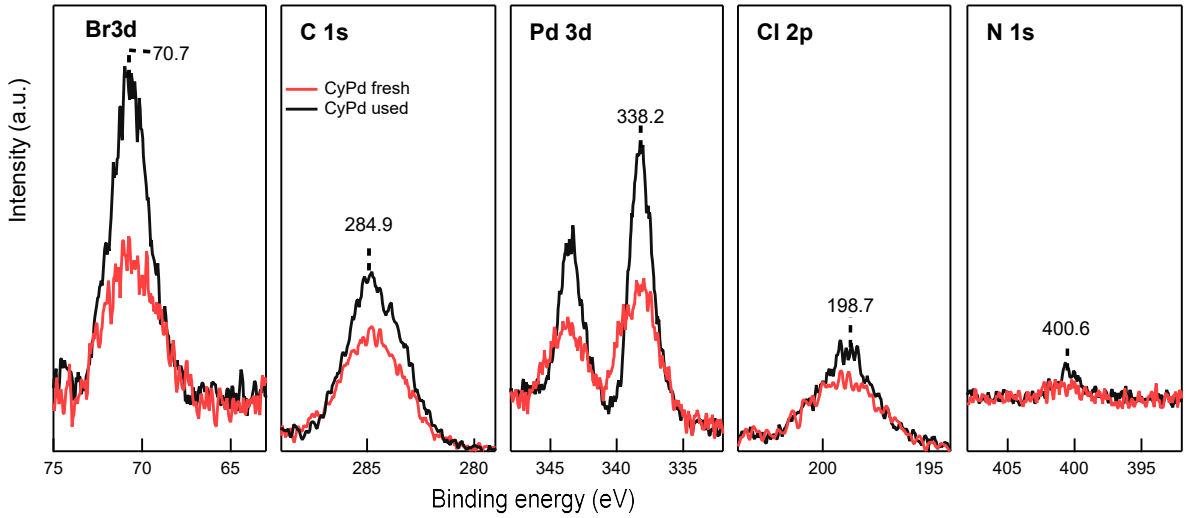

Figure 12 XPS spectra of CyPd powders as prepared (red traces) and after several sublimation cycles (black traces). The spectra are recorded with XPS, hemispherical analyzer model 10–360 and monochromatic X-ray source model 10–610 by Physical Electronics.

Table 1 shows the stoichiometric ratio between the different elements of the CyPd powders before and after sublimation in UHV. The stoichiometry was calculated weighting all fitted intensities with respect to the cross section of the corresponding line and to the transmission function of the analyzer. I firstly observe that the strong excess of C observed in the powders is due to contamination. In fact, the powders were fixed on the sample holder using a Cu tape and were not baked before being inserted in the analysis chamber. Similarly, an excess of Cl is present in the new powders. I believe that it is due to some residue of chloroform, which was used as a solvent during the synthesis. Coherently, C excess is reduced, and Cl excess is almost completely removed for the used powders, which were outgassed in UHV several times. Br and Pd atoms are present in stoichiometric ratio with respect to N, i.e., with respect to the number of phenyl-pyridine units. This confirms the integrity of the molecules both before and after use.

Table 1 Stoichiometric ratio between the different elemental constituents of the CyPd powders before and after sublimation in UHV.

	C 1s/N 1S	Cl 2p/N 1s	Br 3d/ N 1s	Pd 3d/ N 1s	Br 3d/ Cl 2p
Nominal value	*11*	*1*	*1*	*1*	*1*
Powders new	*14.51*	*1.64*	*1.26*	*1.24*	*0.77*
Powders used	*13.27*	*1.26*	*1.15*	*1.14*	*0.91*

In concurrence with the XPS analysis, the ATR-FTIR of the CyPd powders as prepared and after several sublimation cycles are almost identical, indicating that no degradation of the molecule has occurred.

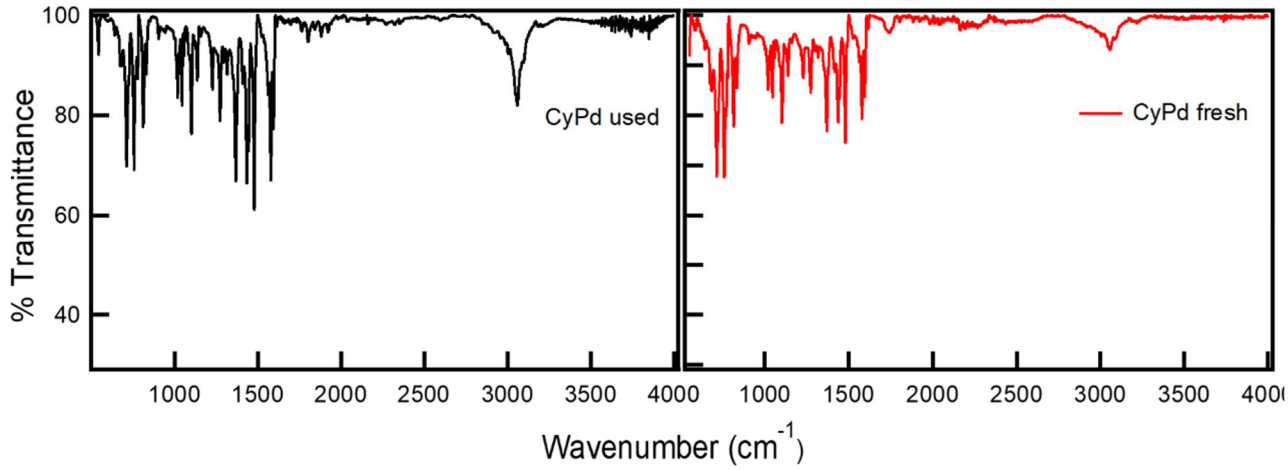

Figure 13 FTIR ATR spectra of CyPd molecules in the 1650-550 cm-1 region. The spectra compare the CyPd Powder as prepared, recorded with a Perkin Elmer Spectrum 100 FTIR spectrometer and after several sublimation cycles in the crucible, recorded with a Nicolet iS20 FTIR spectrometer.

The sample preparation consists of three steps:
1) Cleaning the Ag substrate by cycles of sputtering and annealing
2) Deposition of the previously outgassed precursors onto the clean Ag by sublimation in UHV.
3) Annealing of the self-assembled layers to test their thermal evolution. The parameters were optimized for each set of experiment and are detailed in the next section.

2.7.2. Sample cleaning by ion bombardment (sputtering)

Prior to each experiment, the sample was cleaned in-situ by ion bombardment (sputtering) followed by thermal heating (annealing). The ion beam is produced inside an ion gun. Thermal electrons emitted from W filament (cathode) are accelerated by an anode grid at a positive potential with respect to the filament. The electrons ionize the inert gas (Ne or Ar) present in the volume between the filament and the anode. The so-produced noble gas ions are accelerated and focused onto the sample surface with a kinetic energy between 1 and 3 keV. When the ion beam impinges on the surface, the topmost layer atoms of the surface are removed together with contaminants, Figure 14. After the sputtering cycles, the surface remains disordered and rough, and it is necessary to anneal it to restore the surface order.

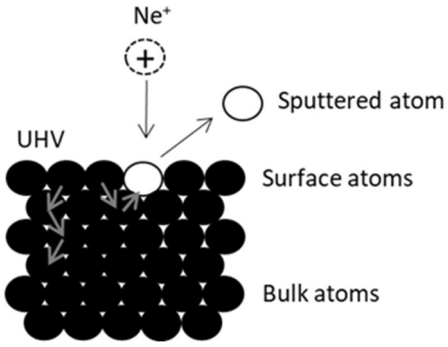

Figure 14 The Sputtering process.

The optimization of the sputtering and annealing procedure is based on the instrumentation used as well as on the sample and on the setup geometry. In my experiments, the Ag substrate was cleaned using a Ne pressure P_{Ne+}=3.5x10^{-5} mbar and usually performing three sputtering cycles of 1h each. The Ne ions were impinging onto the sample $\pm$45° off with respect to the surface normal with KE of 3, 2 and 1 keV at each cycle, respectively. The high beam energy was for effective sputtering and low beam energy to achieve less rough sample surface. The sputtering current focused on the sample was 1.6 μA or higher. After each sputtering cycle, the sample was annealed to 850K for 10 minutes, and then slowly cooled down to favor the formation of large extended terraces. Surface cleanliness was checked by STM and/or by XPS, while surface order was controlled by inspection of STM images.

2.7.3. Deposition of molecular precursor on Ag(110)

The molecules were sublimated from a Ta crucible, which was differentially pumped and baked to 100 °C for one night after insertion of the molecules. Then, before each sublimation cycle, the molecules were further outgassed in the main chamber to desorb undesired contaminants (H_2O, CO_2) by keeping them at 100 °C until a base pressure in the low 10^{-9} mbar range was recovered. The residual gas in the chamber was checked with a mass spectrometer. Then, the sublimation temperature was raised to T_{sub}= 130 °C (CyPd) or 100 °C (CyPd_2) and the precursor was sublimated on clean Ag(110) at RT for 30 min. I note that the evaporation temperature for CyPd_2 is the same as the degassing T. This T_{sub} was chosen considering the rather large size of the molecules and their thermal stability, determined from TGA. It is therefore a compromise to have a reasonable sublimation rate without causing degradation or reaction of the compound inside the crucible.

After deposition, the Ag(110) sample was step-annealed for 5 minutes up to a maximum temperature T=450 °C (CyPd) or T=500 °C (CyPd_2) to investigate the thermal evolution of the CyPd/CyPd_2 layer. At the end of each step of the preparation, the sample was slowly cooled down to RT and transferred inside the STM for measurements.

3. RESULTS: C_YP_D/AG(110)

In this chapter, I will discuss the different self-assembled structures formed in two different experiments (sub-monolayer and full monolayer coverage). First, I mention that the deposition parameters (sample temperature, CyPd sublimation temperature and deposition time) were nominally the same in both experiments, however they resulted in a different coverage. The coverage depends on the molecular flux arriving at the surface, which is related to the change in the background pressure in the chamber. During evaporation the background pressure is changing with time, and it generally decreases after several sublimation cycles. Therefore, when the background pressure during deposition was lower (meaning lower flux), I reached sub-ML coverage of CyPd on Ag. On the contrary, when the molecules were better outgassed (after several depositions) the background pressure was higher, and a full ML coverage was obtained.

In this context, the CyPd/Ag (1 1 0) section is dividend in two parts:

- Sub-ML coverage
- Full ML coverage

3.1. Introduction

CyPd molecules were deposited *in situ* from the Ta crucible. I performed deposition at different flux for the same time (30 min), and I obtained different coverage. Low flux resulted in sub-ML coverage, while at higher flux a full ML of CyPd covered the Ag(110) surface. At the different coverages different self-assembled structures are observed. This is because the kinetics of the self-assembly process plays a role in determining the final structure. If the flux is low, the molecules arrive on the surface and have time to dissociate, diffuse and interact with Ag atoms. Increasing the flux, the mobility of molecules/fragments is reduced and the probability of inter-molecular interactions during the formation of the self-assembly gets larger and may lead to completely different arrangement, as discussed in the following. The goal of the experiment is to study the chemistry and morphology of the different polymorphs after RT deposition and after thermal annealing.

At sub-ML coverage, only one structure is found, and it is completely resolved based on its chemical and morphological characterization combined with DFT calculations: the molecule splits in two fragments, the halogen atoms bind to the substrate and the Pd atoms diffuse below the surface, being replaced by Ag atoms. Therefore, the system is not suitable for catalytic applications, but it reveals an interesting chemistry due to the interaction with the metal substrate and opens new perspectives in this field of research.

On the other hand, at full ML coverage, different polymorphs of CyPd form on Ag(110). They were investigated after RT deposition and stepwise annealing up to T>450 °C. Similarly to what was observed in the sub-ML, CyPd dissociated upon interaction with the metal surface, but the

phenyl-pyridine (Phe-Pyr) fragments organize in a completely different way. Initially, they form organometallic complexes $(Phe\text{-}Pyr)_2$-Ag and if enough energy is provided, they may undergo a cross coupling reaction producing diphenyl-bipyridine units. Interestingly, the self-assembled structures in the full ML regime are accompanied by a reconstruction of the substrate. I conclude that the halogen atoms detach from the molecules bind to the substrate and promote a reconstruction, which is c(2x2) around the isolated $(Phe\text{-}Pyr)_2$ units and p(2x1) in areas where complete desorption of the organic part has occurred. This behavior suggests an active role of halogen species in the reorganization of the surface morphology.

3.2. Sub-ML coverage CyPd/Ag(110)

The sub-ML CyPd/Ag(110) system is characterized upon deposition of the molecules at RT and subsequent annealing up to 150 °C. The morphology and electronic structure are derived from STM and STS measurements, respectively, and they are supported and interpreted in parallel with complementary spectroscopic (XPS and NEXAFS) and DFT analysis.

STM images were recorded at liquid nitrogen (LN_2,77K) or liquid helium (LHe, 4k), using a Pt/Ir tip. The images were acquired in constant current mode, with typical tunneling currents 0.1 nA$\leq$ I $\leq$0.8 nA and a bias voltage range -2.0 V $\leq$ I $\leq$ +2.0 V applied to the sample.

3.2.1. STM analysis

Deposition of CyPd on Ag(110) at RT leads to the formation of extended self-assembled layers as the one shown in the overview of Figure 15. Firstly, I mention that no isolated molecules are observed on the surface, while bare Ag(110) patches may coexist with fully covered areas depending on the total coverage achieved. On the other hand, no traces of multilayer have been observed in the present experimental conditions. This indicates that CyPd adsorption is a self-limiting process, that an attractive interaction among molecules is present and that at RT they are mobile enough to diffuse on the surface until they nucleate or join a self-assembled island of molecules. The 2D-network consists of lozenge-shaped features assembled in a double row-structure. The rows are oriented at ±(60°±3°) off the <1-10> direction

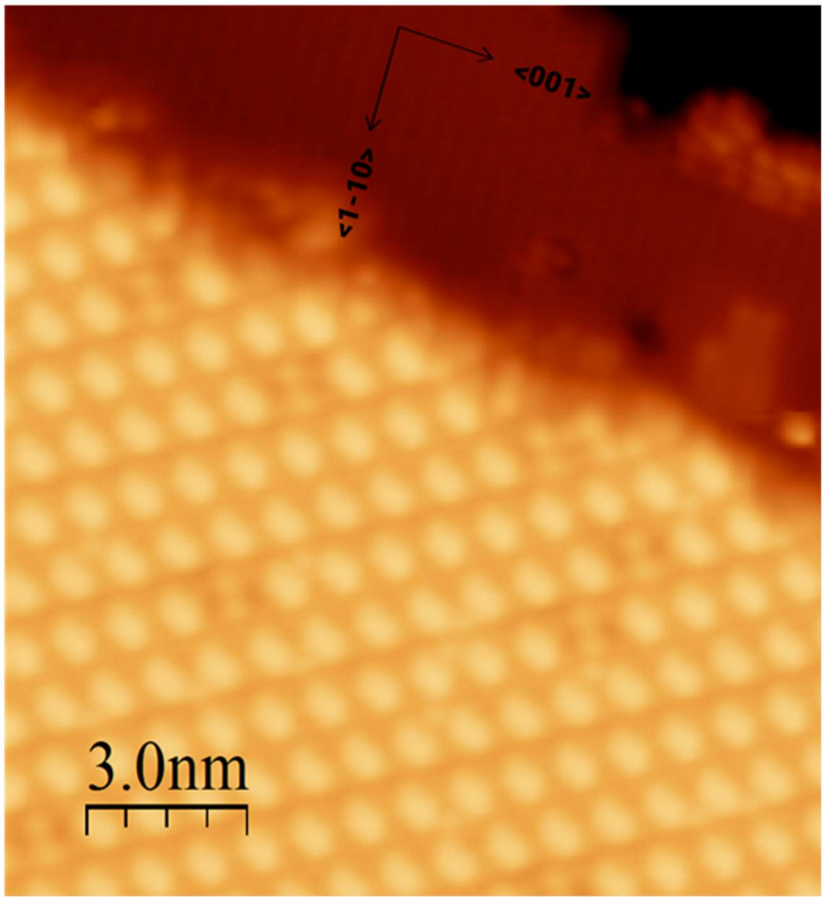

Figure 15 *Overview STM image recorded after 30 minutes deposition of CyPd on Ag(110) at RT. V =-0.5 V, I= 1.2 nA,, imaging at 4 K*

Panels a and b compare the morphology of the CyPd/Ag(110) sample as grown at RT and after annealing to 150 °C. The enlarged STM image in panel a) evidence that each lozenge consists of four smaller lobes arranged in a rhomboidal shape and it is surrounded by some interstitial dots. After annealing to T=100 °C (not shown) and to 150 °C (panel b) no significant morphological changes are observed in the layer. Statistical analysis taken over several equivalent images and of line scans as the ones reported in panel c, allow me to determine the typical periodicities of the self-assembled geometry and draw the unit cell marked in panel a. The average of the measurements obtained over different preparations are given in Table 2. At RT, the unit cell is nearly rectangular with vectors a=(0.97 ± 0.04) nm and b=(2.01 ± 0.10) nm aligned along the rows and perpendicular to them, respectively. The unit cell parameters are compatible within the error for the sample as grown and after annealing (panel d), confirming the intuitive indication that the observed self-assembled geometry is stable in the investigated temperature range. I mention that a smaller unit cell is not possible since the pairs of rows are slightly misaligned and the separation between one row and the next is not the same on either side. Each unit cell contains two lozenge-shaped features and four smaller and fainter dots. By comparing the experimentally determined values of the unit cell with the expected molecular dimensions of the isolated CyPd molecule (1.34 nm long and 1.05 nm wide), I estimate a population of one molecule

per unit cell, corresponding to a local coverage of (5.1± 0.1)·10^{13} molecules/cm^2. The two large features could thus correspond to the two halves of the molecule, while the nature of the dots is less straightforward. From a comparison with previous literature on halogenated aromatic systems on the same surface [12], [35], they can be tentatively assigned to dissociated Br atoms and/or Ag adatoms taken from the substrate, but this hypothesis needs to be verified due to the larger complexity of the CyPd/Ag(110) system. Moreover, I note that the structure of CyPd consists of two equivalent parts rotated by 180° with respect to each other. While this should reflect in the STM image of the molecule, careful inspection of the high-resolution images of Figure 16 a and b show that all the lozenges have the same shape and orientation.

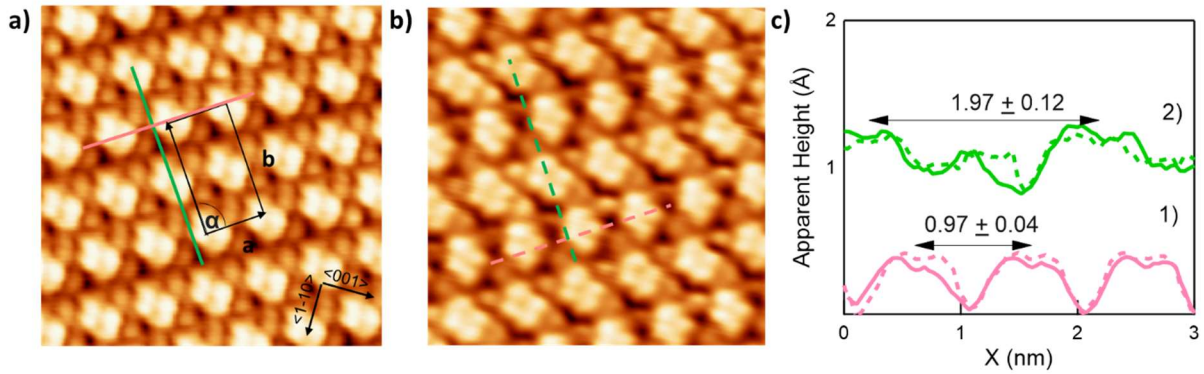

Figure 16 a) STM image of the self-assembled layer formed by the CyPd molecule deposited on Ag(110) at RT (Imaging at 4 K). The unit cell is marked by the black rectangle. b) Same as panel a) after annealing the layer to 150 °C for 5 minutes (Imaging at 80 K). In both cases, image size: 6x6 nm^2, V= -0.1 V, i=0.1 nA. Panel c) Height profiles cut along the pink and green traces in panels ab), corresponding to the unit cell directions a and b, respectively.

Table 2 Table summarizing the unit cell parameters of the double-row structure at the different T.

Double row structure	RT	100 °C	150 °C
Unit cell parameters	a=(0.97±0.04)nm	a=(0.94±0.01)nm	a=(0.94±0.03)nm
	b=(2.01±0.10)nm	b=(2.13±0.01)nm	b=(2.00±0.12)nm
	α=(86±3)°	α=(90±1)°	α=(89±1)°
Orientation wrt <1-10>	±(60±3)°	±(60±3)°	±(60±3)°

The bias dependence of the structures obtained at RT is shown in Figure 17. The same region is acquired at different bias voltage in the range -1.5 V ≤V≤+1.5 V. Firstly, I notice that the molecules change their appearance with bias, which is indicative of some modulation of the local DOS. In more details:

- At negative bias (imaging filled states), each lobe presents an internal structure, i.e., it is formed by 4 small dots, which have different contrast at different V and appear much brighter at V= -0.1 V. For biases more negative than -1.0 V, the internal structure is no longer evident, and we observe single lobe features.

- At positive bias (empty states), the behavior is slightly different. At biases $0.1 \leq V \leq 0.5V$ the internal structure is evident but one of the four internal lobes previously identified is much brighter than the others. When moving to higher V, the details of the internal structure are lost, and the lobe appears as a single bright spot again.

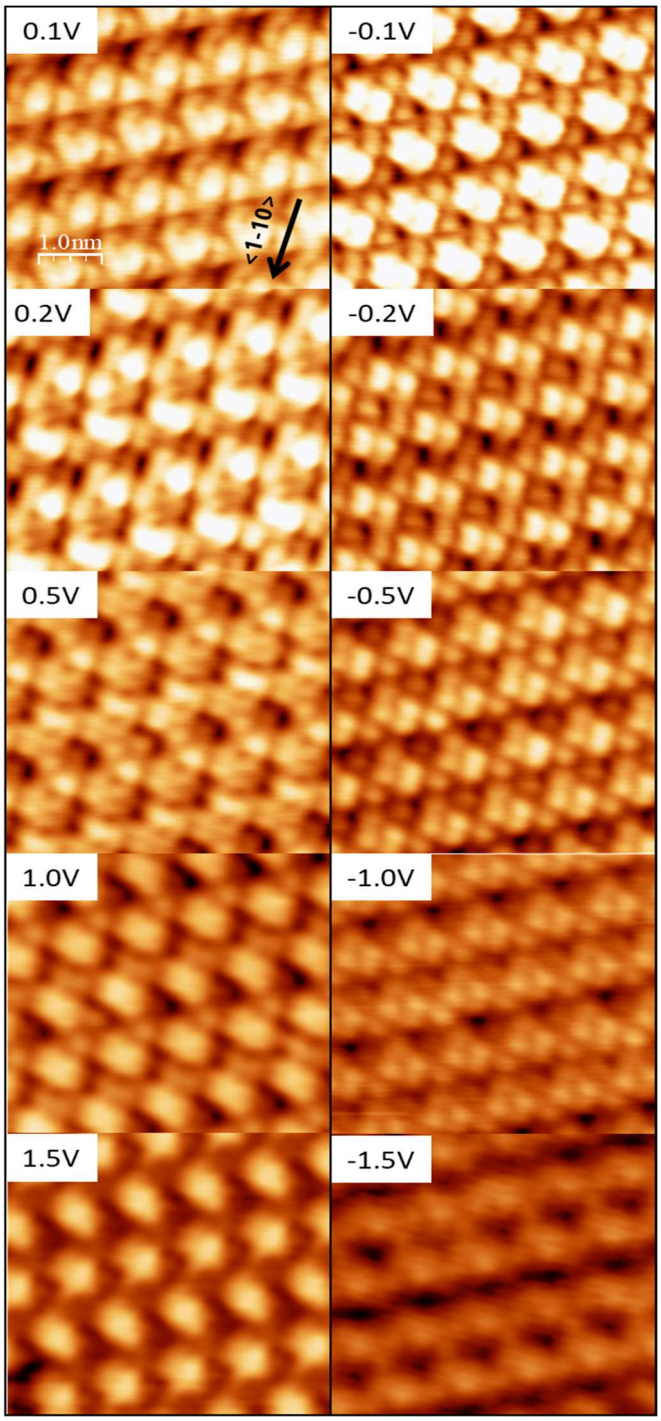

Figure 17 Series of STM images of the CYPD/Ag(110) self-assembled layer produced at RT recorded at different bias voltage in the range from -1.0 V to 1.0V, (5x5nm^2 and i=0.1 nA).

3.2.2. Suggested preliminary models.

Based on the statistical analysis from which I deduced the molecular cell geometry and dimensions, I drew empirical models of the possible self-assembled structures using a home-made routine written in MatLab. The models are based only on geometrical parameters and serve solely as preliminary analysis to ease further theoretical calculations. Therefore, they do not account for crucial parameters (relaxation of the Ag surface, molecular deformation, intermolecular interactions between molecules: Van der Waals forces, hydrogen bonds) which could play a role in the final configuration of the self-assembly. I also underline that, due to the complexity of the system, it is not possible to determine the final molecular geometry without further analysis with complementary tools. In fact, the complete analysis of CyPd includes XPS data and DFT calculations and the resulting final model is much different from those presented in this paragraph. Nonetheless, since they represent the initial stage of my analysis work, I I will briefly explain them as part of the whole story of CyPd on Ag.

To draw the models, I firstly superimposed a molecular scheme of CyPd onto a scheme of the Ag(110) surface (Figure 18). The red rectangle indicates the unit cell of the self-assembled layer of CyPd molecules as determined from STM measurements (Table 2). Converted in units of the Ag (110) primitive unit cell, its dimensions are 2.44x6.95 lattice spacing in the <1-10> and <001> directions, respectively with a rotation of 60 ° off <1-10>. For CyPd, I used the molecular dimensions reported in databases for the undeformed molecule [61], considering that it is lying flat on the surface. The relative position of the molecules with respect to the Ag lattice underneath is arbitrary since the goal is not to determine the adsorption site of the molecule but to unravel the self-assembled geometry.

From the STM images it is impossible to distinguish the brominated molecules from the debrominated ones. I can suppose that the molecules spontaneously de-brominate upon deposition on Ag(110) at RT, due to the high reactivity of bromine and by comparison with similar systems [12]. At the investigated temperatures, Br adatoms are likely to stay on the surface and they can be tentatively identified with some of the small round structures present within and in-between the molecular rows. Ag ad-atoms are also likely to be present on the surface, perhaps forming organometallic complexes. However, the XPS analysis presented in the following was not yet available when I did these empirical models. Therefore, at that moment I concentrated only on the CyPd units, and I did not consider Br or Ag adatoms in the model.

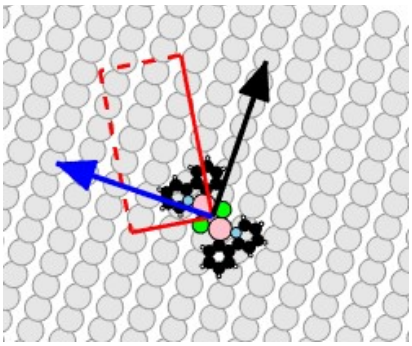

Figure 18 Debrominated CyPd on Ag(110). The black and blue arrows indicate the <1-10> and <001> directions, respectively. The unit cell of the overlayer is marked in red. Its dimensions are those determined by STM analysis. Color code: Ag atoms grey, C atoms are black, H atoms are white, N atoms are light blue, Pd atoms are pink and Cl atoms are green. Br atoms are not reported since they are reasonably already dissociated from the molecule. For simplicity, this drawing of the molecule shows all the C atoms saturated with H, even if it is reasonable that the C-Br bond are broken.

Being an empirical model, there are several possibilities to reproduce the pattern observed in STM images. Figure 19, arrays of molecules with different orientation are superimposed to the experimental, high-resolution STM image. As already mentioned, the dimension of the unit cell suggests that each molecule is imaged with two lobes, which can be either in the same pair of rows (Panel a,b) or in rows of adjacent pairs (Panels c,d). In both cases, two orientations of the molecular axis with respect to the row direction are possible. Therefore, I consider four arrangements, named α, β, γ, and δ in the following, whose geometrical parameters are indicated in Table 3 .

Although these models proved to be inaccurate by the complemented analysis with XPS and DFT, as explained later in this section, they represent a starting point of my analysis and were useful for further discussion within the research group and the theoretical partners.

Table 3 Shows s*ummary of the orientations of the molecular axis wrt the <1-10> direction and wrt the molecular rows for the four possible molecular arrangements observed at RT. Negative angles indicate rotation in the counterclockwise direction.*

Model	Angle wrt <1-10>	Angle wrt row
α	-51	-113
β	0	-62
γ	-62	-124
δ	-8	-70

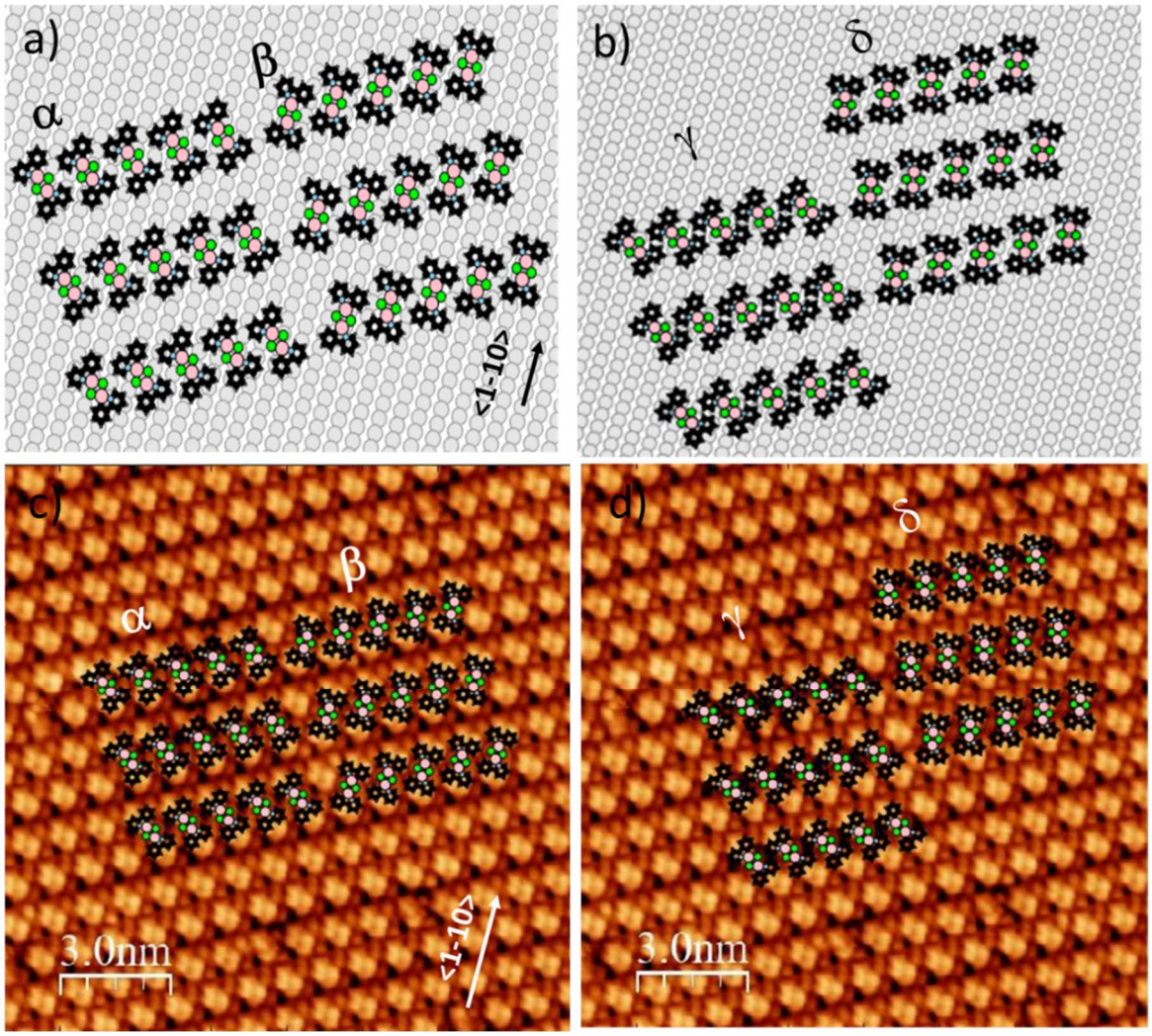

Figure 19ab) Suggested model for molecular arrangements α, β, γ, and δ on Ag (110). Panels cd) the same models superimposed on experimental STM image recorded at V=-0.1 V corresponding to the self-assembled row structures at RT. Models are scaled accordingly.

3.2.3. XPS analysis

As already mentioned, further analysis with complementary tools is necessary for a complete understanding of the system. The chemical information, which is absent in STM images, is provided by the high resolution XPS spectra of Figure 20

Figure 20 shows the Br 3d (panel a) and C 1s (panel b) spectra recorded during an CyPd uptake on Ag(110) at RT. Incremental doses were performed until the saturation coverage was reached, corresponding to the completion of a full monolayer according to STM inspection. The total C 1s and Br 3d areas are reported in panel c.

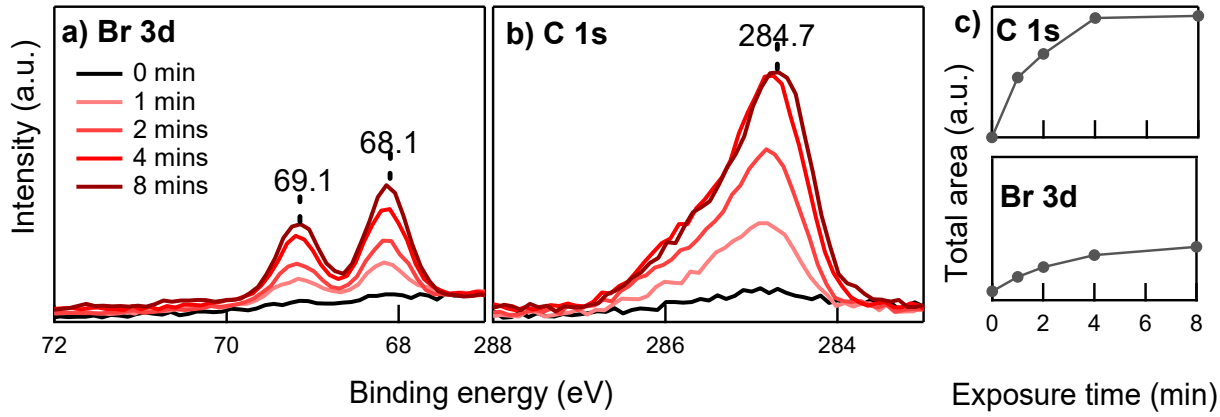

Figure 20 *XPS spectra of a) Br 3d and b) C 1s regions for the Ag(110) surface clean (black trace) and after increasing exposure of CyPd at RT (red traces). c) Total C 1s and Br 3d areas vs exposure time.*

Figure 21 shows the N 1s, C 1s, Cl 2p and Br 3d regions for the full CyPd monolayer of Figure 20 (bottom traces) and their evolution upon annealing to 150 °C (top traces). The outcome of the fitting procedure is also reported to evidence the different components contributing to each spectrum. I first note that only one doublet is present in the Br 3d region at BE (Br $3d_{5/2}$)= 68.1 eV, i.e. at a binding energy corresponding to Br atoms bound to Ag. On the contrary, no traces of Br-C bonds appear around 70 eV [12], [63]. This behavior is already evident at the smallest dose and it is indicative that full debromination of CyPd occurs on Ag(110) already at RT, coherent with what is observed for other halogenated aromatic hydrocarbon species [12], [64], [65]. The Cl 2p spectrum, characterized by a doublet with BE (Cl $2p_{3/2}$)=197.6 eV, is less conclusive since this binding energy is suitable for Cl atoms bound either to Pd or Ag [48], so that it is not possible to determine from XPS spectra if Cl atoms remain bound to the molecule or if they dissociate upon adsorption.

The C 1s spectrum observed at RT has a strongly asymmetric shape already at the smallest coverage. It clearly reveals the presence of multiple components corresponding to C atoms in different chemical environments. The main line at BE=284.7 eV is assigned to the unresolved contributions of sp^2 C atoms (C–C component) and C-H bound carbon atoms [12], [64]. The components at BE=285.3 eV and 286.0 eV are in the range suitable for C-N bonds [66].
The N 1s spectrum shows a single feature, which can be resolved into two components: a main one at 399.4 eV and minor one at 398.6 eV. According to previous literature [67], both species are suitable for pyridinic nitrogen, though their assignment is not straightforward. They could correspond to N atoms with a slightly different interaction with the Ag substrate. A BE value corresponding to the higher energy component was observed for bi-isonicotinic acid on Ag(111) and attributed to nitrogen atoms weakly interacting with the substrate [68]; on the contrary, the lower energy component is compatible with the signal measured in N-doped graphene on Ni(111) [69] and may therefore indicate, in the present case, a stronger interaction with the substrate and possibly N-Ag bond formation.

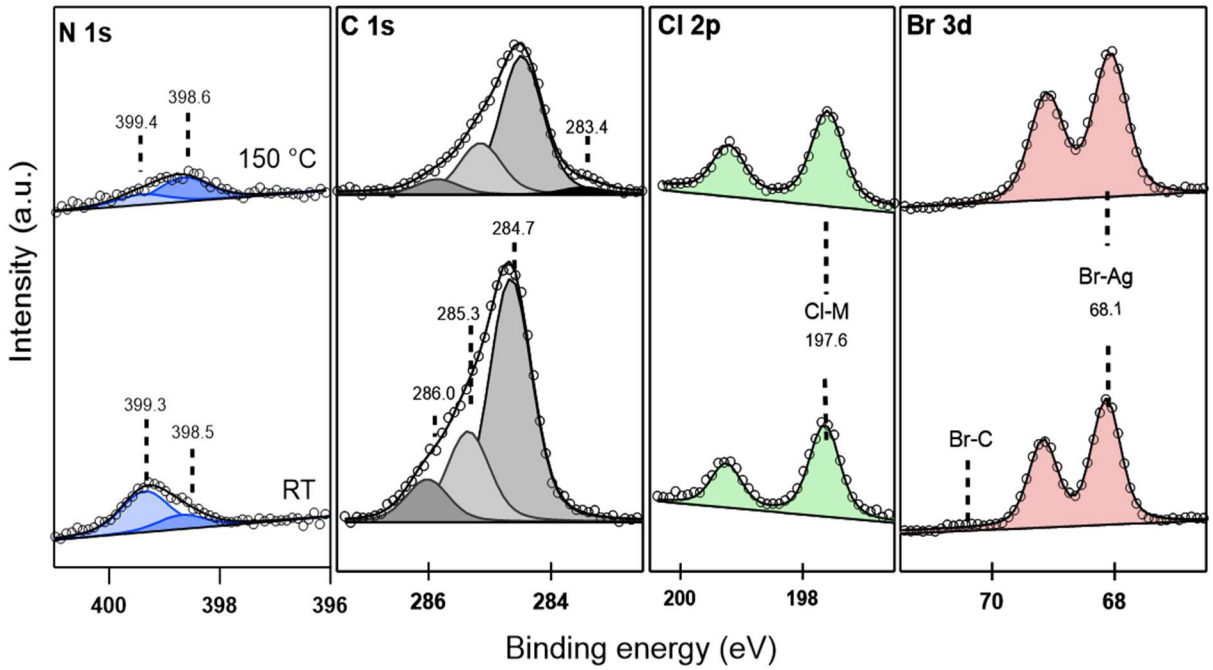

Figure 21: XPS spectra of C 1s, N 1s, Cl 2p and Br 3d regions recorded for CyPd/Ag(110) at RT and saturation coverage and after 5 min step-annealing to 150 °C (upshifted for sake of clarity). The outcome of the fitting procedure and the different components identified are reported in each region.

In this respect, I mention that a very weak upshift of the Ag $3d_{5/2}$ line is observed upon deposition of ~1 monolayer of CyPd (Figure 22). Though it is at the limit of experimental resolution, it is reproduced in different sets of data and therefore it suggests a trend. The small upshift observed may suggest that Ag atoms in a different chemical environment are present on the surface after CyPd deposition. If they are the Ag adatoms directly interacting with the molecule, their coverage of 0.12 ML should contribute to the overall Ag 3d signal for 3 % only in our experimental conditions (hv=515 eV). Therefore, no further analysis is performed since it is not possible to resolve this component reliably. Alternatively, that small shift might be due to a change in the surface core level shift of Ag due to the presence of the overlayer of CyPd molecules, which is also indicative of an interaction of Ag atoms with the adsorbate.

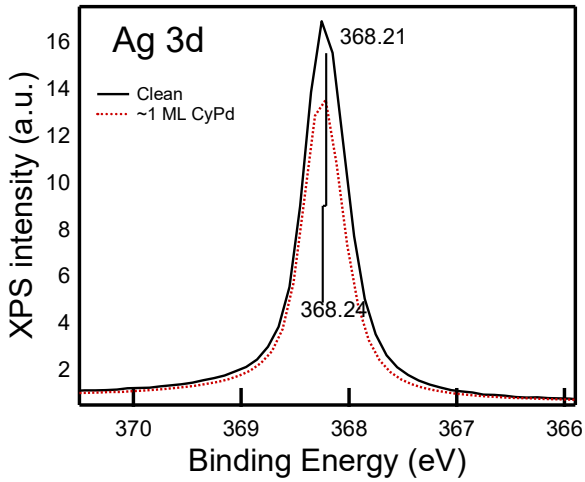

Figure 22 Comparison of the Ag 3d5/2 line of Ag(110) clean and after deposition of nearly 1 ML of CyPd.

Heating up the sample to 150 °C causes desorption of the aromatic part of the molecule, as witnessed by a ~40% decrease of the C 1s and N 1s intensity. In the C 1s region, a small downshift of ~0.1 eV in BE and the appearance of a small additional component at 283.4 eV are observed. This may be due either to some segregation of C induced by the annealing process or by the formation on additional Ag-C bonds. In this case, they should be different from those already formed at RT upon debromination. In the N 1s region, on the contrary, the intensity ratio of the two components gets inverted. Therefore, the amount of N atoms interacting more strongly with Ag increases slightly though the overall coverage decreases with annealing. However, the change in the N 1s spectrum is not reflected in the geometry of the self-assembled overlayer, which remains the same except for minor changes in the internal structure of the lobes. Finally, annealing does not cause significant changes for Cl 2p and Br 3d regions, suggesting that the halogen atoms remain stable on the surface. The last elemental constituent of the CyPd molecule is Pd. Though the presence of such element was checked in the XPS spectra, and though its cross section under the present experimental conditions should allow to see a measurable signal in the Pd 3d region, almost no intensity was observed around 335 eV (Pd $3d_{5/2}$), as shown in Figure 23. This indicates a final configuration in which the Pd atoms are efficiently screened.

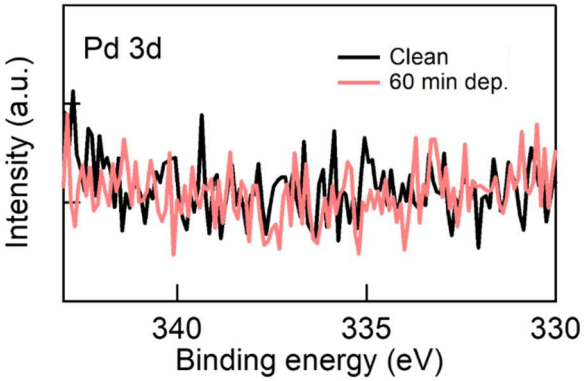

Figure 23 *XPS spectra of the Pd 3d region before and after* CyPd *deposition. No significant intensity is* present at the binding energies expected for the Pd 3d lines (around 335 eV and 340 eV).

The possibility that the molecule dissociates in the crucible during sublimation is ruled out since: i) the stoichiometric ratio of the other elements is respected, as discussed in Table 4 below. ii) the adsorbate organizes on the surface in an ordered, reproducible, and periodic structure. If fragments were produced into the crucible, they would necessarily have different sublimation temperatures and hence their relative abundance on the surface should be far from the molecular stoichiometry, iii) the ATR-FTIR and XPS analysis of the CyPd powders as prepared and after several sublimation cycles in the crucible yielded perfectly compatible results, as already discussed in the preparation section (Figure 13 and Table 1). This indicates that no degradation of the molecule had occurred.
Table 4 shows the stoichiometric ratio between the different elements of the CyPd after sublimation in UHV at RT and subsequent annealing. The obtained values of the self-assembled layers suggest deficiency of C with respect to N. This could be due to the non-planar orientation of the phenyl-pyridine units and, possibly, to photoelectron diffraction effects. The amount of Cl and Br is slightly lower than expected while the Br/Cl ratio is stoichiometric and indicates that dissociation of the molecule occurs upon interaction with the metal surface.

Table 4 Stoichiometric ratio of the CyPd constituents corresponding to the RT deposition of CyPd on Ag(110) at saturation coverage for two different experiments.

	C 1s/N 1S	Cl 2p/N 1s	Br 3d/ N 1s	Pd 3d/ N 1s	Br 3d/ Cl 2p
Exp. A-RT	*7.89*	*0.81*	*0.84*	---	*1.04*
Exp. B-RT	*7.86*	*0.79*	*0.77*	---	*0.97*

3.2.4. DFT calculations

To model the CyPd/Ag(110) system, D. Perilli considered an Ag(110) supercell as the one marked in Figure 24a (purple full cell) because it matches well the experimentally determined repeating unit. The supercell dimensions are sufficient to contain one Pd dimer complex ($C_{22}H_{14}Br_2N_2Pd_2Cl_2$).

The CyPd molecule is considered integer or dissociated in different ways, as shown in Figure 24b. The different optimized configurations were always evaluated for their stability (Table 5) and compared with the experimental STM images. I will briefly describe them, without showing the adsorption geometries and simulated STM images for each one of them, and I will focus on describing the final optimized geometry i.e., the geometry that shows best agreement with the experimental results provided by XPS, NEXAFS, STS and STM.

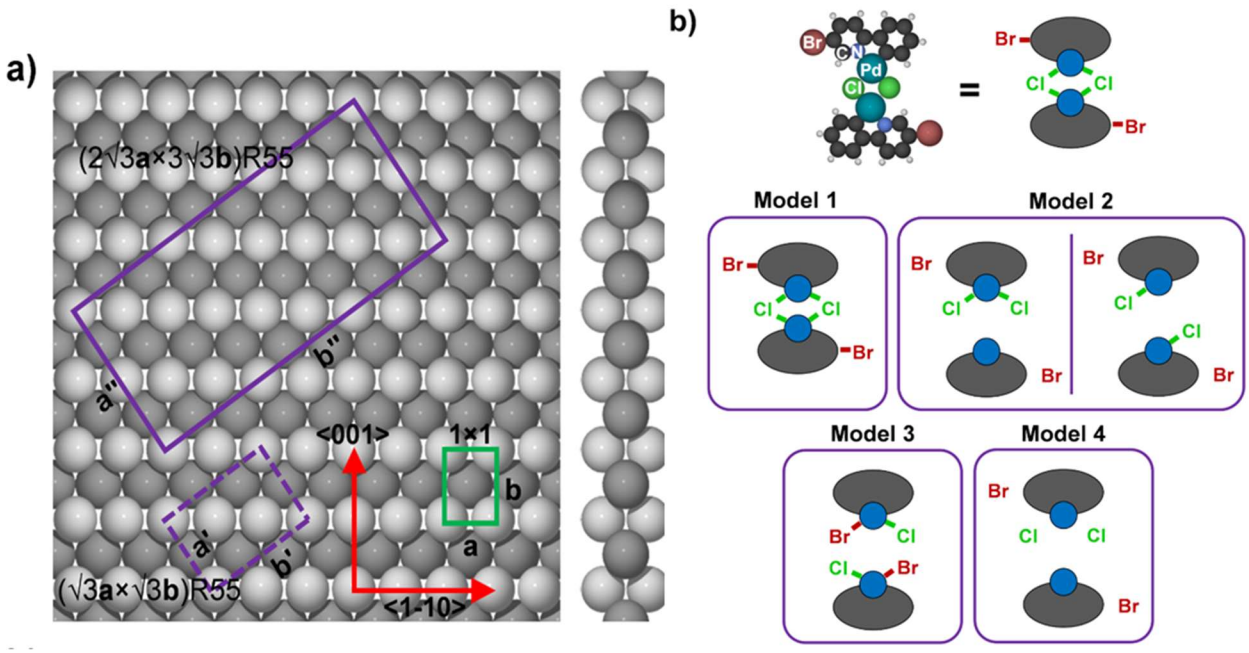

Figure 24*: a) Top and side view of Ag(110). The surface unit cell is shown in green, whereas the smallest unit cell with the same orientation as the experimental one (rotated by ≈60° with respect to the <1-10> direction) is marked in dashed purple. Given the size of CyPd, a (2 × 3) supercell was used (purple full cell). Ag atoms in the top and bottom layer are rendered in light grey; Ag atoms in the middle layer are rendered in dark grey. b) Scheme of possible adsorption/dissociation configurations of CyPd according to the different chemical connectivity.*

Initially, the geometry is optimized for the intact, undissociated molecule (Model 1 in the scheme of Figure 24b). Though this choice is contrary to the information by XPS, which indicates full debromination of the CyPd units already at RT, it is functional to this study. As expected, the calculated adsorption energies in Table 5 (Model 1a) confirm that this situation is not the most advantageous from an energetic point of view. Additionally, the simulated STM images are in poor agreement with the experimental ones, thus in the next step the adsorption of debrominated CyPd on Ag(110) is considered. The geometry of dibrominated CyPd on Ag did not improve the agreement between STM and theory either, hence we considered the possibility that CyPd does not only debrominated upon adsorption on the surface, but that it also breaks in two fragments (Model 2 in Figure 24b). This seems reasonable since dissociation may be favored by the interaction between the Pd atoms and the underlying Ag surface atoms. In this model, two scenarios are possible: the two Cl atoms remain bound to the same Pd atom ($C_{11}H_7NPdCl_2$ + $C_{11}H_7NPd$, Model 2a) or to the different Pd atoms in a symmetric dissociation mode ($C_{11}H_7NPdCl$ + $C_{11}H_7NPdCl$, Model 2b). However, even these two scenarios are not compatible with the experimental STM images.

Next, in model 3, the possibility that Br and Cl atoms are bound to one Pd fragment ($C_{11}H_7NPdClBr$ + $C_{11}H_7NPdClBr$) is considered. In addition, one of the two fragments in the pair is fully rotate to become indistinguishable from the other. The result improved the homogeneous double row patter seen in STM.

Lastly, model 4 is considered, where the halogen atoms split off the molecular fragments ($C_{11}H_7NPd/Cl/Br$ + $C_{11}H_7NPd/Cl/Br$). In this configuration the Pd atoms sit in a 4-fold hollow position, and this causes tilting of the molecule. Since XPS data suggests that the Pd atoms are screened, we checked if they could migrate in the sublayers of the Ag surface. In fact, we determined that the Pd atoms are replaced by one Ag adatom from the surface through a metal exchange mechanism (Model 4-Ag Figure 25). The new configuration is a stable minimum (+100 meV with respect to model 4a, Table 5) and, considering the increase in the overall system disorder, it is certainly entropically more favorable. The atomic charge on the Ag atom attached to the phe-pyr fragment (+0.37 e^-) is about the same as the one calculated for the Pd atom (+0.39 e^-) in the previous model 4a. Therefore, Model 4-Ag is the best fit to the experimental findings. Its validity was verified by the simulated STM image, shown in Figure 25b. The STM image recorded at a bias voltage V=-0.5 V, shows a good agreement with the corresponding one determined experimentally. The same comparison is done for different biases (supplementary material in [36]).

The adsorption energy (ΔE) was calculated in the following 2 ways:

$$\Delta E_{ads,gas} = E_{cypd/Ag} - E_{cypd,\,gas} - E_{Ag} \qquad (1)$$

$$\Delta E_{ads,Model\ 1} = E_{\,cypd/Ag} - E_{cypd,\,model1} \qquad (2)$$

where $E_{cypd/Ag}$ is the total energy of the system with one adsorbed CyPd molecule, $E_{CyPd,\,gas}$ is the total energy of one isolated CyPd molecule in the gas phase, $E_{CyPd,Model\ 1}$ is the total energy of the system with one intact CyPd adsorbed (Model 1), and E_{Ag} is the total energy of the optimized Ag(110) substrate without any adsorbed CyPd molecule.

Table 5 Adsorption energies for AB005 on Ag(110) calculated for all considered configurations. Values for Model 1b are not reported since its number of atoms is different from the other configurations (2 Br atoms were removed from the cell), therefore it is not directly comparable with other models.

	$\Delta E_{ads,gas}$ (eV)	$\Delta E_{ads,Model\ 1}$ (eV)
Model 1a	-2.70	-
Model 1b	-	-
Model 2a	-3.37	-0.66
Model 2b	-2.85	-0.14
Model 3a	-3.57	-0.87
Model 3b	-3.83	-1.13
Model 3c	-4.11	-1.41
Model 3d	-3.98	-1.25
Model 3e	-4.08	-1.37
Model 4a	-3.44	-0.74
Model 4-Ag	-3.34	-0.64

The double row pattern, the unit cell geometry and the position of the molecular fragments (superimposed to the image in Figure **25**b) are well reproduced by the simulation. The four interstitial dots present in each unit cell are assigned to the two Br adatoms in 4-fold hollow sites and to the two Cl adatoms in 3-fold hollow sites, respectively. This behavior is similar to what has been reported for other halogenated aromatic systems on the same substrate [35]. The Pd atoms occupy the octahedral sites below the surface and hence they are not visible in the experimental and theoretical images. The lozenges correspond to phenyl-pyridine units coordinated to one Ag adatom (orange ball). The different brightness within the same lozenge suggests that the pyridinic ring appears darker than the phenyl one. To obtain more information on this geometry I report on the STS spectra and dI/dV maps in *Figure **26***.

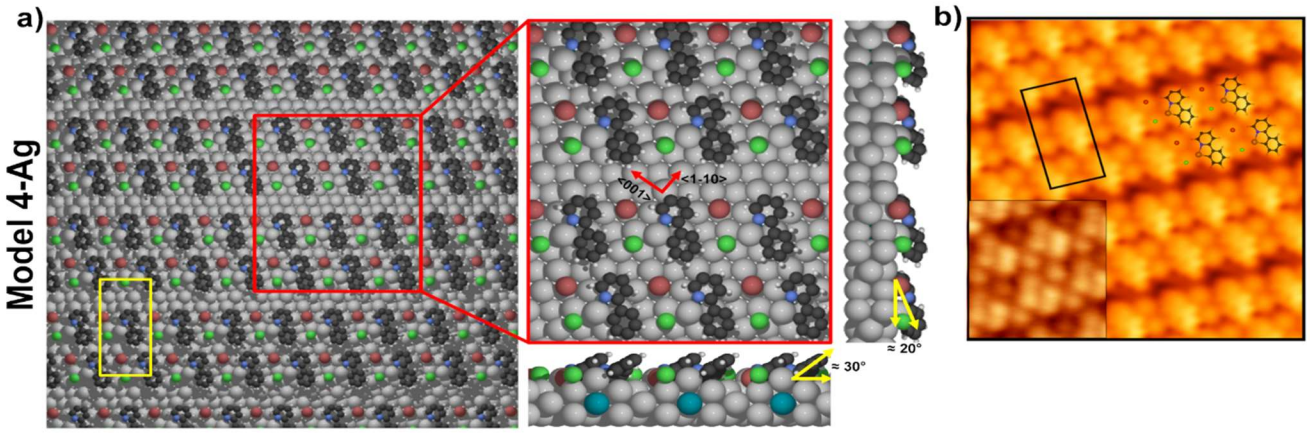

Figure 25a *Top and side view for Model 4-Ag of CyPd/Ag(110). Yellow lines indicate the tilting angle estimate for the fragments with respect to the Ag surface plane. Atoms color code is the same as in* Figure 24*. b) Simulated STM image (V= -0.5 V) with the optimized DFT adsorption configuration overlayed (Model 4-Ag). The corresponding experimental STM image is reported in the bottom-left corner to underline the good matching.*

The STM image of panel a) is well compatible with the double row structure described in Figure 15 and Figure 16, though the internal structure of the lozenges is not evident due to the lower resolution. The STS spectrum of panel d) is measured at the center of a lozenge (red cross in a) and shows the local density of states of CyPd around the Fermi Edge. I mention that STS measurements performed at different points of the unit cell gave spectra equivalent to the one of panel d), which is characterized by a weak state at V~+0.20 V and by a broad and more intense one at V~−0.31 V. The rising tail above +0.5 V is coherent with that observed for other aromatic compounds as benzene [70]. dI/dV maps recorded in correspondence of the observed states (panels b and c) show that the lozenges corresponding to phenyl-pyridine units have a different contrast at the two bias voltages. These differences are reflected in the line scans of panel e), cut along the lines marked on the dI/dV maps: while a lower and broader corrugation is found for V=+0.20 V, the profile measured at V= -0.31 V is sharper and with slightly asymmetric shape induced by the presence of a bright spot in each lozenge. STS and dI/dV maps suggest, therefore, the presence of a localized state around V=-0.31 V, in a position well-suited for the N atom in the pyridinic ring. This assignment agrees with the STS spectra of N-doped graphene with N atoms

in pyridinic configuration [71], while the benzene ring is expected to have an empty state at higher energy (approximately 2.0 V) [70].

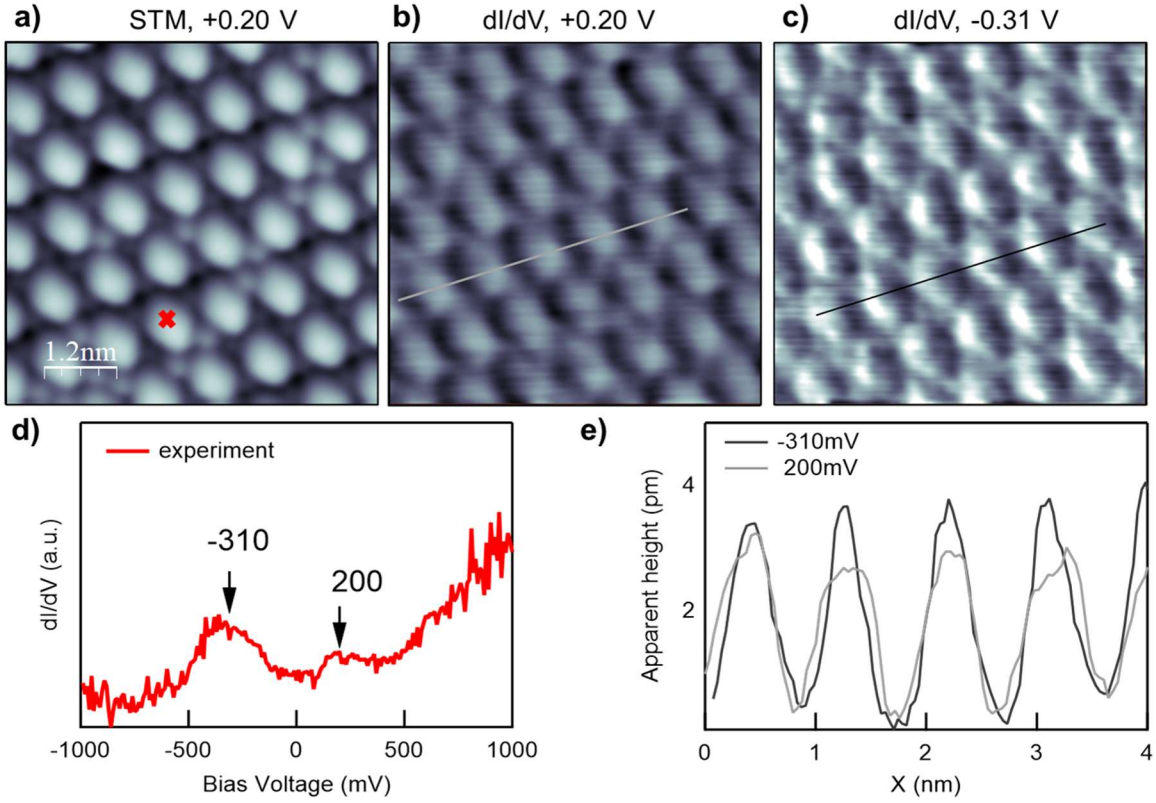

Figure 26 STM image of CyPd upon RT deposition. The red cross marks the point where the STS spectrum of panel d) was recorded. Image size: 6.0 x 6.0 nm², V =+0.2 V, I= 0.42 nA. b) and c) dI/dV maps taken at the bias voltages corresponding to local maxima in the STS spectrum of panel d). e) Line scans cut along the grey and black traces marked in the b) and c).

The NEXAFS spectra of Figure 27 the C and N K-edges recorded after deposition of a full monolayer of CyPd on Ag(110) at RT. Main resonances are present at 284.2 eV, with a shoulder at 284.8 eV and at 288.7 eV in the C K-edge spectrum recorded in p-polarization (continuous lines). Their intensity is reduced by a factor of ~10 in the s-polarization spectra (dashed lines), while broad structures centered around 293 eV and 300 eV appear. The energy region below 290 eV is dominated by π* resonances. We identify the peak at 284.2 eV and the smaller one at 288.7 eV with the $1s \rightarrow \pi_1^*$ and $1s \rightarrow \pi_2^*$ transitions from C 1s occupied core-levels to the lowest unoccupied molecular levels (LUMOs), in agreement with what reported in previous literature for the aromatic systems of phenyl rings [72]. The shoulder at 284.8 eV in the main π^* resonance is likely related to the non-equivalent C atoms bound to N atoms in the pyridine unit [73]. A contribution of C-Ag interaction to the NEXAFS features cannot be excluded. The energy region above 290 eV is characterized by σ* resonances.

The N K-edge spectra show peaks at 398.6 eV and 402.9 eV in p-polarization, while a large resonance around 408 eV is dominant in s-polarization. These features are assigned to the transition of N 1s electrons into the π_1^*, π_3^* and σ^* molecular states, respectively, in good

agreement with what reported for gas-phase pyridine [73] and for pyridine compounds on Au [66], [74].

The strong polarization dependence of NEXAFS spectra implies a preferential orientation of the molecules. However, the residual intensity of π* transitions in the s-polarization spectra indicates that the molecular plane is not flat with respect to the surface. An estimation of the molecular tilt angle can be given by evaluating the s-/p-polarization intensity ratio and following the approach indicated by Stohr for a two-fold symmetry domain [45]. Considering the error introduced by the spectra normalization procedure as well as the azimuthal misalignment of the beam electric field with respect to the <001> direction due to the sample mounting, we found that the spectra describe the molecules as tilted by (20±10) °. This estimate is compatible with the theoretical model (see Figure 25a) which suggests that the molecules in the overlayer are inclined by the angle compatible with NEXAFS.

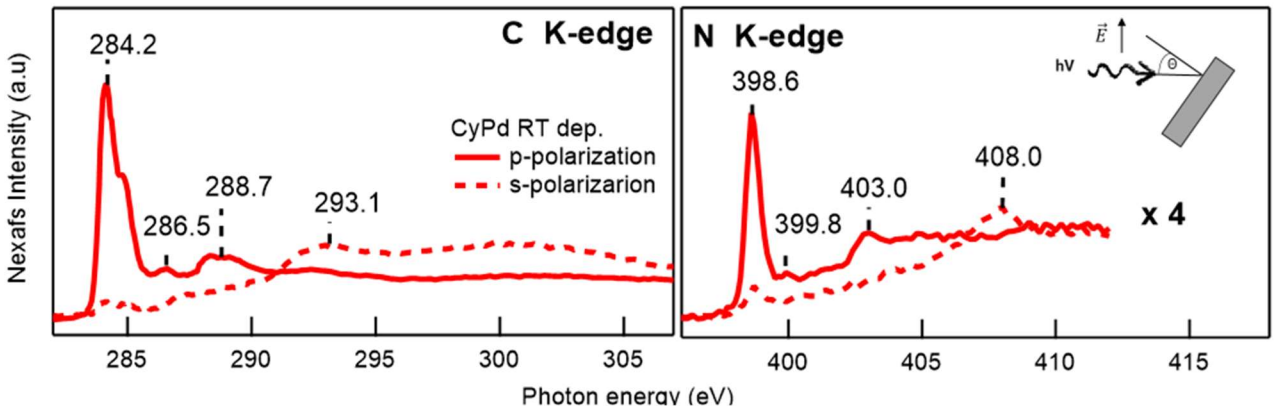

Figure 27 *NEXAFS spectra of the C K-edge and N K-edge recorded with the linearly polarized photon beam impinging normal to the surface (corresponding to s-polarization) and at 85° incidence (corresponding to p-polarization).*

To summarize, upon deposition of CyPd on Ag, the following chemical and conformational steps were developed:

1) Debromination:

$$C_{22}H_{14}Br_2N_2Pd_2Cl_2 \rightarrow C_{22}H_{14}N_2Pd_2Cl_2 + 2Br_{ads}$$

2) Dissociation in two symmetric fragments

$$C_{22}H_{14}N_2Pd_2Cl_2 \rightarrow C_{11}H_7NPdCl + C_{11}H_7NPdCl + 2Br_{ads}$$

3) Dechlorination

$$C_{11}H_7NPdCl + C_{11}H_7NPdCl + 2Br_{ads} \rightarrow C_{11}H_7NPd + C_{11}H_7NPd + 2Br_{ads} + 2Cl_{ads}$$

4) Rotation of fragments and tilting
5) Metal exchange between Pd and Ag

$$C_{11}H_7NPd/Ag_{bulk} \rightarrow C_{11}H_7NAg/Pd_{bulk}$$

The order in which these steps happen on the surface is not definitively determined.

Metal ion exchange between organometallic compounds and the metallic substrate have already been reported for several systems, as Ni porphyrins [75] and Co phthalocyanines [76] on Cu(111). The exchange is favored by annealing of the adsorbed layer but, when the molecules are sublimed at 700 K, their high thermal energy ignites the process already at RT. In the present case this scenario is unlikely because the molecules are sublimed at 130 °C (403 K). Instead, the exchange is likely to be favored by the dissociation of the CyPd complex upon interaction with the Ag surface. Diffusion of the Pd atom below the surface is not surprising, since the surface energy of Pd is significantly higher than that of Ag [77] (2.05 J/m^2 for Pd and 1.25 $J/m/^2$ for Ag), so that Pd atoms tend to migrate into the bulk of the Ag crystal. This is confirmed by previous work on growth of bimetallic AgPd clusters, showing the formation of a core-shell structure with Pd atoms preferentially in subsurface sites [78].
To verify this trend, and since the XPS data suggests that Pd atoms may go deeper into the crystal, the geometry optimization of Model 4-Ag of CyPd/Ag(110) is repeated, with increasing slab thickness from 3 Ag layers up to 5 and 7 Ag layers. The outcome indicates that in the most stable configuration the Pd atoms remain in the middle of the slab (i.e. in the central Ag layer), with a gain in energy of -0.06 and -0.08 eV/Pd for the 5-layer and 7-layer slabs, respectively. The segregation effect of Pd in the subsurface metal layers can be even further facilitated by the high mobility of Ag atoms at the surface, which is not considered in the simulations and would support the experimental information.

3.3.FULL ML COVERAGE CyPd/Ag(110)

The Full-ML CyPd/Ag(110) system is characterized upon deposition of the molecules at RT and subsequent annealing up to 450 °C. As for the sub-ML coverage, the structures are studied with STM, XPS and DFT analysis.
STM images were recorded at liquid nitrogen temperature (LN_2, 77K) using a Pt/Ir tip. They were acquired in constant current mode, with typical tunneling currents 0.2 nA ≤ i ≤ 0.6 nA and bias voltage applied to the sample -3.5 V ≤ V ≤ +3.8 V.

3.3.1. RT deposition and thermal evolution

The STM image in Figure 28 shows an overview of the Ag(110) surface after deposition of CyPd at RT for 30 minutes. It is evident that the adsorbate completely covers the surface; upon careful inspection of several areas of the sample, neither bare Ag patches nor double-layer formation were observed; so, I can safely conclude that the full monolayer coverage has been reached and that the process is self-limiting.
I observe three different self-assembled geometries, labelled A, B and C for convenience. The common feature among them is the presence of stick-shaped units separated by dots and oriented ±30° off the <1-10> direction. In domain A, all the sticks have the same orientation, while in domain B adjacent sticks have opposite orientation and form a sort of zig-zag pattern. Since it is difficult to distinguish A and B domains of the smallest size, for simplicity and to be able to define a unit cell, we assumed a domain to be of A or B type if it contains a minimum of four sticks with the same or with alternating orientation, respectively. In structure C, the same sticks

observed in structures A and B appear as minority structure, being surrounded by shorter features with a brighter end. This arrangement has a short-range and much lower degree of order, and it disappears above RT (see histogram in Figure 30); therefore, it will be discussed only briefly.
I note that these geometries are different from the one obtained upon deposition of CyPd on Ag(110) at RT in the set of experiments discussed in the previous section and in ref. [36]. In that case, however, the molecular flux on the surface was significantly lower since with the same deposition time no full monolayer coverage could be reached. I therefore suggest that the kinetics of the self-assembly process plays a role in determining the final structure observed.

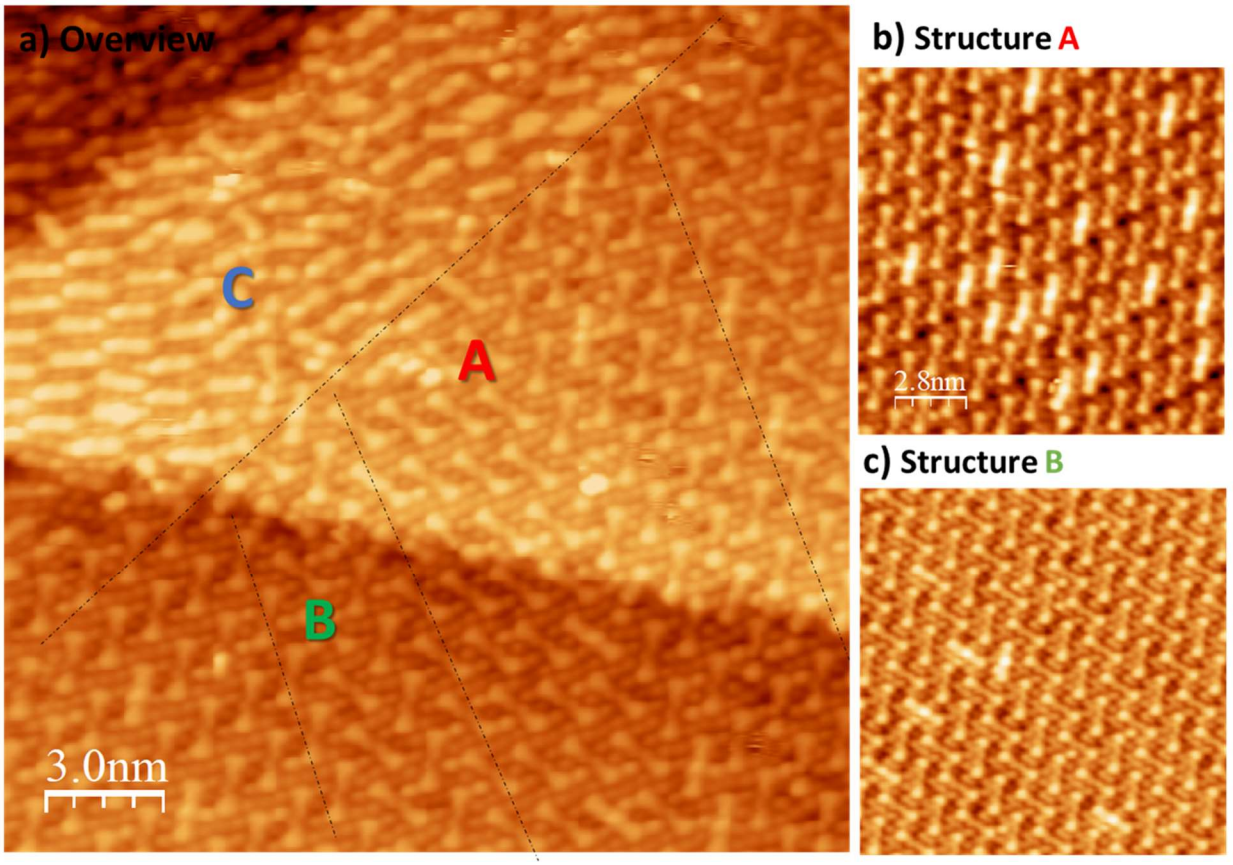

Figure 28a) Overview *STM image of the Ag(110) surface after 30 min deposition of CyPd at RT. Image size: 21x21 nm², V =0.36 V, I= 0.64 nA. A,B and C domains are separated by dashed lines. Panels b,c) show long-range order of the self-assemblies A and B, respectively. (14x14nm², V=0.5V, i=0.2 nA.)*

After deposition, the sample was step annealed up to a maximum T=450 °C to investigate the thermal evolution of the self-assembly. I observe that different molecular arrangements coexist on the surface at the same time. Their morphology is reported in the STM images of Figure 29, together with their relative amount at each temperature, determined from statistical analysis over several overviews, shown in the histogram in Figure 30.
Upon deposition at RT, only geometries A, B and C are present. Annealing to 100 °C causes the disappearance of assembly C, a reduction in the extension of B and an increase of the area covered by assembly A. Such behavior suggests that the most ordered geometry is also the

most stable one. In addition, at this T two new structures appear: the former (I in the following) consists of isolated sticks lying on a c(2x2) reconstructed surface; it becomes dominant at 200 °C and is almost completely removed at 250 °C. The latter (R) consists of bare Ag(110) areas with a (2x1) reconstruction. The area covered by structure R increases from 100 °C to 350°C, at which T it extends almost over the whole surface. Above 450°C, the reconstruction is lifted and clean, unreconstructed Ag(110) terraces is seen in the STM images.

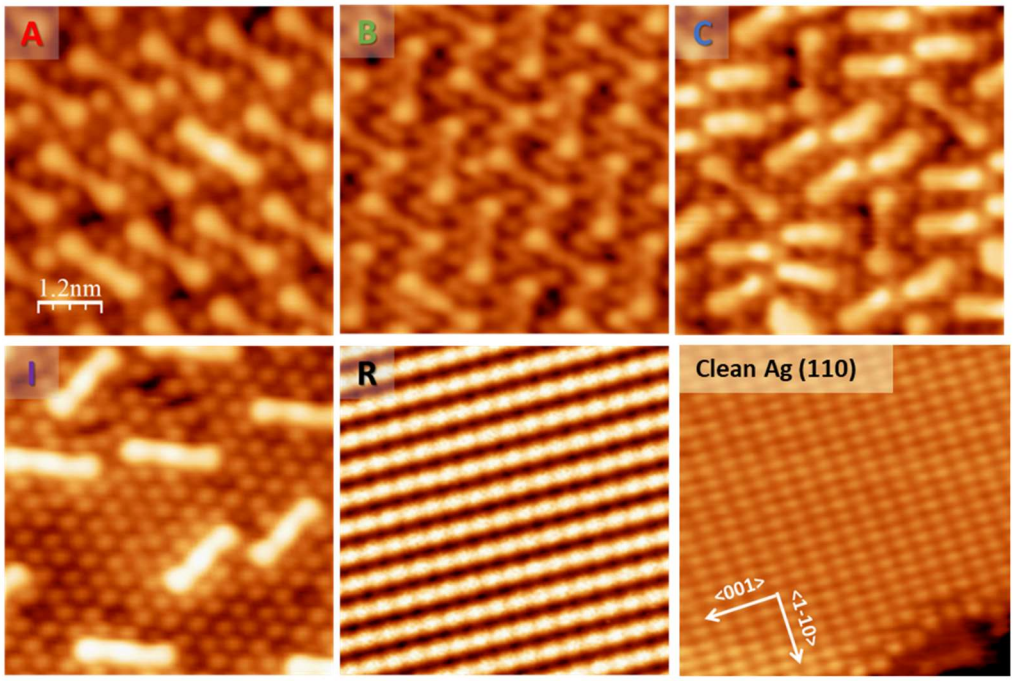

Figure 29 *STM images showing the different polymorphs present on the surface in the investigated T range: A, B and C coexist upon RT deposition while I and R appear only after step annealing. For all Images: size 6 x 6nm², V=0.5 V, i=0.2 nA. Structure R is plotted using a smaller Z-scale for better visualization. Clean Ag surface taken at 450 °C.*

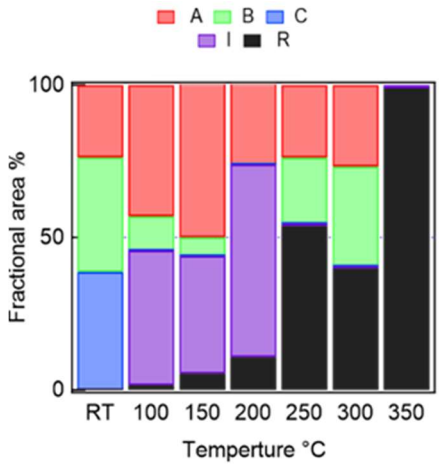

Figure 30 Histogram showing the % fractional area of each structure with respect to the total area covered by CyPd and reconstructed surface.

For a better identification of the observed structures, deposition and thermal evolution of the CyPd/Ag(110) system was investigated in parallel by HR-XPS. Figure 31 reports XPS spectra of the Br 3d, Cl 2p, C 1s and N 1s regions for saturation coverage at RT, i.e. for a full monolayer of CyPd on Ag(110) according to STM data, and upon step annealing to 500 °C.

At RT, doublets are present at 68.1 and 69.1 eV and at 197.6 and 199.2 eV in the Br 3d and Cl 2p regions, respectively. The absence of a Br-C component at BE(Br $3d_{5/2}$)~ 70.4 eV indicates that the molecule is completely de-brominated also at full ML coverage and the Br atoms are bound to Ag. Unfortunately, it is not possible to determine if Cl atoms are still bound to the molecule, since the expected binding energy for Cl-Pd and for Cl-Ag bonds are very close [48].
C 1s and N 1s spectra appear as broad asymmetric peaks with maxima at 284.6 eV and 399.3 eV respectively. In accordance with previous analysis [36], I fit the C 1s line with four peaks at 283.5 eV, 284.6 eV, 285.5 eV and 286.1 eV, respectively. The low BE peak is attributed to C-Ag bonds, which form after molecule dissociation; the one at 284.7 eV is ascribed to the convolution of C atoms involved in C-C and C-H bonds while the other two components are related to C-N with the pyridine ring in different configurations with respect to the substrate [67]. Correspondingly, the N 1s line is fitted with two components at 398.6 eV and 399.3 eV. The Pd 3d region is not reported since, as discussed in the previous section and in ref. [36], Pd diffuses into the bulk and does not contribute to the XPS spectra.

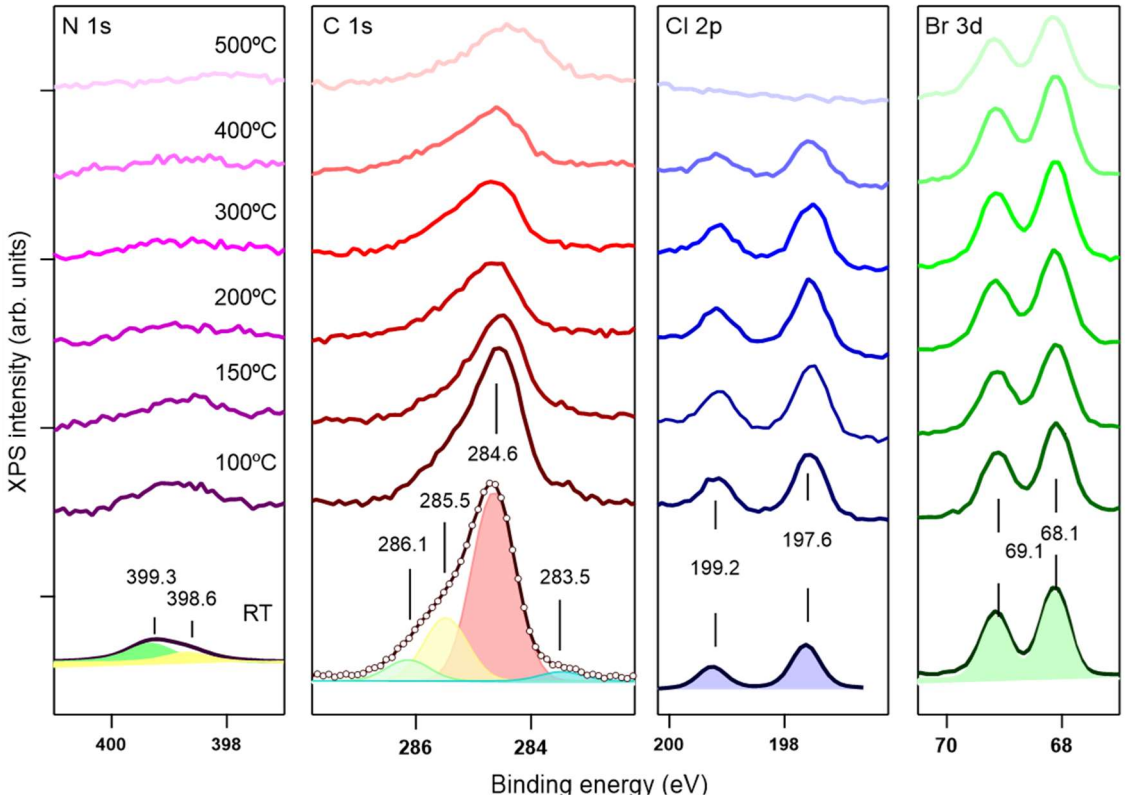

Figure 31 *Photoemission core level spectra of N 1s (purple), C 1s (red), Cl 2p (blue) and Br 3d (green) lines for the CyPd/Ag(110) system obtained upon 24 minutes of deposition at RT and following step-annealing up to 500 °C. Traces are normalized on the background of the corresponding spectrum recorded for clean Ag(110) (not shown) and upshifted for sake of clarity. hv = 515 eV, pass energy = 25 eV.*

Changes in the C 1s and N 1s intensity occur from the first annealing steps, while the Cl and Br signals remain stable till 300 °C and 450 °C (spectrum not shown), respectively, as evident from inspection of the sequence of spectra in Figure 31.

To better visualize the thermal evolution of the layer, I plot the C/Br, N/Br and Cl/Br area ratio in Figure 32. Since I am interested in comparing the behavior of the different elemental constituents of CyPd and not their absolute values, all the traces are further normalized to the value at RT. The graph shows that C and N present the same behavior: their intensity reduces to less than 40% of the original value when annealing from RT to 200 °C, indicating partial desorption of the organic part of the CyPd molecule. Then the peak areas remain almost stable while the peaks broaden and downshift in binding energy. Thus, the residual C 1s and N 1s intensity could corresponds to degradation of the remaining Phe-Pyr units; most probably the phenyl and/or pyridine rings break, and smaller fragments bind to the Ag surface. On the contrary, the Cl and Br intensity is stable to much higher temperatures: Br remains on the surface over the full annealing range, while the Cl intensity drops above 300 °C. Considering the small dimensions of Cl and the higher desorption temperature reported in literature [34], it is reasonable that diffusion into the bulk occurs at least initially. The overall higher thermal stability of halogen species indicates that the interaction with the substrate is stronger for the halogen atoms than for the organic fragments. I note that small C and Br signals are observed by XPS also after annealing to 450 °C, i.e at a temperature for which clean Ag terraces are observed by STM. This discrepancy might be indicative that the residual atoms have migrated into the subsurface region.

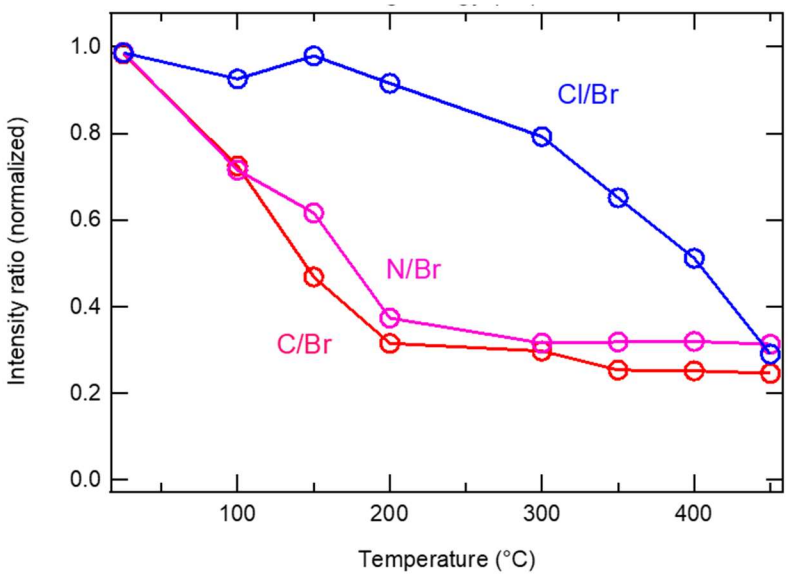

Figure 32 Thermal behavior of the C 1s, N 1s and Cl 2p lines. For a better visualization and to avoid systematic errors, the total C 1s, N 1s and Cl 2p areas are normalized to the corresponding Br 3d signal (assumed as constant) and to the value at RT.

Finally, as mentioned in the previous section and in [36], I highlight that at RT the stoichiometric ratio of Br, Cl and N with respect to C is close to the expected value of 11:1, though actually with a slight deficiency in C. The absence of Pd at the surface, the dissociation of Br and the different thermal stability of halogen atoms and of the Phe-Pyr fragments strongly suggest that the molecule dissociates upon deposition on the surface, as it was already proved to happen at sub-monolayer coverage [36].

3.3.2. Extended assemblies of type A and B

Figure 33 reports close-ups of the overview STM image in Figure 28, showing the geometry of structures A and B in better details. The unit cell parameters are reported in Table 6. Structure A is defined by a black rhomboid with sides: a=(1.26±0.01) nm and b=(2.24±0.04) nm, forming an angle α=(±46±3)° with each other. The unit cell contains one stick oriented nearly parallel to the b vector, and 6 dots of different brightness. Comparing the experimentally determined periodicities with the size of a CyPd molecule (1.34 nm long and 1.05 nm wide), I estimate a population of one molecule per unit cell, corresponding to a local coverage of $(4.9\pm0.1)\cdot10^{13}$ molecules/cm^2. I distinguish between structure A+ and A-, depending on whether the stick is rotated by 30° off <1-10> in clockwise or counterclockwise direction. For structure B, the unit cell is nearly rectangular, with a=(1.56±0.02) nm, b=(2.39±0.06) nm and α=(89±3)°, and with vector b parallel to the <001> direction. The unit cell contains 2 sticks, oriented at +30° and -30° off <1-10>, respectively, and 8 interstitial dots. Therefore, in this case the assembly is slightly more compact, accommodating $(5.3\pm0.1)\cdot10^{13}$ molecules/cm^2. For both structures A and B, the unit cell parameters measured at RT and after annealing are compatible within the error.

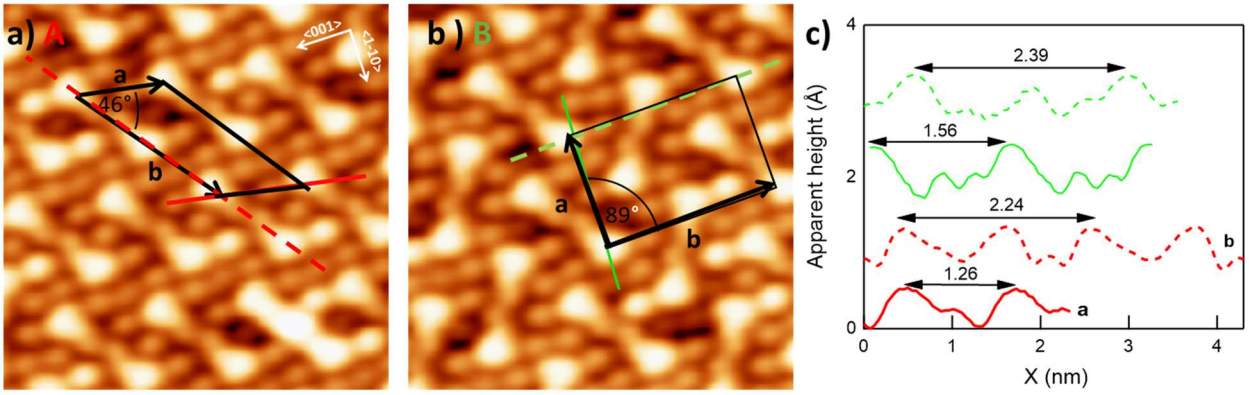

Figure 33 *a) and b): Close-up STM images (5 x 5 nm^2) of the overview in Figure 28, showing the details of structures A and B, respectively. The unit cells are marked in black. c) Height profiles cut along the paths marked in panels a) and b) and corresponding to the unit cell sides.*

Table 6 *showing the unit cell parameters of the different self-assemblies at RT.*

Structures at RT	Orientation wrt <1-10>	Unit Cell parameters
A-	-30°	a=(1.26+0.01)nm b=(2.24+0.04)nm α=(46±3)°
A+	+30°	a=(1.24+0.02)nm b=(2.16+0.03)nm α=(-49±3)°
B	±30°	a=(1.56+0.02)nm b=(2.39+0.06)nm α=(89±3)°

The sequence of STM images in Figure 34 show the evolution of structure A- when step-annealed up to 300 °C. The typical unit cell dimensions are summarized the corresponding Table 7. I notice that the well-ordered islands of sticks/chains obtained at RT remain stable upon step-annealing up to 300 °C. However, the sticks in different rows may be aligned (as in images at RT, 250 °C and 300 °C) or slightly misaligned (see images at 100 °C, 150 °C, 200 °C) with respect to each other, as pointed out by the red dashed lines. This slightly affects the overall shape of the unit cell. The reason for such displacement, most probably, is due to sticks having different registry with the substrate in different rows and hence causing some relaxation of the atomic layers. This suggests that the row direction is the preferential growth direction. I remark that the misalignment does not depend on T but on the area, since domains with different misalignment are observed after annealing at the same T. E.g., I observed large islands (20x20 nm^2) of structure A where misalignments sometimes exist after every second row of sticks and sometimes after every 5th row. (STM image not shown). Based on the line scans taken along the unit cell directions which are reported in the right panel, structure A- is equivalent at the different T since the periodicity in direction a remains the same within the experimental error, while in direction b it is only slightly larger for T=250 °C. The corresponding analysis performed on structure A+ leads to the same conclusion.

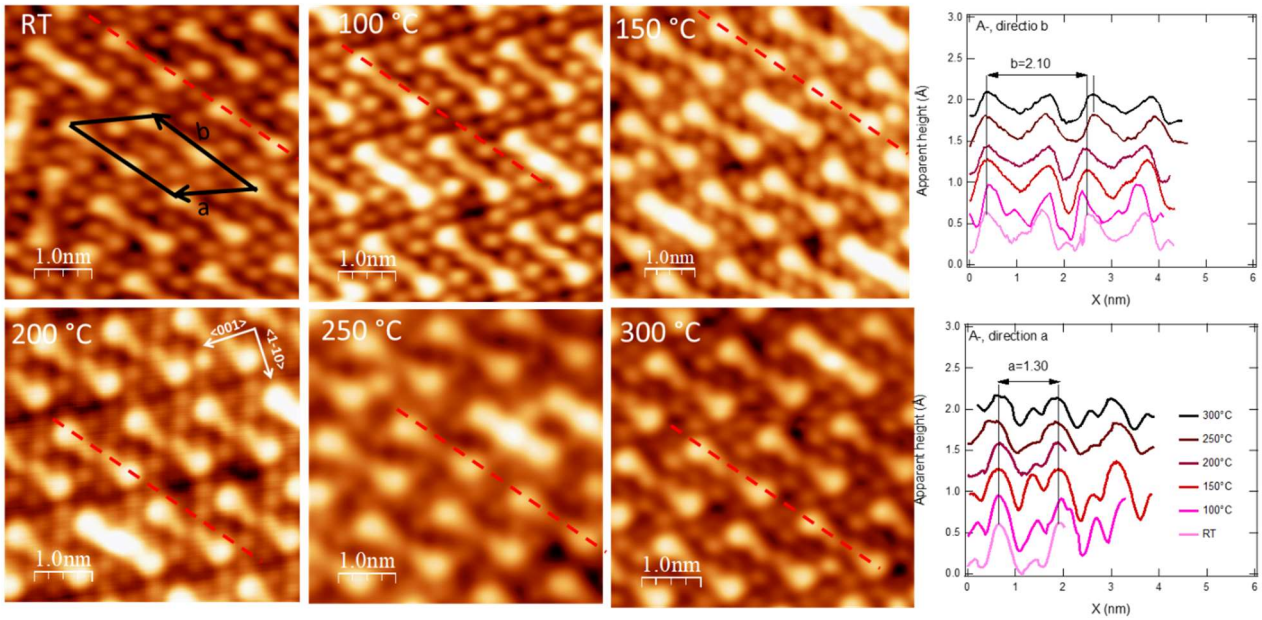

Figure 34 Comparison of the morphology of structure A- at different T. The corresponding height profiles cut along the a and b directions are given in the bottom panels. The red, dashed line evidence the misalignment between adjacent rows of sticks.

Table 7 Unit cell parameters deduced from the line scans of the STM images in Figure 34, corresponding to the evolution of structure A- at different T.

Structure A-	100 °C	150 °C	200 °C	250 °C	300 °C
Unit cell parameters	a=(1.30+0.03)nm b=(2.09+0.03)nm α=(49±3)°	a=(1.29+0.02)nm b=(2.12+0.03)nm α=(47±3)°	a=(1.27+0.05)nm b=(2.07+0.06)nm α=(49±3)°	a=(1.25+0.02)nm b=(2.33+0.03)nm α=(47±3)°	a=(1.26+0.02)nm b=(2.33+0.03)nm α=(47±3)°

The basic constituent of the assemblies, i.e. the sticks, have two different shapes: in the majority of cases they present a minimum at the center, while a few sticks with a central maximum appear in every overview. The high resolution STM image of Figure 35ab and the corresponding line scans of Figure 35c emphasize this difference, also taking advantage of the use of different color contrasts (panel b). Sticks showing a minimum at their center are formed by two "comma-like" features facing each other. Each of them consists of a bright lobe (L) at the end of the stick and of a smaller and fainter lobe (F) pointing towards its center but misaligned with respect to the stick axis. As evident from the line profiles in panel c), this configuration shows a minimum at the center of the stick (green continuous trace). Sticks with a maximum at their center present, on the contrary, a central lobe (L_c) slightly more protruding than the lateral ones (green dashed trace). The overall length is ~1.7 nm for both structures. The relative population of bright sticks in the compact assemblies of type A and B varies from 10% to 20% depending on T, as indicated in the histogram in panel d. Sticks are surrounded by several dots of alternating brightness. Since their density exceeds the number of halogen atoms expected for each molecule, we infer that they correspond both to halogen and Ag atoms and indicate that a significant reorganization of surface atoms occurs upon CyPd adsorption and dissociation.

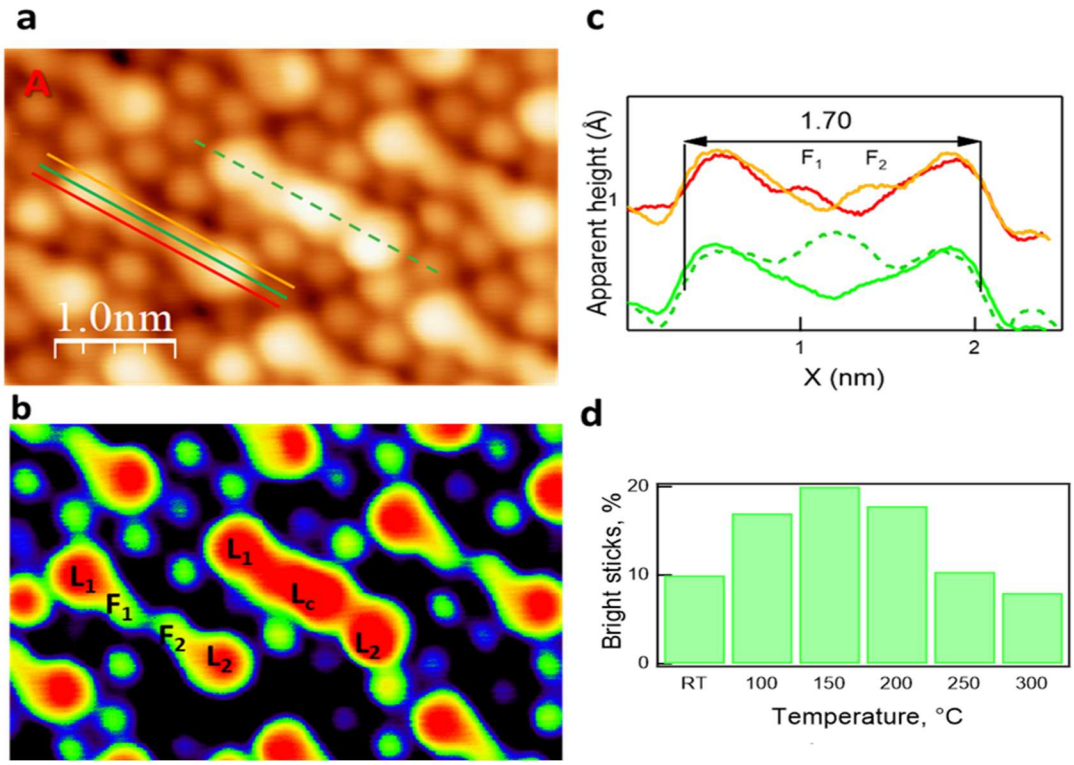

Figure 35 *a) High resolution STM image of structure A recorded after annealing the sample to 150 °C for 5 min (4.5 x 3.1nm², V=-0.1 V, i=0.2 nA). b) Same image of panel a) plotted with a different color palette to better highlight details. C) Height profiles cut along the traces marked in panel a. Panel d) Histogram showing the distribution of bright sticks in domains A and B.*

Structure A- was investigated under the extensive bias dependance range [- 3.5V;+ 3.8V]. A selected set of STM images is shown in Figure 36. The line scans cut across the molecular axis of a bright stick (trace 1) or slightly off the molecular axis of a dark stick (across two sticks with central minimum, trace 2) are shown in the apparent height profiles in the bottom panels. I note that some bias dependence is evident especially at the higher V. When imaging the empty states (+V) with V>1.5 V, the sticks change their appearance into S shaped units. For V > 3.0V, the linear shape is recovered but now they look as formed by three aligned oval lobes. At negative bias -V (filled states) the general appearance of the bright and dark sticks remains the same, indicating a weaker bias dependence. For V< -2.0 V, however the relative intensity between the sticks and surrounding dots changes so that the overall appearance of the overlayer is modified. The height profiles remain qualitatively the same except for changes In the apparent height. Close inspection of the line scans confirms what already observed qualitatively from the images. In particular, for the sticks with bright center (trace 1):

- Up to +2.0 V the apparent height of central maximum is higher than that of the two side shoulders. Above V>+3.0 V this is not true anymore and all three maxima have equal apparent height.

- Much less dependence is present at negative bias. Again, three maxima are evident and well separated at any V, though the average apparent height of the nanostructure decreases for more negative values.

Vice versa, for the sticks with central minimum (trace 2):

- At low bias (0.1V and 0.8 V), the profiles present two maxima and a very low side shoulder between them.
- Above 0.8V and to up to +2.7 V the side shoulder increases in intensity and becomes as bright as the two maxima. This corresponds to the change in the molecule appearance, from stick to S-shaped. For V=+3.0 V the local shoulder reduces again in intensity
- At negative bias, the dependence is much less evident and consists in the reduction of the side shoulder and of the overall apparent height with increasing negative bias.

Additionally, the same bias dependence trend was observed for structures A+ and B.

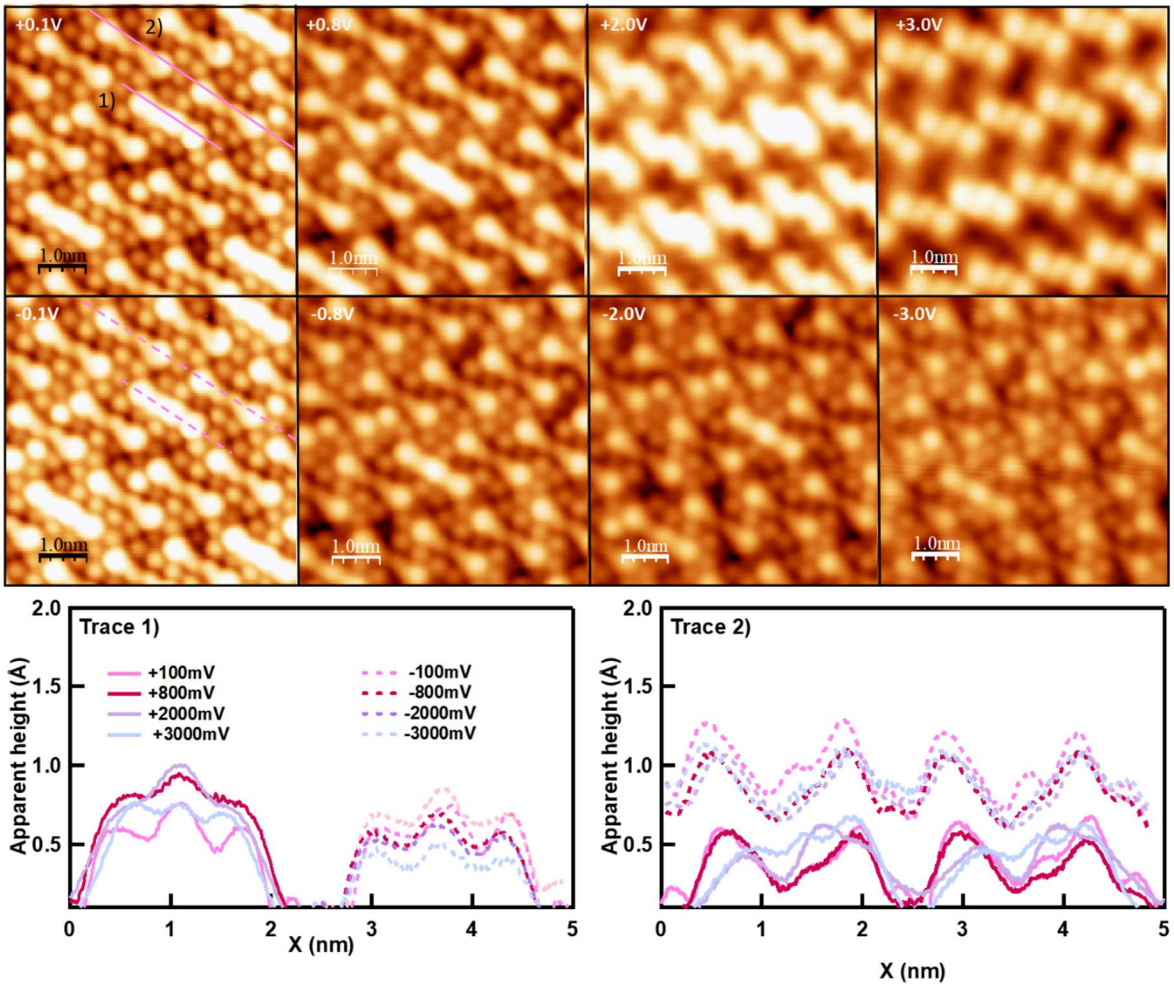

Figure 36 STM images of structure A- recorded at different bias voltages. The islands were prepared by annealing the full monolayer CyPd/Ag(110) to 150°C . The line scans drawn across one bright stick are reported in left bottom panel (trace 1 corresponding to +V (left) and -V (right). The line scans across two sticks with central minimum (trace 2) are reported in the bottom right panel. Here, the +V and -V are upshifted for the sake of clarity.

Finally, Figure 37 shows STM images and the corresponding height profiles of Structure C. The overview STM image reveals that this layer is not periodic, therefore it is not possible to define a unit cell. However, I note the presence of a characteristic local arrangement marked by the rhomboids in panel a). They present two different orientations (continuous and dashed rhomboids in panel a), which are translated mirror images of each other with respect to high symmetry directions. The dimensions a=(1.30+0.02)nm and b=(4.10+0.03)nm are determined from the height profiles reported in panel c). Each rhomboid consists of four elongated features (stripes) in a nearly rectangular pattern, sided by two parallel sticks like those described for structures A and B. I note that the stripes are not uniform: each of them has a fainter end, pointing at the nearby stick, while the brighter ends point at each other. These features are better analyzed and compared in the enlarged STM image of panel b) and in the corresponding line scans of panel c). The stripes (orange line) are approximately 1.1 nm long. The change in contrast along the stripe is reflected in the asymmetry of the profile. I note that those features appear 0.3 Å higher than the sticks (green trace). The sticks show the same length measured for structure A and B. Furthermore, the interstitial dots of alternating brightness marked by the red line scan show periodic arrangements of 0.4 nm (center-to-center). Diamond-like features, marked by the pink circle in panel a), are occasionally seen and present a more compact profile with 0.80 nm FWHM for the long axis (pink trace, panel c).

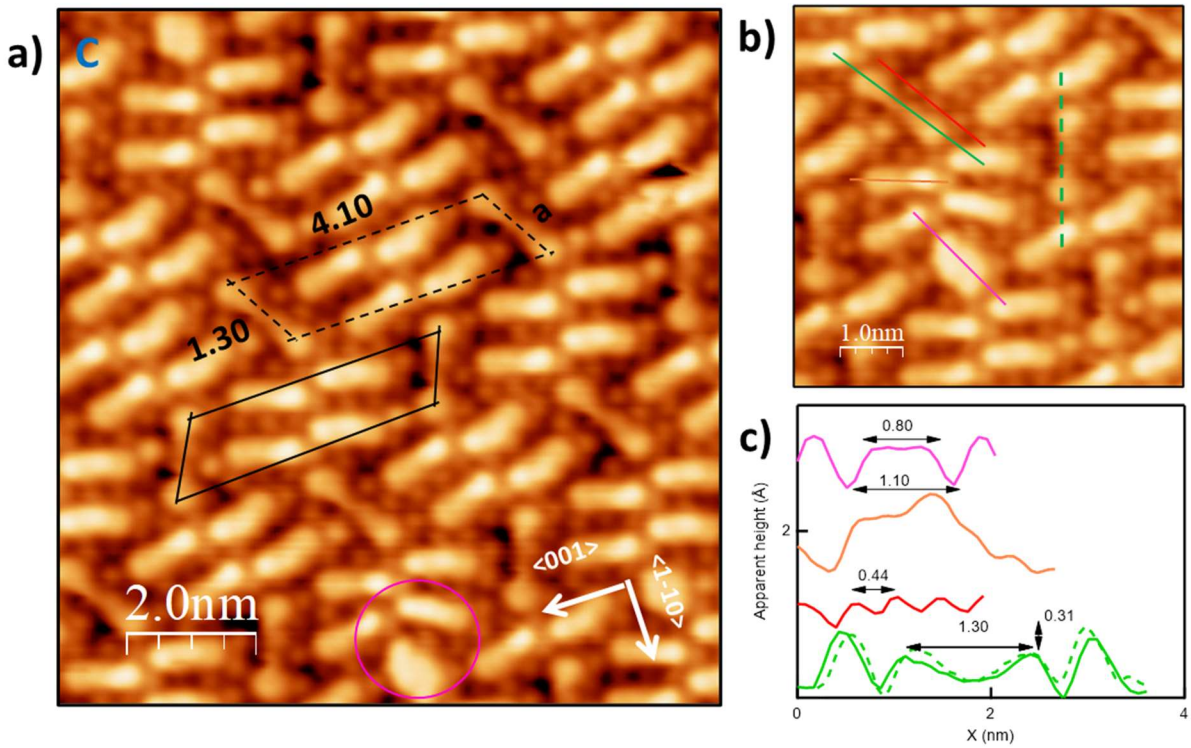

Figure 37 ab) Overview STM of structure C showing the unit cell of the local arrangement. Panel b) shows enlarged STM image for more details with the corresponding apparent height profile in panel c).

3.3.3. Isolated structure and surface reconstruction

According to XPS inspection, after annealing the sample to 100 °C, desorption of the Phe-Pyr units occurs. Coherently, sample areas with little or no molecule-related features appear in STM images. Figure 38 shows an STM overview of the Ag(110) surface after annealing to 200 °C. Most of the surface is covered with structure I, which consists of isolated sticks oriented ± 60° off the <1-10> direction. They sit on top of Ag terraces presenting a slightly compressed hexagonal pattern (see panel b) which, for fcc crystals, corresponds to a c(2x2) reconstruction of the (110) face. In addition, a few areas with a rectangular pattern typical of a p(2x1) reconstruction of the substrate (indicated by R – see unit cell dimensions and orientation marked in panel c) are visible in the overview. Such patches grow with T and cover most of the surface at 350 °C. I remark that no molecular features are found on the R structure, indicating that it becomes energetically favored only after complete local desorption of the organic fragments.

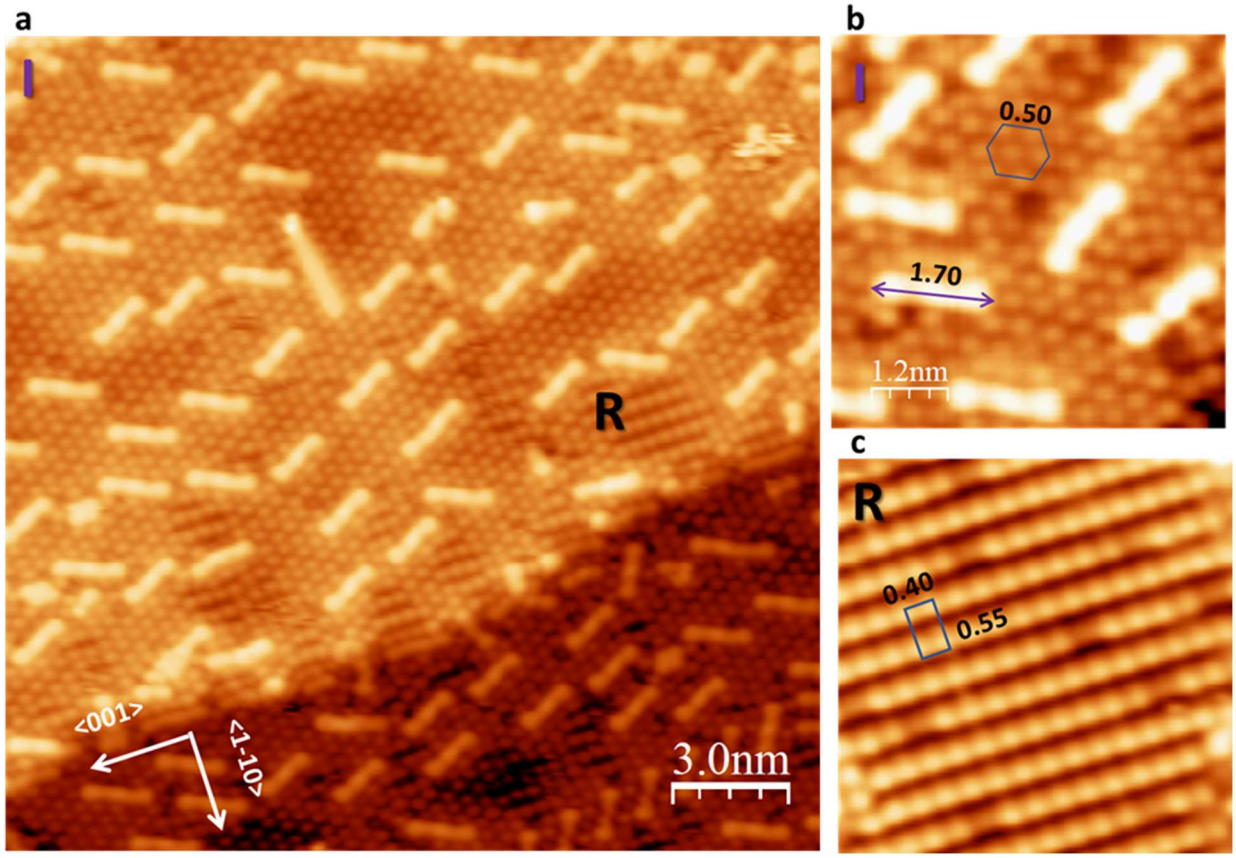

Figure 38 *a): Overview STM image of the Ag(110) surface covered with structure I. Domains with reconstructed p(2x1) surface are also present and labelled as R. The image was recorded after step-annealing the sample to 200 °C for 5 minutes (20x20 nm², V= 0.5 V, i=0.2 nA). b) and c):* Close-ups of I and R structures (6 x 6nm², V=-0.5 V). The unit cell of the reconstructed surface is reported on both panels; dimensions are expressed in nm.

No significant bias dependence is observed for structure I, as evidenced by the STM images and corresponding line profiles in Figure 39. However, differences in the brightness of the sticks can still be noticed and this is reflected in the different apparent height measured in the line scans

reported in panel b. All the sticks in structure I present a central bright lobe and are ~1.7 nm long, thus, they highly resemble those already discussed for assemblies A and B. The different orientation (±60 ° off <1-10> instead of ±30 ° for the compact structures) could be related to the low density and/or to the symmetry of the reconstructed Ag terrace.

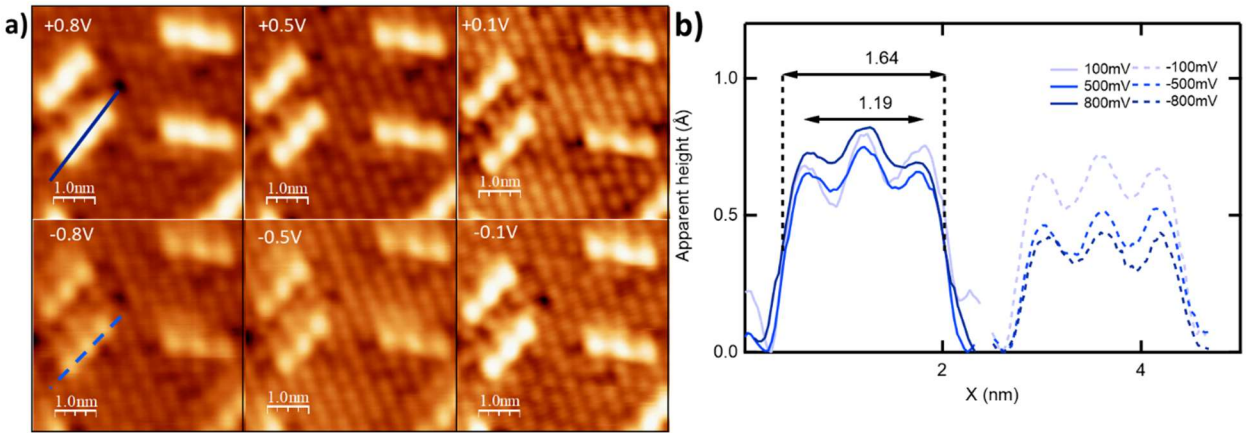

Figure 39 Bias dependence of structure I. The STM images were taken after annealing the sample to 200 °C. The line scan drawn across one bright stick are reported in panel b). + V are indicated with solid traces (left side in the apparent height profile), while dashed lines correspond to -V (right side in the apparent height profile).

To determine the atomic structure and conformation of these bright sticks, a DFT study is performed starting from a model consistent with the experimental evidence. As stated above, XPS data suggests dissociative adsorption of CyPd on the Ag surface followed by Pd atoms diffusion into the surface, while Cl and Br atoms disappear only for T > 300 °C and T> 450 °C, respectively. Based on this information, each stick can be formed by two Phe-Pyr units anchored to the Ag surface. The halogen atoms are not considered in the model, because they are expected to bind to a surface Ag atom right after dissociation from the organic fragments, and act then as spectators. Similarly, Pd atoms are not accounted for because they have diffused beneath the Ag surface.

The proposed adsorption models for dissociated CyPd on the Ag(110)-c(2x2) surface are reported in Figure 40. Initially, two Phe-Pyr units in a *trans* configuration (i.e. with N atoms (blue color) of the Pyridine rings on opposite sides of the two units) are considered. The *trans* configuration is expected to form after dissociation of a CyPd molecule at RT and diffusion of the fragments on the surface. In panel a) in the *trans* $(Phe\text{-}Pyr)_2Ag$ configuration, the two Phe-Pyr units are almost aligned to each other, and they are linked through one Ag adatom (1), thus forming two bridging organometallic C-Ag-C bonds. Each Phe-Pyr unit is also connected to another Ag adatom (2) by C-Ag and N-Ag bonds. This configuration is stabilized through the passivation of the dangling bonds (produced by dissociation of the Pd and halogen atoms from the original molecule) by the Ag substrate, and the new C-Ag and N-Ag bonds direct the molecule orientation.

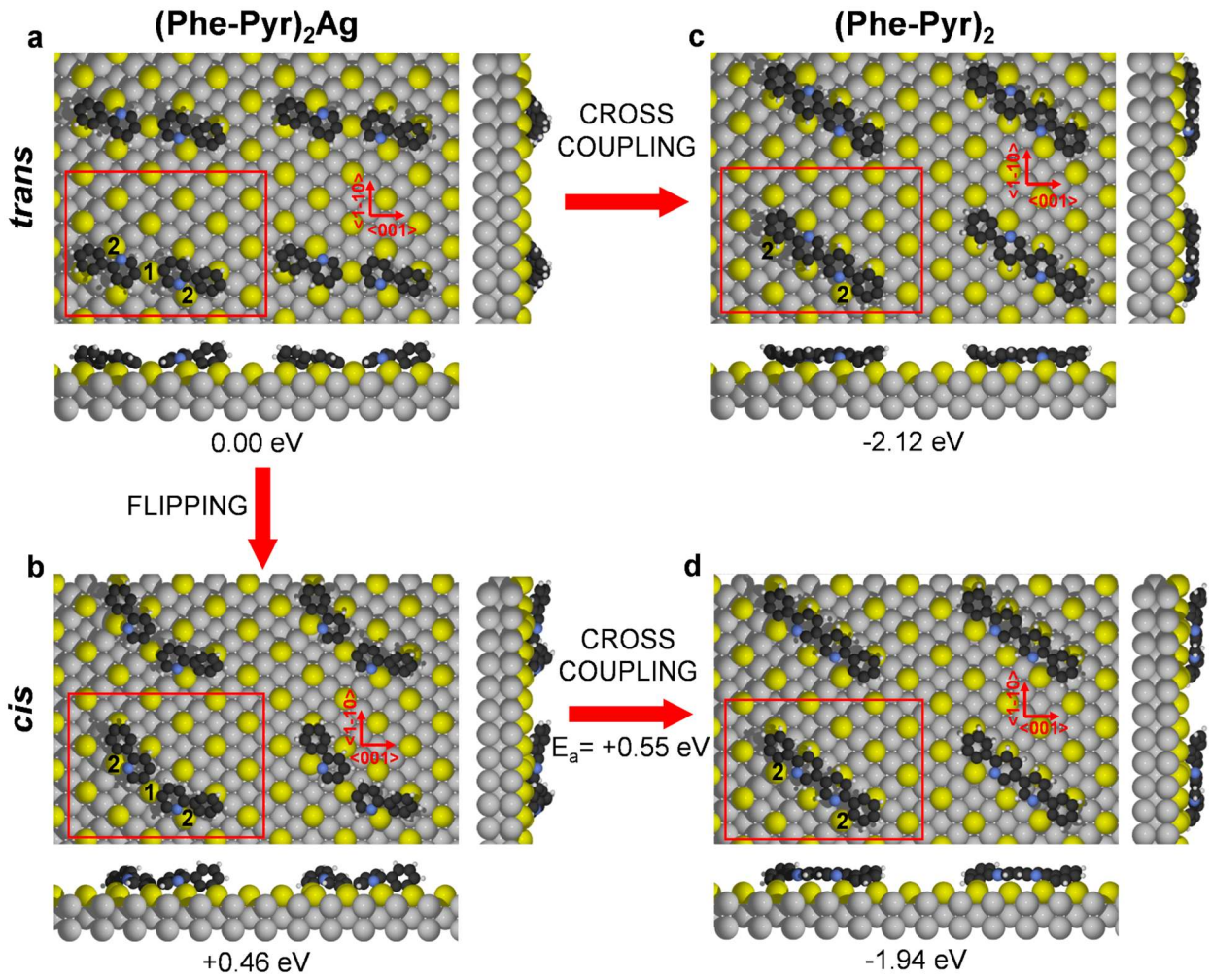

Figure 40 *Top and side views for adsorption models of CyPd on Ag(110)-c(2×2). The two main crystallographic directions (<001> and <1-10>) are indicated by the red arrows. The (6 × 3√2) supercell is shown in red. Relative energies (with respect to configuration a) are reported below each panel (in eV). Color coding: Ag atoms belonging to Ag(110) surface are in gray, Ag adatoms due to the c(2×2) reconstruction are in yellow, C atoms are in black, N atoms are in blue, and H atoms are in white. Ag adatoms involved in interaction with the molecular fragments are labeled as (1) and (2), as described in the text.*

The side view of the adsorption geometry (Phe-Pyr)$_2$Ag in model Figure 40a does not display any atomic protrusion at the expected location for the Ag adatom. Correspondingly, the simulated STM image (Figure 41a) is characterized by two faint lobes pointing at each other and two brighter ones facing the outside. The model is thus consistent with the experimentally observed dark sticks (DS) observed in structures A and B (Panel e).

To explain why sticks in structure I (and in smaller numbers also in structures A and B) have a bright central protrusion, the possibility that a C-C coupling reaction occurs is considered. The C-C coupling reaction occurs from conversion of (Phe-Pyr)$_2$Ag into the dimer 6,6′-diphenyl-3,3′-bipyridine (Phe-Pyr)$_2$. Direct conversion from *trans* (Phe-Pyr)$_2$Ag (panel a) to *trans* (Phe-Pyr)$_2$

(panel c), although largely exothermic (-2.12 eV), is likely to be kinetically hindered. In fact, the formation of the new C-C bond requires that one of the two Phe-Pyr fragments moves around the Ag adatom (1) and gets close enough to the other Phe-Pyr units to allow for C-C coupling; these adjustments could be energetically demanding since they require the breakage of a C-Ag bond between the organic fragment and Ag adatom (2) from the same row (panel a), and the formation of a new C-Ag adatom bond with the Ag adatom in another row (1) (panel c). An alternative and easier path is shown in panels bd: one Phe-Pyr unit of *trans* $(Phe\text{-}Pyr)_2Ag$ flips on the surface around the Ag adatom (2), without the need to detach from both Ag adatom (1) and (2) and converts into the *cis* $(Phe\text{-}Pyrs)_2Ag$ conformer (Figure 40b). Starting from this new conformer, the C-C coupling can lead directly to the final *cis* $(Phe\text{-}Pyr)_2$ product (in Figure **40**d). In this case, no detachment of the Phe-Pyr unit from the surface is needed because the two C atoms are now on the same side of the Ag(2)-Ag(1)-Ag(2) row. The activation barrier for this last step is computed to be 0.55 eV. Note that the simulated STM image of *cis* $(Phe\text{-}Pyr)_2$ (in Figure 41d) is in better agreement with the experimental STM images of the bright sticks (BS) in structure I, than the corresponding simulated STM image of *trans* $(Phe\text{-}Pyr)_2$ (Figure 41c). Simulated STM images for all models reported at different bias voltages (+/- 0.1 V and +/- 0.5 V) have been calculated and confirm the good agreement (supplementary materials in ref. [37]) between DFT and the STM experiments.

Although the simulations were performed for an isolated CyPd unit, it is highly likely that they explain also the self-assembled geometries A and B. Therefore, the sticks with a central minimum can be identified with coupled Phe-Pyr fragments saturated towards a central Ag atom ($(Phe\text{-}Pyr)_2Ag$), while the ones with central maximum are correlated with the $(Phe\text{-}Pyr)_2$ units. The different orientation of sticks in structures A and B and in structure I is most likely related to the additional interaction with neighboring molecules in the self-assembled domains. Therefore, our combined experimental and theoretical analysis suggests that surface assisted synthesis of the $(Phe\text{-}Pyr)_2$ compound occurs on Ag(110) by cross-coupling reaction of the two identical organic fragments generated by dissociation of a single organometallic CyPd unit. This is different with respect to most cross-coupling reactions since in this case only one molecular precursor is needed.

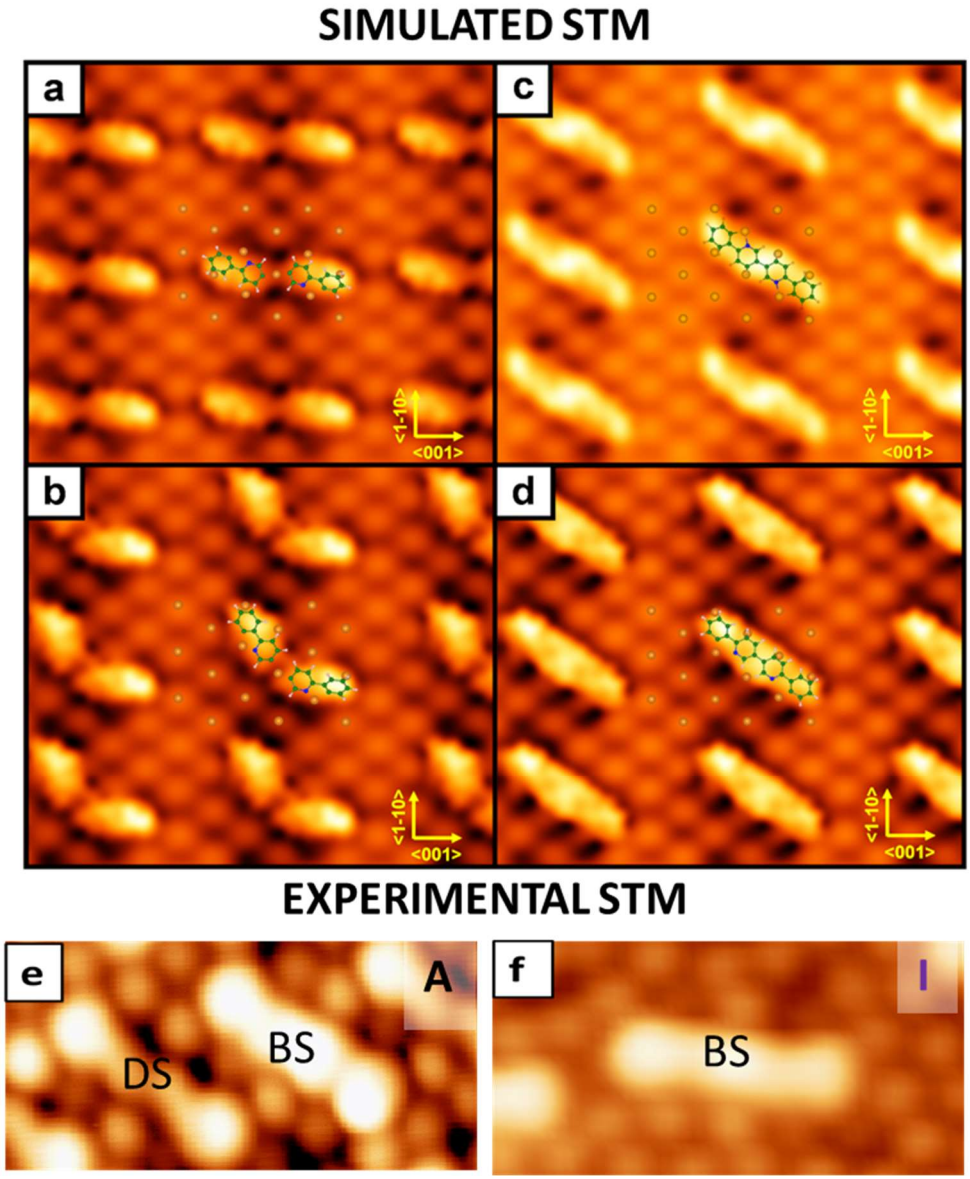

Figure 41 S*imulated STM images a, b, c, and d corresponding to the the models reported in* Figure 40*, respectively. Yellow lines indicate the two main crystallographic directions: <001>, and <1-10>. Atoms of the CyPd molecule (C in green, N in blue, and H in white) and the Ag adatoms (in orange) contained in the (6 × 3√2) supercell are superimposed on the image to facilitate its understanding. V = −0.1 V, LDOS iso-surface value of 5 × 10^{-5} /e|/a$_0^3$.* e is the electron charge and a_0 is the Bohr radius. Panels e and f show experimental STM images of structures A and I, for comparison with the simulated STM.

Furthermore, the density of bright sticks increases after the first annealing steps (Histogram in Figure 42), while the overall molecular coverage at the surface decreases significantly. This perfectly agrees with the DFT information that the conversion from configuration a) to d) requires to overcome a small energy barrier. Therefore, the formation of structure d happens concurrently with the desorption of the molecules, which happens at relatively low T (100 °C) as established previously.

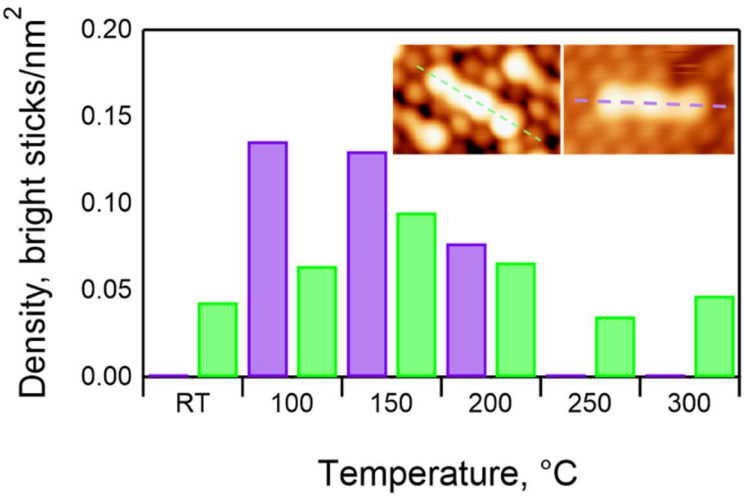

Figure 42 Histogram showing the density distribution of bright sticks per unit of surface area vs annealing temperature. Green columns refer to bright sticks found in the self-assembled structures A and B, and purple ones to Structure I. Statistics are based on at least three overviews of structures A/B, I at each temperature. The density of bright sticks is significantly larger for the I structure, especially at 100 °C and 150 °C, indicating that a conversion from $(Phe\text{-}Pyr)_2Ag$ *to* $(Phe\text{-}Pyr)_2$ occurs upon annealing.

Finally, the role of halogens and the presence of a surface reconstruction is addressed. As mentioned before, Cl and Br remain stable at the surface up to temperatures much higher than the Phe-Pyr units. This is also in accord with other experiments on similar system [12], [33], [64]. The reason for such stability is explained by [12], [32], [33] for di-bromo-pyrene, di-bromo-benzene and di-bromo-tetracene on Ag or Cu surfaces. In those works, the authors report that an efficient desorption mechanism for halogen atoms chemisorbed on metals is to react with H and leave the surface in the form of hydrogen halide. Hydrogen atoms are provided by further, thermal induced dehydrogenation of the precursor molecule, or even by controlled exposure of the sample to a flux of atomic H [33]. The situation is different in the present case, since no additional C-H bonds are broken upon annealing; instead, Phe-Pyr units are likely to desorb intact or to cross-couple to form $(Phe\text{-}Pyr)_2$. It seems plausible that the unavailability of H is the reason for the higher thermal stability of halogens with respect to other literature data, since they will desorb as diatomic molecules or metal halides [27], [31], [34] or, in case of Cl, may diffuse into the substrate [34].

Isolated sticks sit on a c(2x2) reconstructed surface, while a p(2x1) pattern appears in areas where all the $(Phe\text{-}Pyr)_2$ units have desorbed. Coherently, the latter domains get more and more extended with increasing T, i.e., when the coverage of organic fragments reduces. This is indicative of a strong surface rearrangement upon interaction with CyPd. To address the surface reconstruction, I compare my system with previous literature. It is well known that open (110) faces of fcc crystals are prone to surface reconstruction and roughening [79]. Such reorganization is certainly favored by the strong mobility of Ag adatoms, provided by step edges [80], and by the presence of halogen atoms, which are known to form superstructures on several metal surfaces [27], [31]. However, the present situation appears to be more complex.

On one hand, the theoretical model suggests that each Phe-Pyr fragment is anchored to two Ag adatoms, and this could be a reasonable driving mechanism for displacement of Ag adatoms already at RT. In fact, some atom reorganization is evident already at RT, but the presence of densely packed layers (structures A and B) does not allow determining if the surface is already reconstructed or if adatoms simply surround the sticks. On the other hand, the reconstructed phases are observed above RT, when the coverage of Phe-Pyr fragments decreases significantly but halogen atoms are still present on the surface. For this reason, I conclude that the latter have a role in the reconstruction. To better understand the role of each halogen species (Cl and Br), I investigated a simpler molecule i.e. CyPd_2, which has the same structure of CyPd except for not being brominated. These experiments are summarized in Section III. I anticipate that the nonbrominated CyPd_2 molecule formed different organic structures than CyPd, but it caused the same c(2x2) and p(2x1) rearrangements upon annealing the sample.

To summarize this chapter, I described the first investigation of the self-assembly of Pd-cyclometallated compounds on Ag(110) surface at RT. I discussed the structures formed at low and high molecular coverages. At both coverages, dissociation of the molecular precursor occurs upon adsorption on Ag, and well-ordered molecular phases are formed due to the distinct intermolecular and molecule–substrate interactions; at sub-ML coverage, self-assemblies are formed from one molecular fragments coordinated with Ag-adatom taken from the substrate, while at high coverages, when the surface is initially fully covered with molecules, phase is constructed from cross-coupled CyPd fragments coordinated with Ag. Those phases are followed by p(2x1) and c(2x2) reconstruction after annealing the sample.

4. RESULTS: C_YP_D_2/A_G(110)

After the successful results obtained for the CyPd/Ag(110) system, I went on investigating the self-assembly and thermal evolution of similar but simpler molecular precursor i.e. CyPd_2 on Ag(110). The goal of this experiment was to tailor the formation of the self-assemblies. As explained in the introduction, the nonbrominated molecule has one dangling bond less than CyPd when dissociating on the surface and is thus expected to interact differently with the substrate and with other molecules/fragments. Furthermore, it contains one halogen atom less than CyPd, therefore it is used to study the role of halogens in surface reconstruction.
CyPd_2 was deposited following the same protocol previously established. The molecules were deposited at T_{ev}=100 °C on the Ag(110) surface at RT by using the same Ta evaporator used for CyPd. After 30 minutes deposition, a full ML film was formed, as deduced from inspection of several STM images taken in different points of the crystal. No traces of multilayer were observed under the investigated conditions. The surface was eventually annealed for 5 min to temperatures between 100 °C, and 500 °C. The observed self-assemblies are different from the ones produced by CyPd. This is expected since molecules with different functional groups arrange in different geometries. I highlight that along with the molecular features, areas of c(2x2) and a p(2x1) reconstructed Ag(110) surface exist. The interpretation of the data is based on the observed morphology by STM, on complementary XPS data and on comparison with the previously investigated CyPd/Ag(110) system. These results confirm that CyPd_2 also interacts strongly, dissociates at the substrate and that Cl atoms are involved in the surface reconstruction.

4.1. RT deposition and thermal evolution

4.1.1. STM analysis

The overview STM image of Figure 43 depicts the Ag surface after 30 min deposition of CyPd_2 at RT. In this preparation, the Ag(110) surface was, on average, rougher than in the previous set of experiments, since a new crystal was used. Probably also for this reason, quite disordered structures were observed. The disordered arrangement observed in the overview (labelled as "B" in the following) is the majority structure at RT, while less commonly an ordered self-assembly is also observed (labelled A, Figure 44).

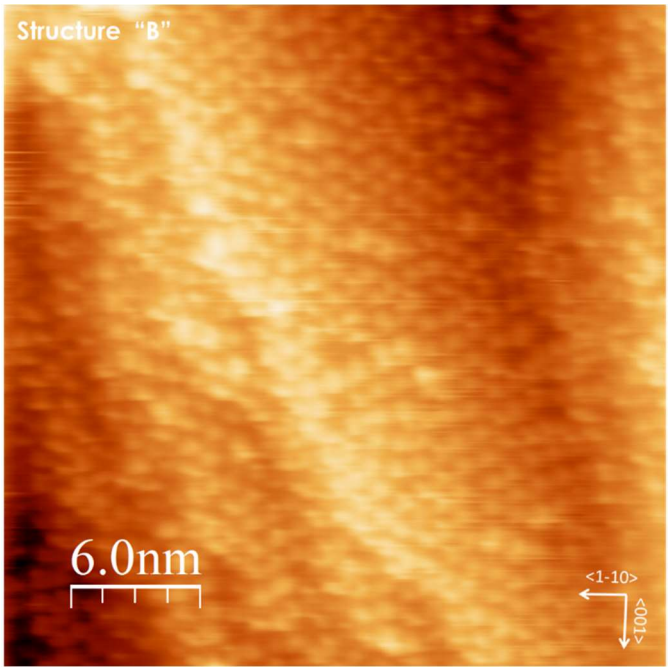

Figure 43 Overview STM image of CyPd_2 on Ag(110) after RT deposition for 30 min(Image size 30x30nm^2, V=1.2 V, i=0.19 nA). The surface was, on average rough and disordered arrangements were observed.

Figure 44 shows structures A and B into more details. Structure A (panel a) consists of rows of molecules with alternating brightness, and is defined by the black rectangle with dimensions a=(1.12±0.03); b=(2.03±0.06) α=(90±3)°, determined from the average periodicities (black and yellow traces) and reported in panel b). Thus, I estimate one molecule/unit cell. Since each unit cell contains a bright and a fainter lobe, I hypothesize that each lobe can correspond to a fragment of the molecule, similarly to what I have previously observed for CyPd. In Structure B the molecules are more distorted and locally arranged in a quasi-hexagonal pattern. This arrangement is short range and will not be discussed into details.

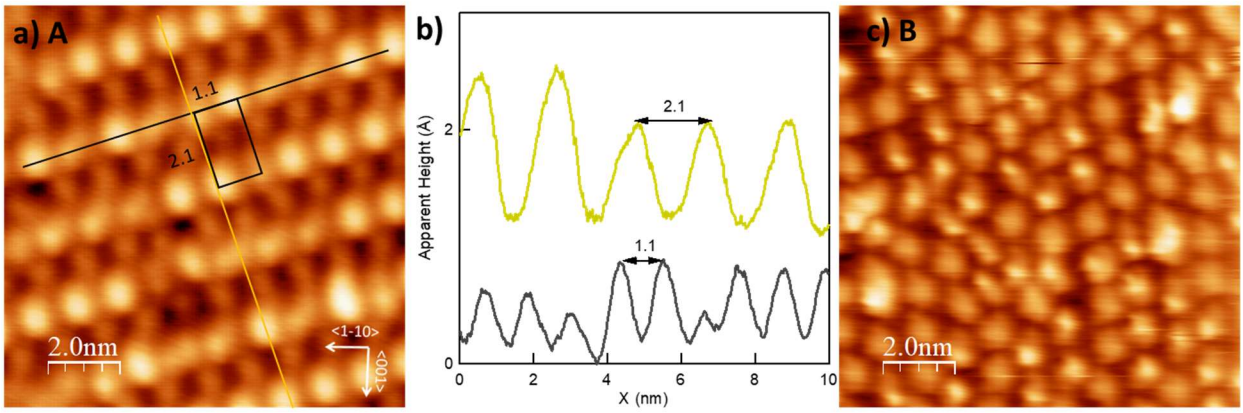

Figure 44 STM images obtained after RT deposition of CyPd_2 on Ag(110) (Image size 10x10nm^2, *V=0.1V, i=0.19 nA).* Panel a) shows Structure A with the unit cell dimensions and geometry determined from the black and yellow traces, which are reported in Panel b). Panel c) shows structure B, which presents local disordered arrangements.

After annealing to 100 °C, partial desorption occurs and the remaining fragments have enough thermal energy to rearrange and form well-ordered long range self-assemblies, as shown in the STM image of Figure 45. Firstly, I mention that the molecules arrange into chain-like structure along the <001> Ag direction. Additionally, patches with both p(2x1) and c(2x2) reconstructions are observed. Those details are emphasized in the right-side images. The molecules/fragments appear as bright features with some internal structure and each of them is surrounded by 10 dots. In most cases the bright features have a nearly square shape with side of ~0.7 nm (blue traces in the line scans of Figure **45**), while some of them appear as lozenges with ~0.8 nm side and major axis ~1.0 nm (green traces). The defined unit cell is quasi-rectangular, with dimensions a=(1.74+0.10) nm, b=(1.19+0.06) nm and α=87+3°, and it contains one bright feature and 10 dots. . The lozenges interrupt the sequence of square-shaped features in the chains. I hypothesize that their presence is due to stress relaxation between the periodicity of the self-assembly and the corrugation of the substrate. From comparison with my previous work and considering the dimensions of the lobe and lozenge features from the apparent height profile, I can tentatively assign them to the molecular fragments. The multiple dots surrounding them could be split off halogen atoms from CyPd_2 or Ag atoms from the substrate.

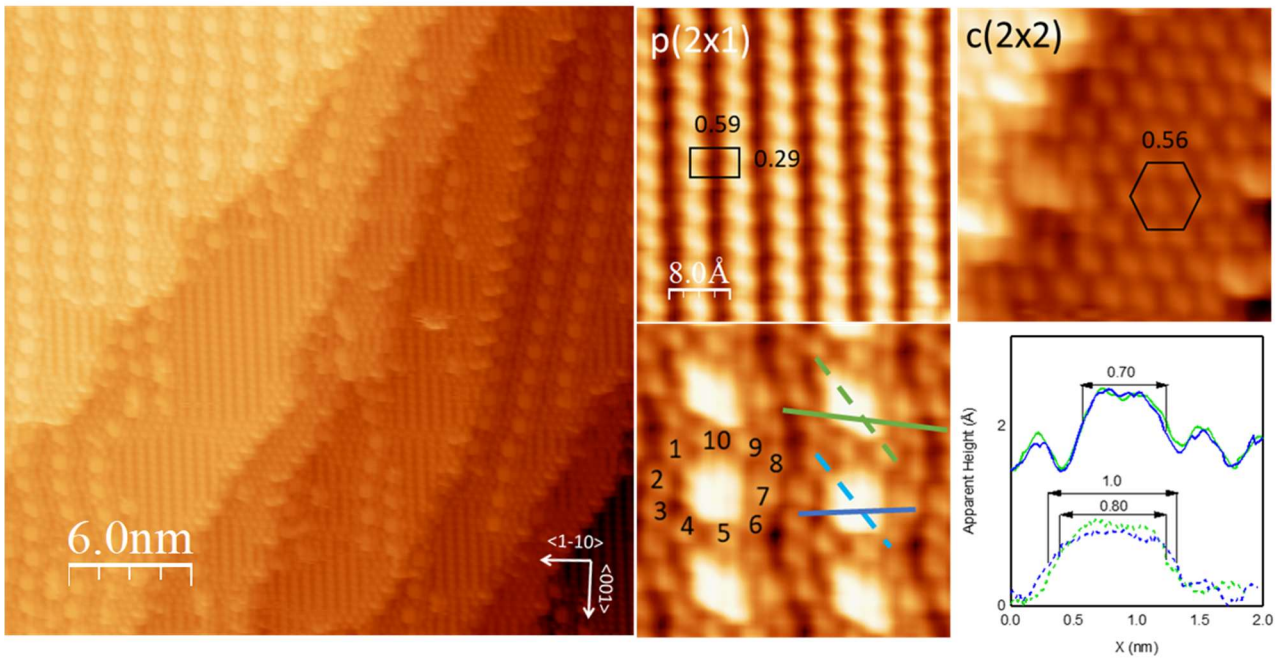

Figure 45 *Overview STM image of CyPd_2 on Ag(110) taken after annealing the sample to 100 °C (Image size 30x30nm^2. V=0.1V, i=0.19 nA). The Ag terraces are reconstructed or covered with molecules arranged in chain-like structure. The* 4x4nm^2 Insets cut from the overview STM, show the details of the different structures. In the bottom right panel, the apparent height profile reports the line scans cut along the red and green traces, corresponding to some of molecular features.

Comparison of the STM images in Figure 46 indicates that the CyPd_2 molecules show bias dependence. As already observed for CyPd, imaging the surface at low bias voltage (0.1V) allows to resolve the details of the internal structure of the bright lobes and to observe all the

interstitial dots. At higher bias voltage (V=2.3V), the features become less resolved and the additional spots disappear. This is an indication of a change in the local density of states. Such a change is less dramatic when imaging at -V.

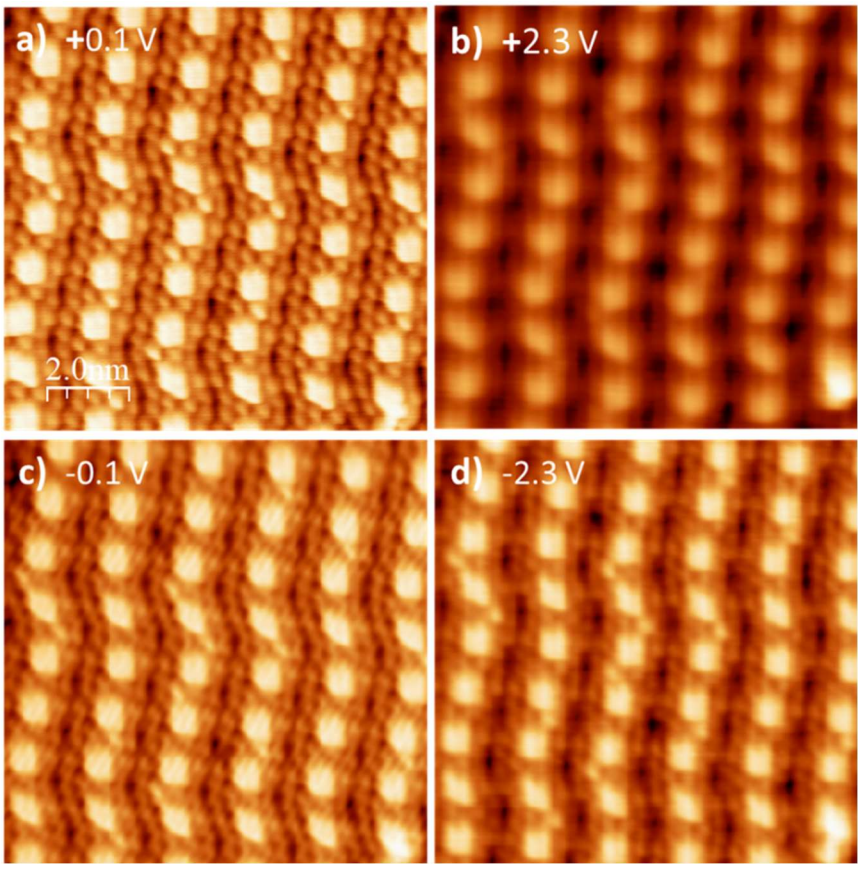

Figure 46 The self-assembled layers of CyPd_2/Ag(110) recorded after annealing at 100 °C (Image size 10x10nm^2, i=0.19 nA). The same area is recorded at V=±0.1 V (panels a,c), V=±2.3 V (panels b,d).

4.1.2. XPS

Figure 47 shows the XPS spectra of the N 1s, C 1s and Cl 2p regions for saturation coverage of CyPd_2 at RT (bottom traces) and their evolution upon annealing to 300 °C (top traces). Contrary to XPS experiments on CyPd, these data were recorded with our laboratory setup, which uses a non-monochromatized X-ray source and have therefore a lower resolution in binding energy. I also mention that I could not perform a detailed analysis of the spectra by fitting all the peaks components, as in Chapter 3.2.2, since these data were recorded in the very last period of my PhD. However, also thanks to the previous knowledge on similar systems [12], [36], I can identify the main features of the spectra.

The C 1s spectrum at RT shows a main peak at BE=284.9 eV. This component is assigned to the unresolved contributions of sp^2 C atoms (C–C component) and C-H bonds, [12], [64]. Using a non-monochromatized Al$_{k\alpha}$ photon, it is hard to effectively detect the N 1s signal due to its small

cross section and small relative abundance with respect to C. Therefore, to plot the spectra on the same scale, I multiplied them by a factor of 5. They show a single large peak centered at BE=399.1 eV, corresponding to C-N bonds [67]. The intensity ratio between N and C, at RT matches well the one expected for the stoichiometric ratio of the CyPd_2 molecule (1:11). The doublet in the Cl 2p region with BE (Cl $2p_{3/2}$)=197.6 eV, suitable for Cl atoms bound either to a metal [48].

After annealing, I observe changes in the C 1s and N 1s regions: the main peaks at 284.9 eV (C 1s) and 399.2 eV (N 1s) downshift by 0.2 eV and their intensity reduces to approximately 50% of the original value when annealing from RT to 200 °C, indicating partial desorption of the organic part of the CyPd molecule. Then the peak areas remain almost stable up to 300 C. Similarly, to CyPd, I associate the residual C 1s and N 1s intensity to a degradation of the remaining fragments; most probably the phenyl and/or pyridine rings break, and smaller fragments bind to the Ag surface. On the contrary, the Cl atoms are much more stable on the surface, and the Cl intensity drops only at 250 °C. The absence of any signal in the Pd region (not shown) indicates that the Pd atoms are effectively screened. This behavior is coherent with what was observed for CyPd and can be rationalized considering that the molecule dissociates due to the interaction with the metal surface. Based on the XPS information and from comparison between CyPd_2 and CyPd, I assume that the CyPd_2 molecule also dissociates after RT deposition, while Cl atoms remain chemically bound to Ag. Consequently, the lobe-like structures observed in STM should correspond to the molecular fragments. The FWHM of the lobe like features that is 0.8 nm, is compatible with the one expected for a phe-pyr units.

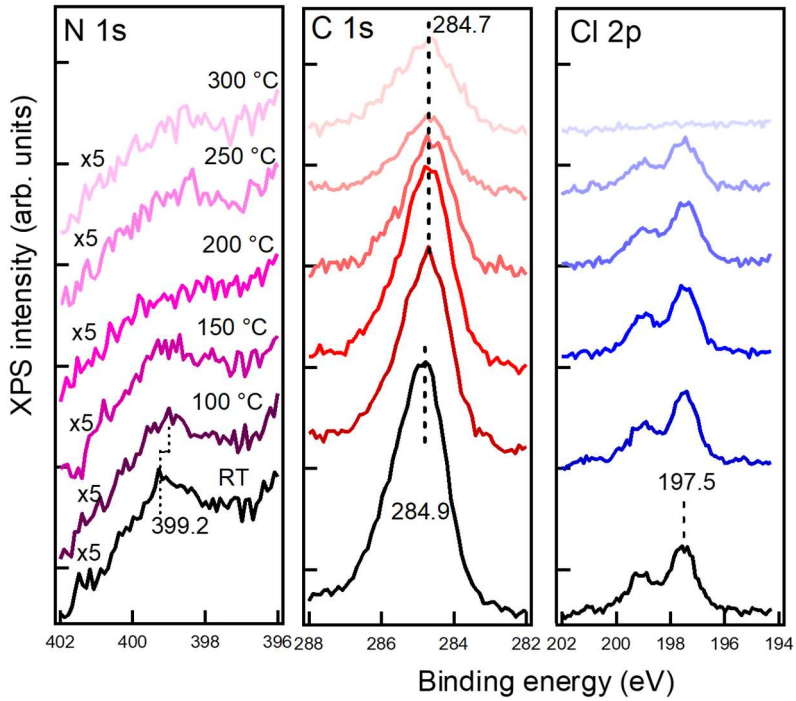

Figure 47 *XPS spectra of N 1s (purple), C 1s (red) and Cl 2p (blue) saturation coverage of CyPd_2/Ag(110) obtained after 80 minutes of deposition at RT and following step-annealing up to 300 °C. Traces are normalized on the background of the corresponding spectrum recorded for clean Ag(110) (not shown) and upshifted for sake of clarity.*

5. CADMIUM CALCOGENICE QUANTUM DOTS ON AU(111)/MICA

5.1. Introduction

In this section I will briefly discuss the work that I did during my three-month internship with the NanoFemtoLab at Institut National de la Recherche Scientifique (INRS), located in Varennes (Canada). My project dealt with cadmium chalcogenide (CdX, X=Se, S) Quantum Dots (QDs), which are important due to their applications in electronic and optoelectronic devices [81]. The aim of my research was to deposit different type of QDs (Colloidal CdSe and CdS) on Au(111) and to investigate their morphology and electronic structure by means of STM and STS, respectively.

The experimental set-ups

The experiments during my internship were carried out either with an ambient STM (Naio) or with a VT UHV STM (Omicron). Figure 48a shows the ambient STM, which is a simple set-up consisting of a scan head, controller and shielding with a magnifying glass for an easy initial approach. It rests on a heavy stone table which allows for reduced vibrations. Panel b) shows The Omicron UHV STM, which consists of a preparation chamber and scanning chamber hosting the STM stage. Like the other UHV system which I used during my PhD at University of Genova, described previously in the experimental section, this chamber is equipped with other commonly used tools: Knudsen cell evaporator for dosing of molecules, fast entry lock system, manipulator, carousel for tips and sample storage, wobble stick for tip and sample handling, leak valves for gasses dosing, quadrupole mass spectrometer. I remark that not all the tools are label on the picture.

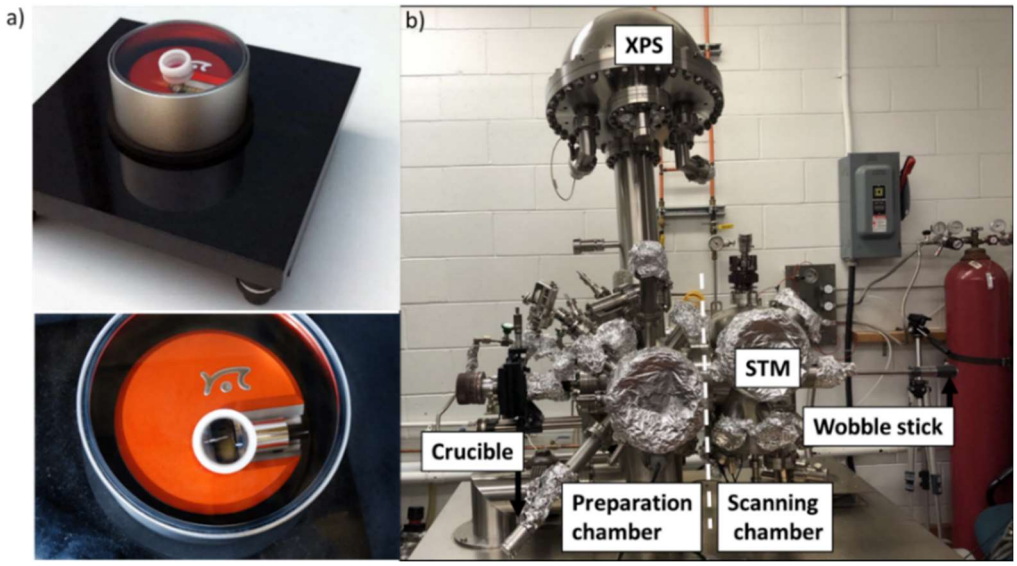

Figure 48 a) NaiO STM, picture taken by www.nanosurf.com. b) Omicron UHV chamber hosting the STM and the other common UHV facilities.

STM measurements

The measurements were recorded either with Pt-Ir tips (ambient STM) or with tungsten (W) tips (UHV). During those experiments, the bias was applied to the tip. The STS measurements were performed by firstly measuring I-V spectra over a certain area. Then, the differential conductance dI/dV was obtained by smoothing and differentiating the experimental I-V curves (NaiO STM) or by using a lock in amplifier (Omicron UHV). For each spectrum, a few scans were recorded over the same area and were averaged (if not indicated otherwise) improving the signal to noise ratio.

The tunneling currents and bias voltages I used were between 300 pA - 1 nA and -0.1 V and -1.2 V, respectively. STM analysis was performed using WSxM software [82] while the STS measurements were analyzed using IGOR Pro software (version 7 by WaveMetrics Inc.)

5.2.Synthesis

Quantum dots can be prepared by *ex-situ* or *in-situ* methods. If prepared *ex-situ*, a wet chemistry approach is used to pre-synthesize QDs in the form of colloids. Colloidal QDs possess uniform size distribution and therefore they have well-defined optical and electronic properties. This makes them very attractive for photoluminescent devices [83].
On the other hand, QDs can be synthesized *in-situ* via successive ionic layer adsorption and reaction (SILAR). This method is easy, cheap and allows for direct growth of QDs on a substrate. As a result, the charge transfer interactions between the QDs and a metal substrate, which depend on the QD-surface separation distance, can be studied [84].

During my internship I worked with colloidal QDs pre-synthetized by Dr. Selopal and his group at INRS. The colloids were prepared by the hot injection method, following the procedure described in [85]. The surface of the QDs was passivated by the organic ligand Oleylamine, whose structure is shown in Figure 49. Then, I attempted to anchored them to the Au(111) substrate via a 1,3-Propanedithiol (PDT) linker solution by drop casting. The 30 mM linker solution was prepared following the method in ref. [86].

In short, the deposition of CdSe colloids on Au was as follows: the Au (111) substrate was first cleaned by 2 cycles of deionized (DI) water followed by drying it under N_2 flux and flame annealing for a few seconds. Then, 10 µl of 30 mM PDT linker solution was drop-casted on the substrate followed by a 10 µl drop of the CdSe colloids.

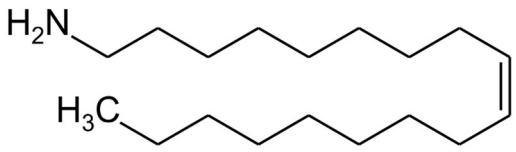

Figure 49 Chemical structure of Oleylamine ($C_{18}H_{35}NH_2$).

The colloids were characterized by transmission electron microscopy (TEM) and optical spectroscopy to determine their shape, average size, and distribution (not shown). The results suggest that the QDs have an average size of 3.0 ± 0.3 nm and nearly spherical shape.

In parallel, I attempted to produce QDs directly on Au(111) by SILAR. The process is explained in the section below.

5.2.1. The SILAR method

The general procedure for SILAR is shown in Figure 50. The method requires repetitive immersion of the substrate in cationic and anionic solutions. After each cycle the sample is dried under N_2 flux. When the substrate is immersed in the cationic solution (beaker 1), the cations adsorb onto the substrate. The unadsorbed cations are then rinsed off by immersing the substrate in a wash off solution (beaker 2). Next, the substrate is immersed into the anionic solution (beaker 3), so that the anions react with the already adsorbed cations. Again, the unreacted ions are removed with the corresponding wash off solution-(beaker 4). Therefore, one SILAR cycle consists of four steps. After a certain amount of immersion cycles, one can obtain NPs with different sizes.

In my experiments, the cationic precursor was cadmium acetate dihydrate $Cd(CH_3COO)_2{\cdot}2H_2O$ and it was weighted (0.26g) and added to 20 mL methanol for a concentration of 50 mM. Similarly, 50 mM ionic precursor solution was prepared by dissolving 0.24 g of sodium sulfide nonahydrate $Na_2S{\cdot}\ 9H_2O$ in 20 mL (50/50 V/V) mixture of Di water/methanol. The cationic and anionic solutions were always kept at 1:1 molar ratio. The wash off solutions were methanol (Cd^{2+}) and a (50/50 V/V) mixture of DI water and methanol (S^{2-}). The immersion time and the wash off time lasted equally.

To optimize the deposition parameters, I prepared different concentrations (50, 33, 25, 10 and 5 mM CdS solutions), I varied the number of SILAR cycles (1,2,3,5 and 8 cycles) and the time of immersion in CdS solution (10 s vs 60 s).

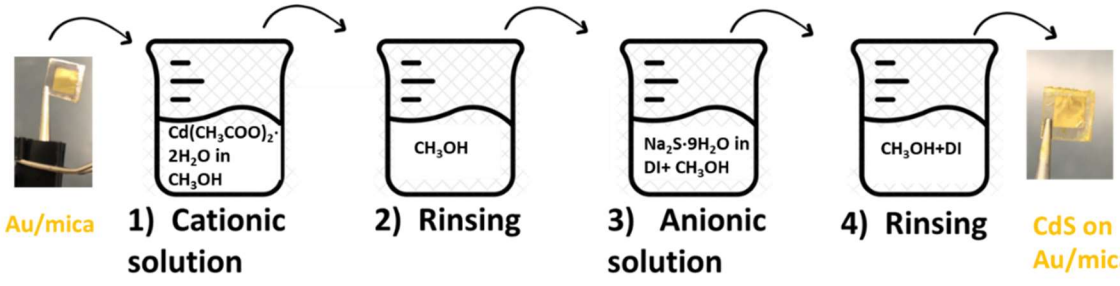

Figure 50 The SILAR method. The ionic precursor solutions used: methanolic solution of $Cd(CH_3COO)_2{\cdot}2H_2O$ and solution of $Na_2S{\cdot}9H_2O$ in methanol/water (50/50 V/V) for Cd^{2+} and S^{2-}, respectively. Wash solutions are CH_3OH (Cd^{2+}) and (50/50 V/V) DI water+ CH_3OH (S^{2-}). After each cycle the sample is dried under N_2 flux. The number of SILAR cycles was varied between 1,3,5, and 8 cycles.

5.3. Preliminary results

In section 5.3.1., I report on the effect of using dithiol molecules as linkers for anchoring of CdSe QDs onto Au(111). Colloidal CdSe Nano Particles (NPs) have been previously successfully linked to Au(111)via dithiols in UHV [87]–[90]. Here, I attempted to form them in ambient conditions and study them in more practical circumstances, by employing ambient STM and STS. To my knowledge, until now, similar work has been done by [91] who reported on ambient STM and STS measurements of similar TOPO/ODA-capped CdSe NCs, spun on Si wafer.

In section 5.3.2., I report on the CdS QDs grown on Au(111). I discuss how some factors like the number of SILAR cycles, concentration, and the immersion time affect the morphology of the formed nanoparticles (NPs). SILAR has been widely employed for fabricating CdX QDs/films, since it is easy and cost effective method compare to other deposition routes [92]–[94]. In most of the studies, the deposition parameters are optimized for more than 10 or even 100 SILAR cycles. Additionally, the most investigated surfaces are usually transparent substrates (glass, TiO_2) [94], [95]. On the contrary, I investigate the effect of few SILAR cycles on the morphology of CdS QDs on Au(111) substrate. The Au substrate was chosen due to its smooth surface and conductivity, while the QDs were chosen because of their opto-electronic properties.

5.3.1. Colloidal CdSe on Au: procedure and results

Figure 51 shows three sets of experiments: CdSe QDs linked to the Au surface via PDT molecules (panel a), PDT molecules deposited on Au substrate (b) and CdSe QDs deposited on Au substrate (c). Panel a) shows that the deposition of 30 mM PDT on Au(111) followed by CdSe colloids results in large (100x100 nm^2) and flat terraces with single atom steps containing 4.0 $\pm$ 0.4 nm size dots. The particle diameter of 4 nm is in good agreement with the TEM analysis. On the contrary, The STM image in panel b) shows that depositing only the CdSe colloids leads to formation of rough surface and no QD like features. The same observation is made for the deposition of PDT linker on Au (panel c). The disarrangement could be due to strong interaction of the tip and the thiol molecules.

Based on the STM information, and considering previous literature [96]), I conclude that the thiols are needed for anchoring of the CdSe on Au. This is due to the strong affinity of thiols for Au i.e. because the Au–S covalent bond (≈180 kJ/mol^{-1}) is stronger than hydrogen bonding or van der Waals interaction [96]. Nevertheless, to better understand the nature of the dots i.e., to assign them to CdSe with certainty, additional measurements with complementary technique are required. Unfortunately, the STS measurements proved difficult under ambient conditions and no conclusive data was acquired for this set of measurements.

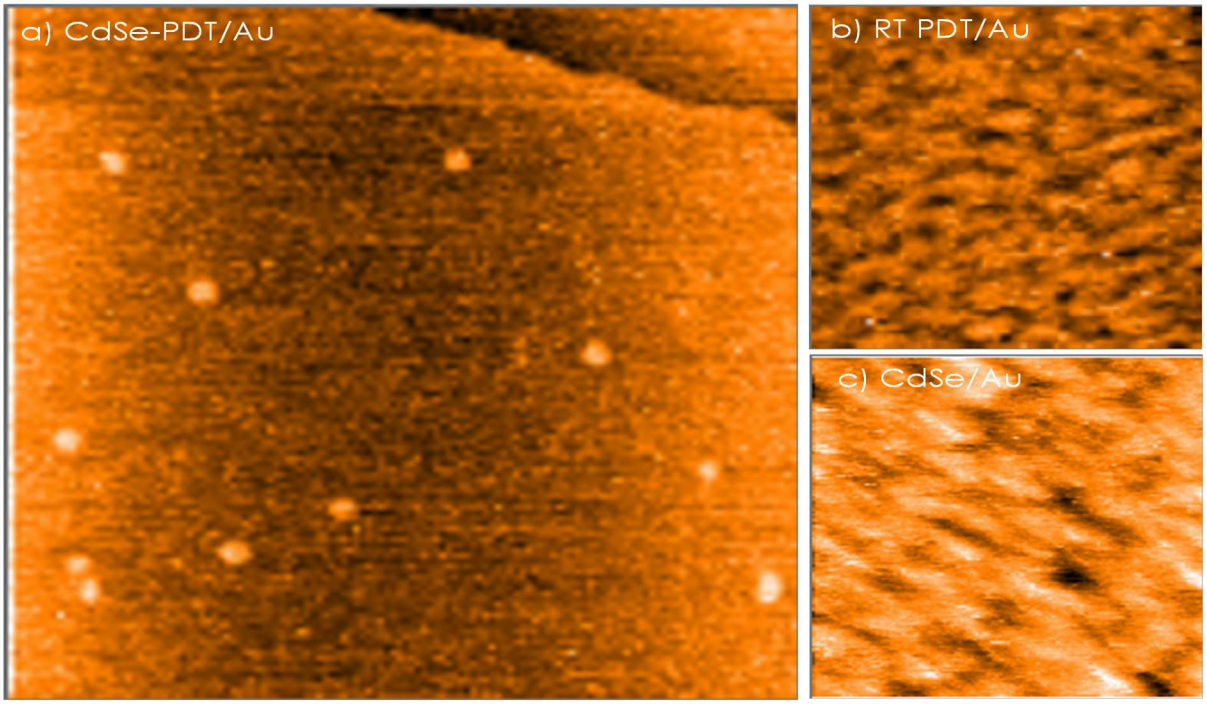

Figure 51a STM image of the pre-synthetized CdSe QDs linked via PDT on Au (100x100 nm^2, i=1nA, V=-300mV. b) 10 µl drop of PDT deposited on Au at RT (48.8x48.8 nm^2, i=1 nA V=-0.6 V). c) CdSe colloids on Au (48.8x48.8 nm^2 , i=1nA V=-0.5 V).

5.3.2. CdS grown on Au by SILAR method.

The aim of this experiment was to form NPs of different sizes and then to study their band gaps in relation to their size. Initially, I started by preparing a 50 mM CdS solution and 2 SILAR cycles of 60s each. The choice of concentration was based on the previous work of Dr. D. Benetti [97] from INRS, who have successfully formed 5.5 nm CdS NPs on HOPG by using 50 mM CdS solution.

The STM image in Figure 52a. shows that after 2 cycles (60s each) in 50 mM CdS solution, the surface is fully covered with continuous and porous network. The size of the pores ranges between 2 and 11 nm, as determined from few overview STM images. Additionally, 5±1.6 nm sized particles are sometimes seen, inset in panel a). The NPs are randomly distributed and most often found near step edges. The apparent height profile in panel b) denotes that the film is one layer thick. These results were surprising, since SILAR is known to form films on Au after tens or hundreds of cycles. Therefore, in the next steps, to optimize the deposition parameters and to attempt to obtain NPs, I reduced the immersion time (Figure **53**) and performed increasing number of SILAR cycles (Figure **54**).

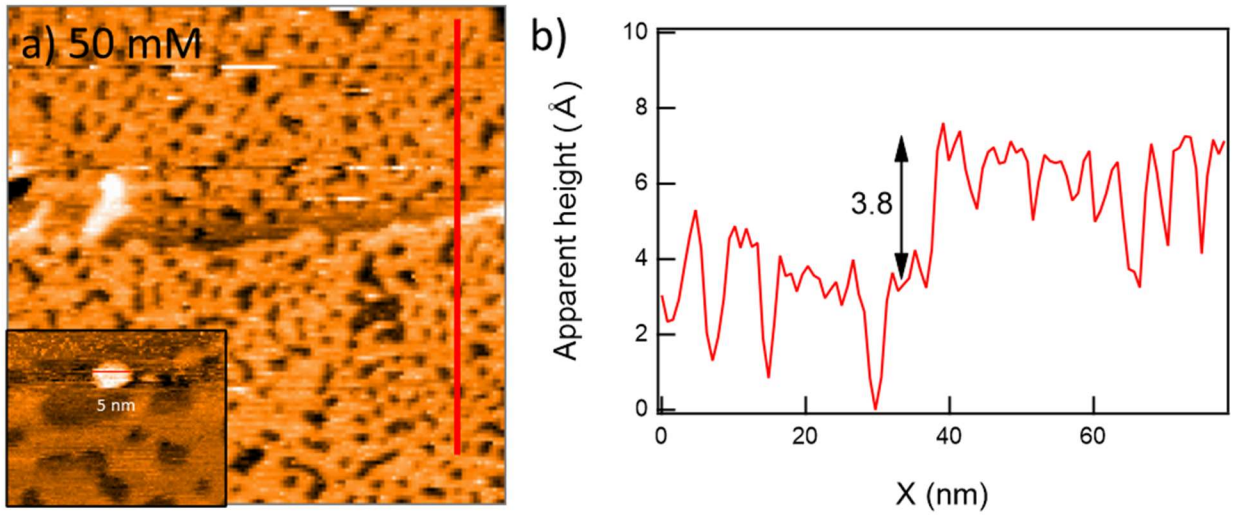

Figure 52 STM image of 50 mM CdS film deposited on Au by 2 SILAR cycles of 60s each. (Size:100x100nm^2, V=-0.6 V, i=300pA). b) Apparent height profile cut along the red trace marked in a).

Figure 53 shows the Au surface after immersion in 50 Mm CdS solution for 60s (panel a) or 10s (b) for 1 cycle. The STM results show that the immersion times affects the crystallinity and shape of the films. In panel a) The surface corresponding to 60s immersion time resulted in homogeneous and dense films with a pore size up to 10 nm. Decreasing the immersion time to 10 s results in irregular and large pore sizes. This can reduce the specific surface area and consequently the QDs loading.

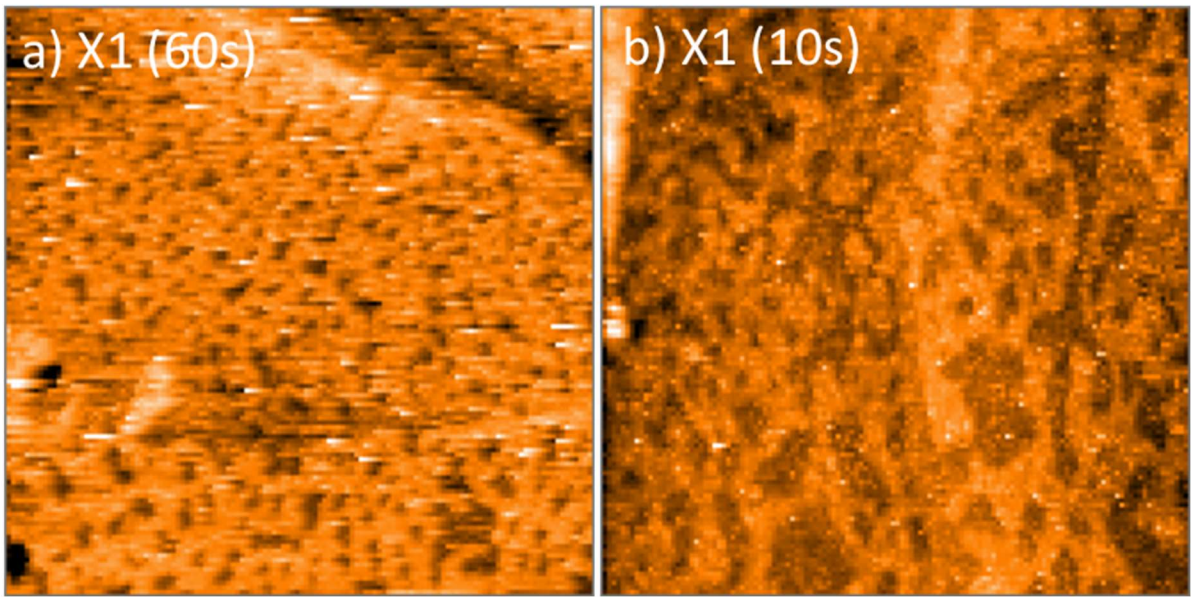

Figure 53 STM images (100x100 nm2) of 1 SILAR cycle. The sample was immersed in 50 mM CdS solution for 60 s (a) and 10 s (b).

Figure 54 shows the Au surface after 1,3,5 and 8 SILAR cycles in 10 mM CdS solution. The STM images indicate that with increasing the number of SILAR cycles particles of different sizes and shape start to form. Panel a) depicts that after one SILAR cycle, the surface is fully covered by a porous film. With increasing the number of SILAR cycles to 3 (panel b), particles with different shapes and sizes start to grow. The particles are randomly orientated and have an average size in the range of 3-10 nm, estimated from STM images inspection. After 5 SILAR cycles, more particles are observed and with slightly larger diameter (panel c), while after 8 cycles almost no particles are found on the surface (panel d). Additionally, I notice that the porosity of the CdS is slightly decreased with increasing the deposition cycle and the x8 SILAR cycles resulted in a film with lowest porosity (panel e). This might suggest that the volume of CdS particles increases because of QDs deposition. Additionally, I notice yellow film forms on the Au(111) substrate. This is in line with the work from [93] who reported that the color and thickness of CdS surface can be changed by varying the SILAR cycles.

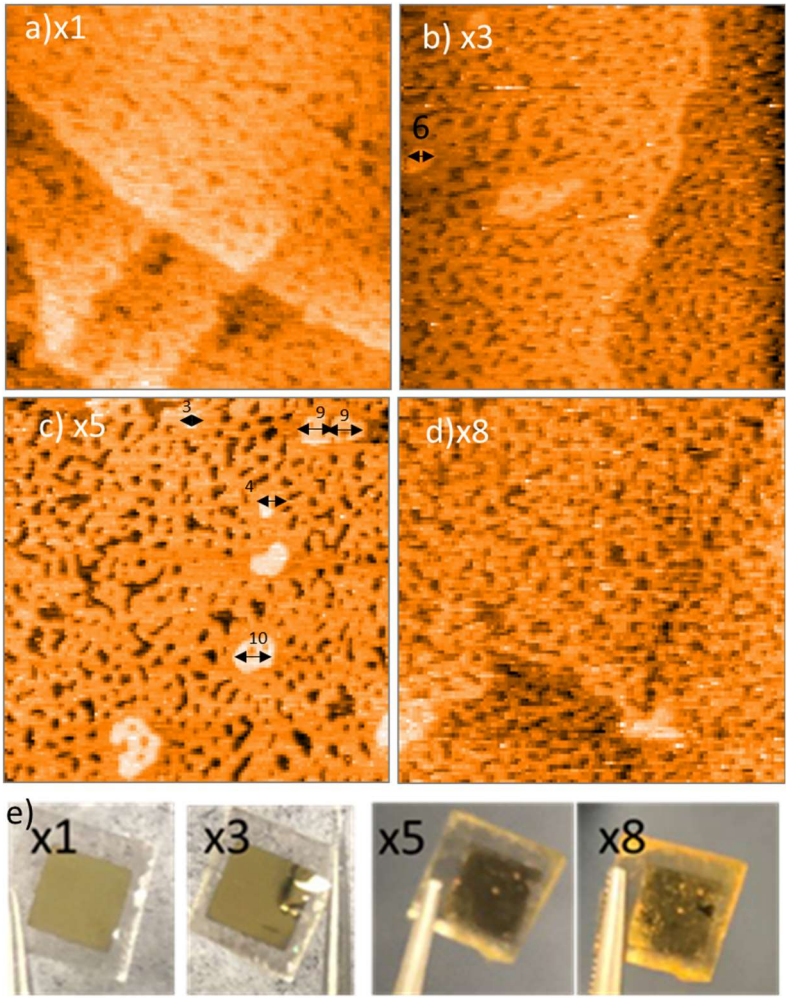

Figure 54 STM images of the Au surface immersed in 10 mM CdS solution for increasing number of SILAR cycles: 1 (panel a), 3 (b), 5 (c) and 8 cycles(d). Each cycle was 60 s. (size 100x100 nm^2, i=500 pA).panel e) shows the samples surface after the increasing cycles.

To obtain information on the electronic structure of the films I recorded I-V curves, Figure 55. The I-V curves taken over the surface of the NP in the inset image indicate the reproducibility between the scans. From the spectra, it is evident that there are some fluctuations in the separation distance between tip/sample for the set of spectra subsequently recorded under same conditions. This can be due to the formation of an oxide layer during the scan. To check the validity of the spectra, I performed STS measurements in UHV, as reported in Figure **56**.

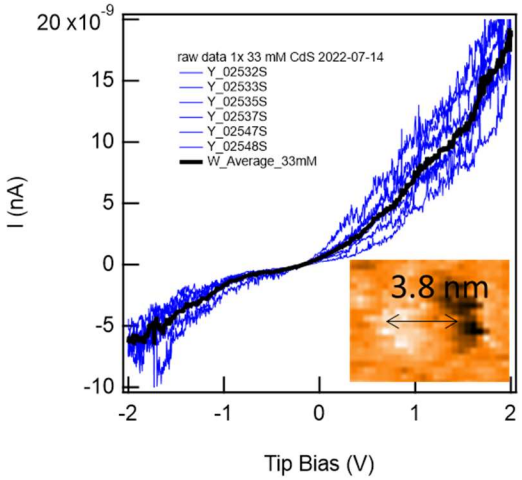

Figure 55 I-V curves (blue traces) taken with the ambient Nalo STM. The tip was placed in the center of the 3.8 nm QD shown in the inset. The set point was 1 nA and V=-1.0 V. The average of the spectra is represented with black trace.The inset image show the morphology of 1 SILAR cycle for 60 s immersion of the Au/mica substrate in 33 mM CdS solution.

5.3.3. UHV STM Results of CdS/Au(111)

The overview STM image shows that after x3 SILAR cycles in 33 mM solution the surface is covered with layers of different contrast. The increased porosity is due to the immersion time (10s instead of 60s) as previously observed under ambient conditions. Panel b denotes that the different layers have different apparent heights, therefore suggesting the formation of a multilayer. I notice that sometimes dot-like features (black circle) with sizes between 1.5 to 5± 0.6 nm sit on top of the layers. The I-V curve taken at the center of one 1.5 nm dot are averaged and shown in panel c) together with the corresponding derivative in panel d). From the STS measurement I see that such dots have a band gap of 3.7 eV. This result is in good agreement with theoretical calculations based on tight-binding approximations [98].

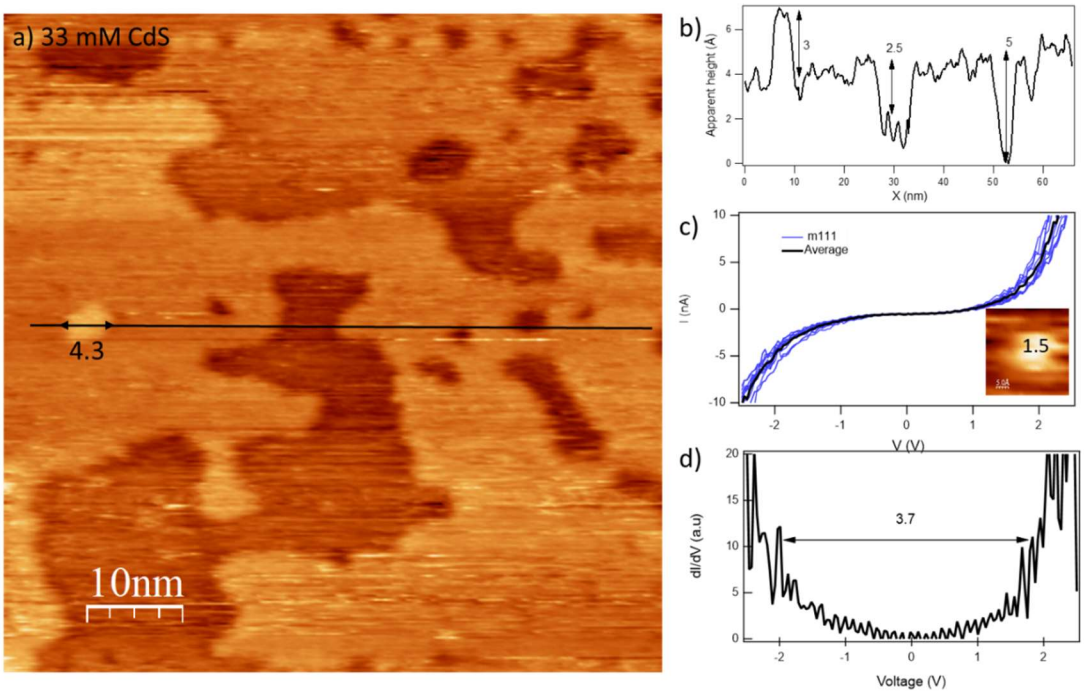

Figure 56a) 33 mM CdS/Au film. Immersion time was 10s for three cycles. STM image size 67x67nm^2, V=+1 V i=2 nA. b) apparent heigh profile corresponding to the black trace in the overview STM image.c) Multiple I-V curves taken over the surface of 1.5±0.9 nm CdS QD to highlight the reproducibility of the measurements. Panel d) dI/dV obtained by differentiating the averaged I-V curve in panel c).

Figure 57. panel a) shows an STM image of the 33 mM CdS on Au, where different layers of the film are seen. The violet and red X mark the location where few spectra are taken and are represented in Panel b). The I-V curves look different for the two different layers. This is because the tunneling current for one or more than one monolayer will differ.

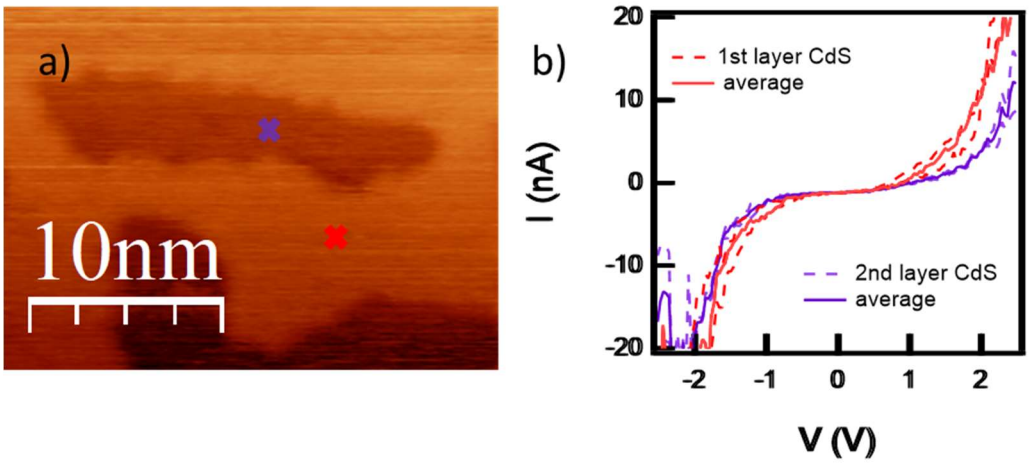

Figure 57a) STM image of 33 mM CdS/Au film. Immersion time was 10 s for 3 cycles. (I=2.27 nA V=1.0 V). b) I-V curves taken on the place marked with X.

6. CONCLUSIONS

In my thesis, I have studied the morphology and chemistry of the self-assemblies formed by CyPd and CyPd_2 on Ag(110). Both systems were studied by first depositing the molecular precursors on the substrate at RT followed by step-annealing up to T_{max} of 500 °C. I prepared a sub-monolayer and a Full ML of CyPd, and a full monolayer film of CyPd_2. At each intermediate temperature, I investigated the morphology of the self-assembled layer and combined the STM information with the complementary results obtained by our collaborators in the MADAM project using the XPS, NEXAFS techniques and DFT methods. On this basis, I can formulate the following conclusions:

Pd-cyclometalated compounds on Ag(110):

1) I reported on the first investigation of the self-assembly of [(5-bromo-2-phenylpyridine)Pd(μ-Cl)]$_2$, $C_{22}H_{14}Br_2Cl_2N_2Pd_2$ (CyPd) deposited on a noble metal surface. The sub-ML CyPd/Ag system was investigated from the morphological and chemical point of view by scanning tunneling microscopy and x-ray photoemission spectroscopy, respectively. The results are validated by ab-initio calculations. The combined experimental and theoretical study aimed at studying the stability of these class of molecules after deposition at RT and stepwise annealing to 150 °C. My results revealed unexpected surface chemistry: An ordered self-assembled layer of paired rows of lozenge-shaped features with interstitial dots in between them forms after deposition of CyPd on Ag. DFT calculations, corroborated by the experimental findings, indicate that the molecule dissociates due to the interaction with the metal substrate: the halogen atoms bind to the surface, the two phe-pyr fragments saturate towards an Ag adatom and the Pd atoms diffuse inside the Ag substrate. Therefore, the formation of a C-based network at the surface occurs upon a drastic modification of the system, in which metal atoms are embedded in regular positions. The details of this study reveal the active role played by the metal substrate in promoting the chemistry of the deposited Pd cyclometallates and could open new perspectives for the application of this class of materials in heterogeneous catalysis.
2) I described the structured formed by a full monolayer of CyPd on Ag(110) in combination with X-ray Photoelectron Spectroscopy and Density Functional Theory calculations. My results have resolved the molecular geometry of one of the self-assembled structures present on Ag (structure "I") and report on the dissociation of CyPd upon adsorption on Ag at RT. The dissociated fragments originating from the same precursor form diphenyl-bipyridine units via cross coupling reaction. Additionally, the strong interaction between CyPd and Ag substrate results in p(2x1) and c(2x2) reconstructions in areas where complete desorption of the organic part has occurred. This behavior suggests an active role of halogen species (Br and Cl) in the reorganization of the surface. To better understand which of the halogens is responsible for the reconstruction I deposited the non-brominated CyPd molecule (CyPd_2). The corresponding results are summarized below.

3) CyPd_2 on Ag(110): The non-brominated CyPd molecule $C_{22}H_{16}Cl_2N_2Pd_2$ (CyPd_2), was deposited at RT on Ag(110) following the same protocol previously established. Then, the surface was step annealed to 500°C. By comparing the results obtained for the two Pd cyclometallated precursors, I observe that they behave similarly. The molecules dissociate upon adsorption on Ag, their organic part desorbs readily at lower temperatures with respect to the halogen atoms. Moreover, the interaction of CyPd_2 with Ag(110) lead to the same surface reconstructions previously discussed, hence confirming the role of Cl atoms in the perturbation of the substrate. Nevertheless, the final products are quite different, as consequence of the different molecular structure: CyPd_2, which has two dangling bonds than CyPd, assembles in a chain like structure, while occupying rectangular unit cell geometry. This self-assembly is at variance with the one observed for CyPd, which appears as a double-row or zig zag structure of stick shaped features, depending on the flux. This result stress out the importance of the initial choice of the precursor for the synthesis of desired nanostructures.

My data suggest that Ag(110) is still too reactive to act as a support for this class of molecules. Therefore, a future development could be to use a less reactive substrate as Au(111) or an oxide layer, on which the molecules have a lower probability to dissociate and, consequently, Pd is less likely to diffuse into the bulk.

CdX/Au(111)

During my internship I attempted to deposit different QDs (synthesized by two different methods) on Au(111) and to study their morphology by STM in UHV or under ambient conditions. Specifically, I worked with colloidal CdSe QDs which were pre-synthesized by the hot injection method by the chemistry group of Dr. Gurpreet Selopal at INRS. I attempted to deposuted them to the Au(111) substrate via a PDT linker solution by drop casting and I conclude that the linker solution is necessary for anchoring the CdSe on the surface of Au(111). This is in line with previous works on similar systems.

On the other hand, I report on the morphology of CdS films formed by the SILAR method. I observe that even one SILAR cycle, a thin film of CdS film on Au(111) can be formed. This is different than what has been previously reported in literature, where thin films of CdS on Au by SILAR were reached after > 100 cycles ([92]). Additionally, the crystallinity of the film can be affected by the immersion time. Shorter (10 s) immersions resulted in irregular and more porous networks with respect to 60 s. Finally, increase in SILAR cycle results in increase in NPs size and shapes. This holds true for up to 5 cycles. Then, the increase up to 8 SILAR cycles leads in decrease in film porosity.

ACKNOWLEDGMENTS

Foremost, I would like to express my gratitude to Dr. Letizia Savio for giving me the opportunity to work on the research project. She has followed me since my master studies, and she is the best mentor I have ever had. What I have achieved to date is because of her and I will truly miss our lab and working for such an amazing leader. Likewise, I would like to thank prof. Gianangelo Bracco for his mentorship, for the contribution to the thesis, patience, and willingness to teach us quantum mechanics. I also appreciate all his help with all the other Ph.D. related things.

I am thankful to prof. Mario Rocca, who not only taught us physics and chemistry, but also, enriched our knowledge in Italian culture. I am grateful that he has never forgotten us, like SERP+ alumni, and he always invited us to operas, museums, excursions around Italy.

I am grateful to prof. Luca Vattuone for the scientific discussions and his contributions to the project that improved my understanding of molecular self-assemblies.

Dr. Marco Smerrieri is our STM expert and the reason why it works. I thank him for his help in solving the LT-STM mysteries. Also, I appreciate all the sweet treats he has shared with us-they always made my day. I thank Dr. Giovanni Carraro, who also took the edge off the frustration of keeping a UHV STM functional. He always helped us, in so many ways. I thank him for the understanding and valuing our opinion.

I thank Simone, Ola, and Dr. Clement for the nice working atmosphere and all the nice times spent together enjoying nice food and drinks. Also, Manuel Corrales, who was always there for me.

I thank the group of prof. C.D. Valentin for the theoretical calculations, and especially Dr. Danielle Perilli for his immediate responses and work ethic. I also acknowledge prof. Antonio Papagni and the chemistry group from University of Milano Bicocca, who synthesized the molecules and contributed to the chemistry. I thank the collaborators from Trieste and Aloisa beamline who contributed to the HR-XPS data.

I thank prof. Federico Rosei for the opportunity to do an internship at INRS, Dr. Tarnjit Johal Kaur for the supervision, the chemistry group of Dr. D. Benetti, Dr. G. Selopal and Dr. Lei Chin for the synthesis of CdSe QDs and their help with the chemistry. I thank Navathej and Dominik, the Ph.D. students from the surface science group, for their help and collaboration during my time in Canada.

I thank the coordinator of my Ph.D. program, prof. Renata Riva for allowing my missions abroad to happen, for her flexibility and understanding.

My special thanks go to Jed, who is my colleague, partner in crime and my best friend. I thank you for tolerating my shenanigans, for being always there for me, for all the advice, exchange of thoughts on our common projects. You are the most brilliant person I have ever met, and I am so lucky to have you in my life. I love you.

I thank my Jonathan, the most important person in my life, for all his love, support, and for all the editing advice and time spent in teaching me more about design. I love you 4012. Likewise, I thank his family for the support and welcoming me to their home.

Finally, I thank my family, my mother, father, and brother who set me off on this road a long time ago. I am grateful for their love and faith in me. Благодарна сум за Вашата љубов и верба, и ништо не ме прави посреќна од тоа Вие да сте горди. Ве сакам,

BIBLIOGRAPHY

[1] H. Chen *et al.*, "On the mechanism of homogeneous Pt-catalysis: A theoretical view," *Coord. Chem. Rev.*, vol. 437, p. 213863, 2021.

[2] P. Sehnal, R. J. K. Taylor, and L. J. S. Fairlamb, "Emergence of palladium(IV) chemistry in synthesis and catalysis," *Chem. Rev.*, vol. 110, no. 2, pp. 824–889, 2010.

[3] A. Biffis, P. Centomo, A. Del Zotto, and M. Zecca, "Pd Metal Catalysts for Cross-Couplings and Related Reactions in the 21st Century: A Critical Review," *Chem. Rev.*, vol. 118, no. 4, pp. 2249–2295, 2018.

[4] M. Mauro, A. Aliprandi, D. Septiadi, N. S. Kehr, and L. De Cola, "When self-assembly meets biology: Luminescent platinum complexes for imaging applications," *Chem. Soc. Rev.*, vol. 43, no. 12, pp. 4144–4166, 2014.

[5] M. Fanelli, M. Formica, V. Fusi, L. Giorgi, M. Micheloni, and P. Paoli, "New trends in platinum and palladium complexes as antineoplastic agents," *Coord. Chem. Rev.*, vol. 310, pp. 41–79, 2016.

[6] F. De Castro, E. De Luca, M. Benedetti, and F. P. Fanizzi, "Platinum compounds as potential antiviral agents," *Coord. Chem. Rev.*, vol. 451, p. 214276, 2022.

[7] V. W. W. Yam, V. K. M. Au, and S. Y. L. Leung, "Light-Emitting Self-Assembled Materials Based on d8 and d10 Transition Metal Complexes," *Chem. Rev.*, vol. 115, no. 15, pp. 7589–7728, 2015.

[8] J. Kalinowski, V. Fattori, M. Cocchi, and J. A. G. Williams, "Light-emitting devices based on organometallic platinum complexes as emitters," *Coord. Chem. Rev.*, vol. 255, no. 21–22, pp. 2401–2425, 2011.

[9] D. C. Powers and T. Ritter, "Palladium(III) in synthesis and catalysis," *Top. Organomet. Chem.*, vol. 503, pp. 129–156, 2011.

[10] R. Mosteiro *et al.*, "Cyclometallated palladium diphosphane compounds derived from the chiral ligand (S)-PhCH(Me)NMe2. Michael addition reactions to the vinylidene double bond," *Eur. J. Inorg. Chem.*, no. 11, pp. 1824–1832, 2011.

[11] R. Chinchilla and C. Nájera, "Chemicals from alkynes with palladium catalysts," *Chem. Rev.*, vol. 114, no. 3, pp. 1783–1826, 2014.

[12] M. Smerieri *et al.*, "Synthesis of graphene nanoribbons with a defined mixed edge-site sequence by surface assisted polymerization of (1,6)-dibromopyrene on Ag(110)," *Nanoscale*, vol. 8, no. 41, pp. 17843–17853, 2016.

[13] C. Sánchez-Sánchez, F. Yubero, A. R. González-Elipe, L. Feria, J. F. Sanz, and R. M. Lambert, "The flexible surface revisited: Adsorbate-induced reconstruction, homocoupling, and sonogashira cross-coupling on the Au(100) surface," *J. Phys. Chem. C*, vol. 118, no. 22, pp. 11677–11684, 2014.

[14] G. Galeotti *et al.*, "The role of halogens in on-surface Ullmann polymerization," *Faraday Discuss.*, vol. 204, pp. 453–469, 2017.

[15] V. K. Jain, "Cyclometalated group-16 compounds of palladium and platinum: Challenges and opportunities," *Coord. Chem. Rev.*, vol. 427, p. 213546, 2021.

[16] M. Albrecht, "Cyclometalation using d-block transition metals: Fundamental aspects and recent trends," *Chem. Rev.*, vol. 110, no. 2, pp. 576–623, 2010.

[17] S. Wilde *et al.*, "Toward Tunable Electroluminescent Devices by Correlating Function and Submolecular Structure in 3D Crystals, 2D-Confined Monolayers, and Dimers," *ACS Appl. Mater. Interfaces*, vol. 10, no. 26, pp. 22460–22473, 2018.

[18] J. Ren *et al.*, "On-Surface Reactive Planarization of Pt(II) Complexes," *Angew.*

Chemie - Int. Ed., vol. 58, no. 43, pp. 15396–15400, 2019.
[19] H. Gersen *et al.*, "Dissociation of iridium(III) phosphorescent emitters upon adsorption on Cu(110) revealed by scanning tunneling microscopy," *Appl. Phys. Lett.*, vol. 89, no. 26, pp. 10–13, 2006.
[20] C. N. R. Rao, K. Gopalakrishnan, and A. Govindaraj, "Synthesis, properties and applications of graphene doped with boron, nitrogen and other elements," *Nano Today*, vol. 9, no. 3, pp. 324–343, 2014.
[21] X. Yang, X. Dou, A. Rouhanipour, L. Zhi, H. J. Räder, and K. Müllen, "Two-dimensional graphene nanoribbons," *J. Am. Chem. Soc.*, vol. 130, no. 13, pp. 4216–4217, 2008.
[22] X. Li, X. Wang, L. Zhang, S. Lee, and H. Dai, "Chemically derived, ultrasmooth graphene nanoribbon semiconductors," *Science (80-.).*, vol. 319, no. 5867, pp. 1229–1232, 2008.
[23] L. Jiao, L. Zhang, X. Wang, G. Diankov, and H. Dai, "Narrow graphene nanoribbons from carbon nanotubes," *Nature*, vol. 458, no. 7240, pp. 877–880, 2009.
[24] M. Y. Han, B. Özyilmaz, Y. Zhang, and P. Kim, "Energy band-gap engineering of graphene nanoribbons," *Phys. Rev. Lett.*, vol. 98, no. 20, pp. 1–4, 2007.
[25] X. Li *et al.*, "Facile synthesis of N-doped carbon nanotubes grafted on N-doped carbon nanosheets co-encapsulating cobalt and molybdenum carbide nanoparticles for efficient methanol oxidation," *Mater. Today Chem.*, vol. 23, 2022.
[26] J. Hu *et al.*, "Ullmann coupling of 2,7-dibromopyrene on Au(1 1 1) assisted by surface adatoms," *Appl. Surf. Sci.*, vol. 513, no. October 2019, p. 145797, 2020.
[27] B. V. Andryushechkin, T. V. Pavlova, and K. N. Eltsov, "Adsorption of halogens on metal surfaces," *Surf. Sci. Rep.*, vol. 73, no. 3, pp. 83–115, 2018.
[28] D. Dettmann *et al.*, "Identification of Topotactic Surface-Confined Ullmann-Polymerization," *Small*, vol. 17, no. 41, pp. 1–10, 2021.
[29] J. G. Serafin, A. C. Liu, and S. R. Seyedmonir, "Surface science and the silver-catalyzed epoxidation of ethylene: An industrial perspective," *J. Mol. Catal. A Chem.*, vol. 131, no. 1–3, pp. 157–168, 1998.
[30] B. V. Andryushechkin, V. V. Cherkez, T. V. Pavlova, G. M. Zhidomirov, and K. N. Eltsov, "Structural transformations of Cu(110) surface induced by adsorption of molecular chlorine," *Surf. Sci.*, vol. 608, pp. 135–145, 2013.
[31] C. Benndorf and B. Kruger, "Adsorption and reaction of bromine with Ag(110)," *Surf. Sci.*, vol. 151, pp. 271–288, 1985.
[32] C. Bronner, J. Björk, and P. Tegeder, "Tracking and removing br during the on-surface synthesis of a graphene nanoribbon," *J. Phys. Chem. C*, vol. 119, no. 1, pp. 486–493, 2015.
[33] M. Abyazisani, J. M. MacLeod, and J. Lipton-Duffin, "Cleaning up after the Party: Removing the Byproducts of On-Surface Ullmann Coupling," *ACS Nano*, vol. 13, no. 8, pp. 9270–9278, 2019.
[34] M. Bowker and K. C. Waugh, "Chlorine adsorption and chloridation of Ag(110)," *Surf. Sci.*, vol. 155, no. 1, pp. 1–14, 1985.
[35] M. Smerieri *et al.*, "Synthesis of corrugated C-based nanostructures by Br-corannulene oligomerization," *Phys. Chem. Chem. Phys.*, vol. 20, no. 41, pp. 26161–26172, 2018.
[36] M. Stojkovska *et al.*, "Well-Ordered Surface Metal Atoms Complexation by Deposition of Pd Cyclometallated Compounds on Ag (110)," *Appl. Surf. Sci.*, vol. 606, 2022.
[37] J. E. Barcelon *et al.*, "Formation of diphenyl-bipyridine units by surface assisted cross

coupling in Pd-cyclometalled complexes," *Appl. Surf. Sci.*, vol. 609, no. August 2022, p. 155307, 2023.
[38] A. Laugier and J. Garai, "Derivation of the ideal gas law," *J. Chem. Educ.*, vol. 84, no. 11, pp. 1832–1833, 2007.
[39] G. Binnig, H. Rohrer, C. Gerber, and E. Weibel, "Tunneling through a controllable vacuum gap," *Appl. Phys. Lett.*, vol. 40, no. 2, pp. 178–180, 1982.
[40] K. Besocke, "An easily operable scanning tunneling microscope," *Surf. Sci.*, vol. 181, no. 1–2, pp. 145–153, 1987.
[41] I. Horcas, R. Fernández, J. M. Gómez-Rodríguez, J. Colchero, J. Gómez-Herrero, and A. M. Baro, "WSXM: A software for scanning probe microscopy and a tool for nanotechnology," *Rev. Sci. Instrum.*, vol. 78, no. 1, 2007.
[42] S. C. White, U. R. Singh, and P. Wahl, "A stiff scanning tunneling microscopy head for measurement at low temperatures and in high magnetic fields," *Rev. Sci. Instrum.*, vol. 82, no. 11, pp. 10–15, 2011.
[43] A. Zangwill, *Physics at Surfaces*. 1988.
[44] K. Diller, R. J. Maurer, M. Müller, and K. Reuter, "Interpretation of x-ray absorption spectroscopy in the presence of surface hybridization," *J. Chem. Phys.*, vol. 146, no. 21, 2017.
[45] Joachim Stöhr, "NEXAFS spectroscopy by Joachim Stöhr (z-lib," *NEXAFS Spectrosc.*, vol. 25, pp. 114–161, 1992.
[46] G. Bracco and B. Holst, "Surface science techniques," *Springer Ser. Surf. Sci.*, vol. 51, no. 1, pp. 277–303, 2013.
[47] M. Katsikini, F. Pinakidou, E. C. Paloura, E. Wendler, W. Wesch, and R. Manzke, "N - K edge NEXAFS study of the defects induced by indium implantation in GaN," *J. Phys. Conf. Ser.*, vol. 190, 2009.
[48] G. M. National Institute of Standards and Technology, "NIST X-ray Photoelectron Spectroscopy Database," 2000. .
[49] G. Bracco, "Comparison of quadrupole mass filters equipped with rods of different convexity: An analysis by finite element methods and trajectory simulations," *Int. J. Mass Spectrom.*, vol. 278, no. 1, pp. 75–88, 2008.
[50] P. Giannozzi *et al.*, "QUANTUM ESPRESSO: A modular and open-source software project for quantum simulations of materials," *J. Phys. Condens. Matter*, vol. 21, no. 39, 2009.
[51] P. Giannozzi *et al.*, "Advanced capabilities for materials modelling with Quantum ESPRESSO. (arXiv:1709.10010v1 [cond-mat.mtrl-sci])," *J. Phys. Condens. Matter*, vol. 29, no. 46, p. 465901, 2017.
[52] P. Giannozzi *et al.*, "Quantum ESPRESSO toward the exascale," *J. Chem. Phys.*, vol. 152, no. 15, 2020.
[53] K. Lee, É. D. Murray, L. Kong, B. I. Lundqvist, and D. C. Langreth, "Higher-accuracy van der Waals density functional," *Phys. Rev. B - Condens. Matter Mater. Phys.*, vol. 82, no. 8, 2010.
[54] I. Hamada and M. Otani, "Comparative van der Waals density-functional study of graphene on metal surfaces," *Phys. Rev. B - Condens. Matter Mater. Phys.*, vol. 82, no. 15, pp. 1–4, 2010.
[55] A. Basagni *et al.*, "On-surface photo-dissociation of C-Br bonds: Towards room temperature Ullmann coupling," *Chem. Commun.*, vol. 51, no. 63, pp. 12593–12596, 2015.
[56] L. Ferrighi *et al.*, "Control of the intermolecular coupling of dibromotetracene on

Cu(110) by the sequential activation of C-Br and C-H bonds," *Chem. - A Eur. J.*, vol. 21, no. 15, pp. 5826–5834, 2015.
[57] J. D. P. Hendrik J. Monkhorst, "Special points for Brillonin-zone integrations*," *Phys. Rev. B*, vol. 13, no. 12, pp. 5188–5192, 1976.
[58] D. R. Tersoff, J. and Hamann, "Theory of the scanning tunneling microscope," *Phys. Rev. B*, vol. 31, no. 2, pp. 805--813, 1985.
[59] D. Nečas and P. Klapetek, "Gwyddion: An open-source software for SPM data analysis," *Cent. Eur. J. Phys.*, vol. 10, no. 1, pp. 181–188, 2012.
[60] X. Peng, Y. Zhu, T. A. Ramirez, B. Zhao, and Y. Shi, "New reactivity of oxaziridine: Pd(II)-catalyzed aromatic C-H ethoxycarbonylation via C-C bond cleavage," *Org. Lett.*, vol. 13, no. 19, pp. 5244–5247, 2011.
[61] E. C. Constable, A. M. W. Cargill Thompson, T. A. Leese, D. G. F. Reese, and D. A. Tocher, "Cyclometallation reactions of 2-phenylpyridine; crystal and molecular structure of (2-{2-pyridyl} phenyl)palladium(II) tetramer and (2-{2-pyridyl} phenyl)mercury(II) tetramer," *Inorganica Chim. Acta*, vol. 182, no. 1, pp. 93–100, 1991.
[62] A. BIGANZOLI, "SINTESI E CARATTERIZZAZIONE DI CICLOMETALLATI DI METALLI DI TRANSIZIONE CON LEGANTI ALOGENATI," UNIVERSITA' DEGLI STUDI DI MILANO BICOCCA.
[63] J. Eichhorn *et al.*, "On-surface ullmann coupling: The influence of kinetic reaction parameters on the morphology and quality of covalent networks," *ACS Nano*, vol. 8, no. 8, pp. 7880–7889, 2014.
[64] I. Píš *et al.*, "Surface-Confined Polymerization of Halogenated Polyacenes: The Case of Dibromotetracene on Ag(110)," *J. Phys. Chem. C*, vol. 120, no. 9, pp. 4909–4918, 2016.
[65] R. Gutzler *et al.*, "Ullmann-type coupling of brominated tetrathienoanthracene on copper and silver," *Nanoscale*, vol. 6, no. 5, pp. 2660–2668, 2014.
[66] Y. Zubavichus *et al.*, "X-ray photoelectron spectroscopy and near-edge X-ray absorption fine structure study of water adsorption on pyridine-terminated thiolate self-assembled monolayers," *Langmuir*, vol. 20, no. 25, pp. 11022–11029, 2004.
[67] F. Orlando, P. Lacovig, M. Dalmiglio, A. Baraldi, R. Larciprete, and S. Lizzit, "Synthesis of nitrogen-doped epitaxial graphene via plasma-assisted method: Role of the graphene-substrate interaction," *Surf. Sci.*, vol. 643, pp. 214–221, 2016.
[68] R. H. Temperton, A. J. Gibson, K. Handrup, and J. N. O'Shea, "Adsorption and charge transfer interactions of bi-isonicotinic acid on Ag(111)," *J. Chem. Phys.*, vol. 147, no. 5, 2017.
[69] R. Costantini *et al.*, "Methylamine terminated molecules on Ni(1 1 1): A path to low temperature synthesis of nitrogen-doped graphene," *FlatChem*, vol. 24, no. October, p. 100205, 2020.
[70] W. Xiaoyong and G. Zijian, "Targeting and delivery of platinum-based anticancer drugs," *Chem. Soc. Rev.*, vol. 42, no. 1, pp. 202–224, 2013.
[71] M. Inagaki, M. Toyoda, Y. Soneda, and T. Morishita, "Nitrogen-doped carbon materials," *Carbon N. Y.*, vol. 132, pp. 104–140, 2018.
[72] M. Di Giovannantonio *et al.*, "Insight into organometallic intermediate and its evolution to covalent bonding in surface-confined ullmann polymerization," *ACS Nano*, vol. 7, no. 9, pp. 8190–8198, 2013.
[73] C. Kolczewski *et al.*, "Detailed study of pyridine at the C 1s and N 1s ionization thresholds: The influence of the vibrational fine structure," *J. Chem. Phys.*, vol. 115,

no. 14, pp. 6426–6437, 2001.
[74] O. Adak *et al.*, "Ultrafast Bidirectional Charge Transport and Electron Decoherence at Molecule/Surface Interfaces: A Comparison of Gold, Graphene, and Graphene Nanoribbon Surfaces," *Nano Lett.*, vol. 15, no. 12, pp. 8316–8321, 2015.
[75] C. M. Doyle *et al.*, "Ni-Cu ion exchange observed for Ni(II)-porphyrins on Cu(111)," *Chem. Commun.*, vol. 50, no. 26, pp. 3447–3449, 2014.
[76] K. Shen *et al.*, "On-surface manipulation of atom substitution between cobalt phthalocyanine and the Cu(111) substrate," *RSC Adv.*, vol. 7, no. 23, pp. 13827–13835, 2017.
[77] F.R. de Boer, R. Boom, W.C.M. Mattens, A.R. Miedema, A.K. Niessen, *Cohesion in Metals*. Amsterdam, 1988.
[78] F. Baletto, C. Mottet, and R. Ferrando, "Growth of Three-Shell Onionlike Bimetallic Nanoparticles," *Phys. Rev. Lett.*, vol. 90, no. 13, p. 4, 2003.
[79] G. Bracco and A. C. Levi, "Roughening Transition: Theories and Experiments," in *Springer Handbook of Surface Science*, M. Rocca, T. S. Rhaman, and L. Vattuone, Eds. Springer series in surface sciences, 2020, pp. 3–44.
[80] T. Zambelli, J. Barth, and J. Wintterlin, "Formation mechanism of the O-induced added-row reconstruction on Ag(110): A low-temperature STM study," *Phys. Rev. B - Condens. Matter Mater. Phys.*, vol. 58, no. 19, pp. 12663–12666, 1998.
[81] G. S. Selopal *et al.*, "Interfacial engineering in colloidal 'giant' quantum dots for high-performance photovoltaics," *Nano Energy*, vol. 55, no. October 2018, pp. 377–388, 2019.
[82] I. Horcas, R. Fernández, J. M. Gómez-Rodríguez, J. Colchero, J. Gómez-Herrero, and A. M. Baro, "WSXM: A software for scanning probe microscopy and a tool for nanotechnology," *Rev. Sci. Instrum.*, vol. 78, no. 1, 2007.
[83] F. P. García de Arquer, D. V. Talapin, V. I. Klimov, Y. Arakawa, M. Bayer, and E. H. Sargent, "Semiconductor quantum dots: Technological progress and future challenges," *Science*, vol. 373, no. 6555, 2021.
[84] D. Wang, H. Zhao, N. Wu, M. A. El Khakani, and D. Ma, "Tuning the charge-transfer property of PbS-quantum Dot/TiO 2-nanobelt nanohybrids via quantum confinement," *J. Phys. Chem. Lett.*, vol. 1, no. 7, pp. 1030–1035, 2010.
[85] B. O. Dabbousi *et al.*, "(CdSe)ZnS core-shell quantum dots: Synthesis and characterization of a size series of highly luminescent nanocrystallites," *J. Phys. Chem. B*, vol. 101, no. 46, pp. 9463–9475, 1997.
[86] Z. Hens, D. V. Tallapin, H. Weller, and D. Vanmaekelbergh, "Breaking and restoring a molecularly bridged metal/quantum dot junction," *Appl. Phys. Lett.*, vol. 81, no. 22, pp. 4245–4247, 2002.
[87] E. P. A. M. Bakkers, Z. Hens, L. P. Kouwenhoven, L. Gurevich, and D. Vanmaekelbergh, "A tunnelling spectroscopy study on the single-particle energy levels and electron-electron interactions in CdSe quantum dots," *Nanotechnology*, vol. 13, no. 3, pp. 258–262, 2002.
[88] U. Banin and O. Millo, "Tunneling and optical spectroscopy of semiconductor nanocrystals," *Annu. Rev. Phys. Chem.*, vol. 54, no. 7, pp. 465–492, 2003.
[89] G. F. Goya *et al.*, "Oxidation of ultrathin iron layers grown on C & l 1 i," vol. 436, no. December, pp. 393–400, 1999.
[90] R. Bernard, G. Comtet, G. Dujardin, V. Huc, and A. J. Mayne, "Imaging and spectroscopy of individual CdSe nanocrystals on atomically resolved surfaces," *Appl. Phys. Lett.*, vol. 87, no. 5, 2005.

[91] B. Kundu, S. Chakrabarti, and A. J. Pal, "Redox levels of dithiols in II-VI quantum dots vis-à-vis photoluminescence quenching: Insight from scanning tunneling spectroscopy," *Chem. Mater.*, vol. 26, no. 19, pp. 5506–5513, 2014.
[92] S. Shen, X. Zhang, B. Perdue, and J. L. Stickney, "Formation of CdS using electrochemical atomic layer deposition (E-ALD) and successive ionic layer adsorption reaction (SILAR)," *Electrochim. Acta*, vol. 271, pp. 19–26, 2018.
[93] D. S. Dhawale, D. P. Dubal, M. R. Phadatare, J. S. Patil, and C. D. Lokhande, "Synthesis and characterizations of CdS nanorods by SILAR method: Effect of film thickness," *J. Mater. Sci.*, vol. 46, no. 14, pp. 5009–5015, 2011.
[94] K. Manikandan *et al.*, "Effect of molar concentration on structural, morphological and optical properties of CdS thin films obtained by SILAR method," *Indian J. Pure Appl. Phys.*, vol. 52, no. 5, pp. 354–359, 2014.
[95] T. ÇAYIR TAŞDEMİRCİ, "Effect of Different Thickness and Solution Concentration on Cus Thin Film Grown By Silar Method," *J. Sci. Perspect.*, vol. 3, no. 3, pp. 207–214, 2019.
[96] S. Kano, T. Tada, and Y. Majima, "Nanoparticle characterization based on STM and STS," *Chem. Soc. Rev.*, vol. 44, no. 4, pp. 970–987, 2015.
[97] D. Benetti, D. Cui, H. Zhao, F. Rosei, and A. Vomiero, "Direct Measurement of Electronic Band Structure in Single Quantum Dots of Metal Chalcogenide Composites," *Small*, vol. 14, no. 51, pp. 1–9, 2018.
[98] P. E. Lippens and M. Lannoo, "Calculation of band gap CdS & ZnS," *Phys. Rev. B*, vol. 39, no. 15, pp. 935–942, 1989.

PUBLICATIONS

First and co-first authored publications:

- Barcelon, J. E.+; Stojkovska M.+, Perilli D.; Carraro G.; Smerieri M.; Vattuone L.; Rocca M.; Bracco G.; Dell'Angela M.; Costantini R.; Cossaro A.; Vaghi L.; Papagni A.; Di Valentin C.; Savio L. Formation of diphenyl-bipyridine units by surface assisted cross coupling in Pd-cyclometalled complexes. Accepted in Appl. Surf. Sci. (October), 2022 https://doi.org/10.1016/j.apsusc.2022.155307
- Stojkovska M.+.; Perilli D.+; Barcelon, J. E.; Smerieri M.; Carraro G.; Dinh Thuy H.; Vattuone L.; Rocca M.; Bracco G.; Dell'Angela M.; Costantini R.; Cossaro A.; Vaghi L.; Papagni A.; Di Valentin C.; Savio L. Well-ordered surface metal atoms complexation by deposition of cyclometallated Pd dimers at Ag (110). Accepted in Appl. Surf. Sci. (September), 2022. http://dx.doi.org/10.2139/ssrn.4158267
- Stojkovska, M.; Davì, R.; Carraro, G.; Smerieri, M. Applied Surface Science Vibrational Fingerprint of the Catalytically-Active FeO2-x Iron Oxide Phase on Pt (1 1 1). 2020, 512 (October). https://doi.org/10.1016/j.apsusc.2020.145774.

Other publications, not presented in the thesis:

- Davì, R.; Carraro, G.; Stojkovska, M.; Smerieri, M.; Savio, L.; Lewandowski, M.; Gallet, J.-J.; Bournel, F.; Rocca, M.; Vattuone, L. Intercalation and reactions of CO under single layer Graphene/Ni(111): the role of vacancies. Accepted in Phys. Chem. Chem. Phys. (November), 2022. DOI: 10.1039/D2CP03441G
- Davì, R.; Carraro, G.; Stojkovska, M.; Smerieri, M.; Savio, L.; Lewandowski, M.; Gallet, J.-J.; Bournel, F.; Rocca, M.; Vattuone, L. Boudouard Reaction under Graphene Cover on Ni(111). Appl. Surf. Sci. 2022, 599 (June), 154065. https://doi.org/10.1016/j.apsusc.2022.154065.
- Davì, R.; Carraro, G.; Stojkovska, M.; Smerieri, M.; Savio, L.; Lewandowski, M.; Gallet, J. J.; Bournel, F.; Rocca, M.; Vattuone, L. Graphene Growth on Ni (1 1 1) by CO Exposure at near Ambient Pressure. Chem. Phys. Lett. 2021, 774 (January), 138596. https://doi.org/10.1016/j.cplett.2021.138596

CV

10/2019-10/2022 doctoral studies in Sciences and Technologies of Chemistry and Materials - University of Genoa, Genoa, Italy
09/2017-09-2019 M.S. in chemistry-University Paris-Sud, Orsay, France & in materials science and engineering-University of Genoa, Genoa, Italy
09/2012-08/2016 B.S. in inorganic engineering and environmental protection - University of St. Cyril and Methodius, Skopje, Macedonia